Calhoun: The NPS Institutional Archive

DSpace Repository

Theses and Dissertations | 1. Thesis and Dissertation Collection, all items

2012-06

Characterization of Synthetic Aperture Radar Image Features of the Ocean as a Function of Wind Speed and High Frequency Radar Products

Vicente, Ricardo Miguel F.P.

Monterey, California. Naval Postgraduate School

http://hdl.handle.net/10945/7424

Downloaded from NPS Archive: Calhoun

http://www.nps.edu/library

Calhoun is the Naval Postgraduate School's public access digital repository for research materials and institutional publications created by the NPS community. Calhoun is named for Professor of Mathematics Guy K. Calhoun, NPS's first appointed -- and published -- scholarly author.

Dudley Knox Library / Naval Postgraduate School
411 Dyer Road / 1 University Circle
Monterey, California USA 93943

NAVAL POSTGRADUATE SCHOOL

MONTEREY, CALIFORNIA

THESIS

CHARACTERIZATION OF SYNTHETIC APERTURE RADAR IMAGE FEATURES OF THE OCEAN AS A FUNCTION OF WIND SPEED AND HIGH FREQUENCY RADAR PRODUCTS

By

Ricardo Vicente

June 2012

Thesis Advisor: Jeffrey Paduan
Second Reader: Benjamin Holt

Approved for public release; distribution is unlimited

THIS PAGE INTENTIONALLY LEFT BLANK

REPORT DOCUMENTATION PAGE			Form Approved OMB No. 0704-0188
Public reporting burden for this collection of information is estimated to average 1 hour per response, including the time for reviewing instruction, searching existing data sources, gathering and maintaining the data needed, and completing and reviewing the collection of information. Send comments regarding this burden estimate or any other aspect of this collection of information, including suggestions for reducing this burden, to Washington headquarters Services, Directorate for Information Operations and Reports, 1215 Jefferson Davis Highway, Suite 1204, Arlington, VA 22202-4302, and to the Office of Management and Budget, Paperwork Reduction Project (0704-0188) Washington DC 20503.			
1. AGENCY USE ONLY *(Leave blank)*	**2. REPORT DATE** June 2012	**3. REPORT TYPE AND DATES COVERED** Master's Thesis	
4. TITLE AND SUBTITLE Characterization of Synthetic Aperture Radar Image Features of the Ocean as a Function of Wind Speed and High Frequency Radar Products		**5. FUNDING NUMBERS**	
6. AUTHOR(S)			
7. PERFORMING ORGANIZATION NAME(S) AND ADDRESS(ES) Naval Postgraduate School Monterey, CA 93943-5000		**8. PERFORMING ORGANIZATION REPORT NUMBER**	
9. SPONSORING /MONITORING AGENCY NAME(S) AND ADDRESS(ES) N/A		**10. SPONSORING/MONITORING AGENCY REPORT NUMBER**	
11. SUPPLEMENTARY NOTES The views expressed in this thesis are those of the author and do not reflect the official policy or position of the Department of Defense or the U.S. Government. IRB Protocol number _____N/A_____.			
12a. DISTRIBUTION / AVAILABILITY STATEMENT Approved for public release; distribution is unlimited		**12b. DISTRIBUTION CODE** A	

13. ABSTRACT

Assessment of coastal ocean conditions is valuable for both military and civilian operations. Remote sensing of those conditions can be even more valuable, particularly in the case of all-weather sensor types. The potential for better understanding of ocean conditions through the combination of remote sensing results was recognized here with the focus on SAR imagery and High Frequency (HF) radar-derived surface currents.

The hypothesis that combining remote sensing products may improve results was tested using SAR imagery and available HF radar surface current maps along central California. Data were obtained from 2007–2010 when the network of HF radar stations was operating relatively continuously. Over the same time period, 780 archived SAR images were identified and, of those, 31 images were chosen for detailed assessment by identifying representative images under weak, moderate, and strong wind conditions.

As expected, wind strength played a dominant role in determining the physical processes visible in the SAR imagery. Moderate wind speed of 2–4 m/s exhibited the most obvious ocean-related processes and the best correlation with features in the HF radar surface current maps. Surprising is the discovery that oceanographic features in the SAR imagery represent recent history of tracer advection over hours to days. As such, individual hourly, surface-current snapshots are not, perhaps, the best product for comparing with those features. Features in the daily-average currents, for example, appear more highly correlated with features in SAR imagery under moderate wind conditions.

14. SUBJECT TERMS SAR, HF Radar, Surface Currents, Ocean features, Remote Sensing			**15. NUMBER OF PAGES** 149
			16. PRICE CODE
17. SECURITY CLASSIFICATION OF REPORT Unclassified	**18. SECURITY CLASSIFICATION OF THIS PAGE** Unclassified	**19. SECURITY CLASSIFICATION OF ABSTRACT** Unclassified	**20. LIMITATION OF ABSTRACT** UU

NSN 7540-01-280-5500 Standard Form 298 (Rev. 2-89)
Prescribed by ANSI Std. 239-18

THIS PAGE INTENTIONALLY LEFT BLANK

Approved for public release; distribution is unlimited

CHARACTERIZATION OF SYNTHETIC APERTURE RADAR IMAGE FEATURES OF THE OCEAN AS A FUNCTION OF WIND SPEED AND HIGH FREQUENCY RADAR PRODUCTS

Ricardo Miguel F.P. Vicente
Lieutenant, Portuguese Navy
B.S., Portuguese Naval Academy, 2000

Submitted in partial fulfillment of the
requirements for the degree of

MASTER OF SCIENCE PHYSICAL OCEANOGRAPHY

from the

NAVAL POSTGRADUATE SCHOOL
June 2012

Author: Ricardo Vicente

Approved by: Jeffrey Paduan
Thesis Advisor

Benjamin Holt
Second Reader

Jeffrey Paduan
Chair, Department of Oceanography

THIS PAGE INTENTIONALLY LEFT BLANK

ABSTRACT

Assessment of coastal ocean conditions is valuable for both military and civilian operations. Remote sensing of those conditions can be even more valuable, particularly in the case of all-weather sensor types. The potential for better understanding of ocean conditions through the combination of remote sensing results was recognized here with the focus on SAR imagery and High Frequency (HF) radar-derived surface currents.

The hypothesis that combining remote sensing products may improve results was tested using SAR imagery and available HF radar surface current maps along central California. Data were obtained from 2007–2010 when the network of HF radar stations was operating relatively continuously. Over the same time period, 780 archived SAR images were identified and, of those, 31 images were chosen for detailed assessment by identifying representative images under weak, moderate, and strong wind conditions.

As expected, wind strength played a dominant role in determining the physical processes visible in the SAR imagery. Moderate wind speed of 2–4 m/s exhibited the most obvious ocean-related processes and the best correlation with features in the HF radar surface current maps. Surprising is the discovery that oceanographic features in the SAR imagery represent recent history of tracer advection over hours to days. As such, individual hourly, surface-current snapshots are not, perhaps, the best product for comparing with those features. Features in the daily-average currents, for example, appear more highly correlated with features in SAR imagery under moderate wind conditions.

THIS PAGE INTENTIONALLY LEFT BLANK

TABLE OF CONTENTS

I. INTRODUCTION....1
- **A. MOTIVATION AND BACKGROUND....1**
- **B. CONTRIBUTIONS....2**
- **C. THESIS ORGANIZATION....3**

II. BACKGROUND....5
- **A. SAR....5**
  - **1. SAR Background and Ocean Applications....5**
  - **2. What is SAR?....6**
  - **3. How Does SAR Work?....7**
  - **4. Bragg-Resonant Backscatter and Surface Roughness....8**
  - **5. ASAR Polarization....11**
  - **6. ASAR Measurement Modes....12**
- **B. HF RADAR....14**
  - **1. HF Background and Ocean Applications....14**
  - **2. What is HF Radar?....14**
  - **3. How Does HF Radar Work?....15**
  - **4. Site Description....17**
- **C. SAR AND HF RADAR CHARACTERISTICS....19**

III. DATA SET AND METHODOLOGY....23
- **A. DATA SETS....23**
- **B. HF RADAR SURFACE CURRENT PROCESSING STEPS....23**
- **C. SAR DATA SET AND IMAGE PROCESSING FLOW....24**
  - **1. Data Access....24**
  - **2. Processing Flow....26**
    - ***a. Precise Orbit Files....28***
    - ***b. Absolute Calibration....29***
    - ***b. Slant Range to Ground Range Correction....30***
    - ***c. Multilook....31***
    - ***d. Speckle Noise Filter....33***
    - ***e. Ellipsoid Correction....33***
    - ***f. Mosaic....34***
- **D. WIND DATA....35**
- **E. OVERLAP HF RADAR PRODUCTS AND SAR-PROCESSED IMAGES....36**
- **F. HORIZONTAL DIVERGENCE TEST....36**

IV. RESULTS....39
- **A. EXAMPLE 1 - WIND INTENSITY VS. BACKSCATTER....40**
- **B. EXAMPLE 2 - WIND FRONT....42**
- **C. EXAMPLE 3 – UPWELLING EVENTS....46**
- **D. EXAMPLE 4 – CHANNEL OUTWARD FLOW AND INTERNAL WAVES....52**

E. EXAMPLE 5 – HF-RADAR SURFACE CURRENTS AND SAR IMAGE ASSESSMENT 55
F. EXAMPLE 6 – DIVERGENCE TEST 60
G. EXAMPLE 7 – SAR FEATURES SEEN IN HF-RADAR SURFACE CURRENT 65
H. EXAMPLE 8 – SLICK OFF POINT SUR 68
I. EXAMPLE 9 – ATMOSPHERIC FEATURES AND A CURIOUS RECTANGULAR FEATURE 71

V. CONCLUSIONS 75
A. DISCUSSION 75
B. FUTURE RESEARCH 77

APPENDIX A 79

APPENDIX B 113

LIST OF REFERENCES 119

INITIAL DISTRIBUTION LIST 123

LIST OF FIGURES

Figure 1. Oceanic region of interest included in the square (After Eoli-sa ESA) 2
Figure 2. ESA's ENVISAT (From ESA). 6
Figure 3. The Electromagnetic Spectrum (After Paduan & Graber, 1997) 6
Figure 4. Concept of synthetic aperture (After Canada Centre for Remote Sensing, n.d.) 8
Figure 5. Illustration containing a) Bragg scattering mechanism; b) Tilt modulation – long wave pattern modifies short-wave local incident angle, and c) hydrodynamic modulation – surface currents affect distribution of short waves along a long wave. ζ is the surface elevation and ψ is the wavenumber spectrum. (After Stewart, 1985, Figure 13.6; Canada Centre for Remote Sensing, n.d) 9
Figure 6. VV Polarization (From ASAR Users Guide, n.d., Figure 1.20) 12
Figure 7. Image Mode (After ASAR users guide, n.d., Figure 1.10) 13
Figure 8. Typical Doppler spectrum collected by an OSCR system, showing prominent Bragg peaks due to waves advancing toward and receding from the receiver. Bragg frequencies, $\pm f_{Bragg}$, correspond to positions of no-currents shown by the vertical dashed lines. Δ_f is the additional Doppler shift related to ocean currents (after Graber et al., 1996; Paduan & Graber, 1997). 16
Figure 9. Site localization of HF antennas (after CeNCOOS http://www.cencoos.org/index.html) 18
Figure 10. Dispersion diagram and wave characteristics. Capillary waves on an order of centimeters or less and surface gravity waves on the order of tens of meters (After Hasselmann, 1982, Figure 1; Chu, n.d., Figure 6.54) 20
Figure 11. Histogram of images in Eoli-sa catalogue for the period and ROI. The vertical axis represents the quantity of images. In the legend, ASAR is from ENVISAT and AMI/SAR from ERS-2. 24
Figure 12. ASAR image mode coverage from period 2007-2010 and ROI. Each vertical red segment represents one image. 25
Figure 13. Example of HF radar data available for 2007. Vertical axis shows different HF radar stations illustrated in Figure 9. 25
Figure 14. Example of wind plots from in situ buoy measurements on the ROI for 2010. The vertical solid black segments indicate available ASAR image and solid red segments indicate surface wind direction and magnitude at the time of ASAR image formation. 26
Figure 15. Work flow for SAR IMS with ESA's software NEST. 27
Figure 16. Work flow for SAR IMP with ESA's software NEST. 28
Figure 17. Apply orbit file operator 29
Figure 18. Calibration operator for IMS products. 30
Figure 19. Slant range to ground range operator. 31
Figure 20. Multilook operator for IMS products. 32
Figure 21. Multilook operator for IMP products. 32

Figure 22. Speckle filter operator 33
Figure 23. Ellipsoid correction – geolocation grid operator 34
Figure 24. Mosaic operator 35
Figure 25. SAR image with HF surface currents (red) and wind vectors (green) on 05 July 2008 at 1820 UTC. The image shows well-organized oceanic pattern in which there's a large fetch with strong winds, as well as wind-shadowing effect on the surface in the north part of Monterey Bay (SAR data provided by ESA). 41
Figure 26. True Color map taken on 05 July 2008 at 2143 UTC showing a well-organized atmospheric pattern agreeable with the ocean surface structure in Figure 25 (after NLR, http://www7240.nrlssc.navy.mil/). 42
Figure 27. SAR image with HF currents (red) and wind vectors (green) on 28 August 2008 at 1823 UTC. A frontal feature offshore of Pigeon Point (36.5N-122.8W to 37.2N-123W) is depicted by a sharp contrast in backscatter in an overall low-wind condition ~2 m/s (SAR data provided by ESA). 44
Figure 28. True Color image on 28 August 2008 at 2107UTC (From NLR, http://www7240.nrlssc.navy.mil/). 45
Figure 29. SST map on 27 August 2008 at 2201 UTC showing patches of warmer water close to shore and temperature fronts with an approximately 2° C gradient (After NLR, http://www7240.nrlssc.navy.mil/)..... 45
Figure 30. Upwelling event illustrated on both a) SST and b) Chlorophyll Concentration MODIS products on 6 September 2008 at 2100 UTC. In a) the colder water (greenish) extends from Half Moon Bay to Monterey Bay Canyon. In b) the image shows higher levels of productivity near the coast, corroborating the upwelling occurrence (After NLR, http://www7240.nrlssc.navy.mil/). 46
Figure 31. Upwelling event seen in SAR image on 7 September 08 at 0555 UTC. The darker patches show evidence of colder and biologically richer water from Half Moon Bay to Point Sur and over Monterey Bay Canyon. HF radar surface-current flow is seaward (SAR data provided by ESA). 47
Figure 32. Upwelling event seen in SAR image on 7 October 2010 at 1823 UTC. The darker patches show upwelled-colder and nutrient-richer water along the west coast from San Francisco to Pigeon Point. Note the presence of surfactants associated with natural oils. The horizontal white line indicates the SST map northern latitude in Figure 33. The white box indicates the daily-average HF-radar surface currents seen in Figure 35 (SAR data provided by ESA). 49
Figure 33. MODIS SST map from 7 October 2010 at 2054 UTC showing patches of colder water near the coast from Half Moon Bay to the Pigeon Point area. The black box indicates the SAR image seen in Figure 32, and the white box indicates the daily-average HF-radar surface currents seen in Figure 35. (After NLR, http://www7240.nrlssc.navy.mil/)..... 50
Figure 34. Three buoy wind plots for the six days preceding the SAR-image formation show upwelling favorable winds. The red segment indicates wind condition at the SAR image time. 51

Figure 35. Daily-averaged HF-radar surface currents for the Half Moon Bay area corresponding to the white box on the SAR image (Figure 32). The tide is naturally removed. (From Cencalcurrents, http://cencalcurrents.org). 52
Figure 36. Observed tide in San Francisco on 1 March 2009. The vertical line corresponds to the SAR image time. (After NOAA, http://tidesandcurrents.noaa.gov/).....53
Figure 37. The SAR image is from 1 March 2009 at 0555 UTC and exhibits two recurring local features. In the San Francisco area, there's an outward flow which is imaged upon completion of the ebb tidal cycle and, farther south,internal waves are seen propagating shoreward. The bathymetry contours are overlapped. The blue box delimits the area of Figure 38 (SAR data provided by ESA).....54
Figure 38. HF radar, 24h surface current trajectories for the San Francisco area, equivalent to the blue box in Figure 36. The blue x represents the starting time on 28-Feb-2009 at 0600 UTC, and the red dot the ending time on 01-Mar-2009 at 0600 UTC (From Cencalcurrents, http://cencalcurrents.org). 55
Figure 39. SAR image of Monterey Bay sensed on 14 August 2010 at 1820 UTC. Both SAR and HF-radar products contribute to the interpretation of coastal ocean dynamics. Several slick patterns are seen in the SAR image, and its interpretation is facilitated by the surface current (SAR data provided by ESA).....56
Figure 40. SAR meandering slick stripes assessed in HF-radar vectors, as well. The red arrows show current vectors, and the green arrows represent wind measurements (SAR data provided by ESA).....57
Figure 41. Detailed image of a rain or pressure cell depicted in Monterey Bay sensed on 14 August 2010 at 1820 UTC. (SAR data provided by ESA). 58
Figure 42. HF-radar, 24h surface current trajectories for the Monterey Bay area. The blue x represents the starting time on 13-Aug-2010 at 1800 UTC, and the red dot the ending time on 14-Augr-2010 at 1800 UTC (From Cencalcurrents, http://cencalcurrents.org). 59
Figure 43. Daily-averaged HF-radar surface currents for the Monterey Bay area, ending time on 14-Aug-2010 at 1800. The tide is naturally removed. (From Cencalcurrents, http://cencalcurrents.org). 60
Figure 44. SAR image sensed on 02 September 2010 at 1823 UTC in which a frontal signature aligned north-south is depicted close to Pigeon Point. The white box corresponds to an enlarged area in Figure 46 (SAR data provided by ESA).....61
Figure 45. Divergence test shows a convergence (bluish dots) front centered at 37N 122.5W, where the flow has a north-south alignment. This agrees with the orientation of the surfactants close to the frontal structure depicted in the SAR image in Figure 44 and in the enlarged area in Figure 46.....62
Figure 46. Detail image of a convergence zone depicted by SAR and by the horizontal divergence test in Figure 45. The flow has a north-south alignment (SAR data provided by ESA).....63

Figure 47. SST map with 1km resolution for 02 September 2010 at 2200 UTC, 4 hours after the SAR image, illustrating the type of coastal temperature gradients surrounding the convergence zone. The area being discussed is masked by cloud cover (After NLR, http://www7240.nrlssc.navy.mil/).....64
Figure 48. SAR image sensed on 25 May 2008 at 0555 UTC where both SAR- and HF-radar products detect a frontal signature offshore of Point Sur (details in Figure 49) and an anti-cyclonic eddy offshore of Monterey (details in Figure 50). The average wind is ~ 3m/s (SAR data provided by ESA).....65
Figure 49. Detail of the SAR image sensed on 25 May 2008 at 0555 UTC where a frontal signature offshore of Point Sur is depicted by both SAR- and HF-radar products (SAR data provided by ESA).....66
Figure 50. Divergence test shows a convergence (bluish dots inside the black circle) feature centered at 36.4N 122.25W, where the corresponding SAR image demonstrates a brighter frontal structure (Figure 49). 67
Figure 51. Detail of the SAR image sensed on 25 May 2008 at 0555 UTC with an anti-cyclonic eddy offshore of Monterey Bay, depicted by both SAR- and hourly-averaged HF-radar products (SAR data provided by ESA). 68
Figure 52. MODIS Chlorophyll Concentration and True Color products from 10 February 2008 at 2155 UTC showing a slick oriented NE-SW (After NLR, http://www7240.nrlssc.navy.mil/). 69
Figure 53. Image captured on 10 February 2008 at 0555 UTC. Close to Point Sur there's evidence of frontal features and a slick oriented NE-SW, which is illustrated in Figures 52 a) and b), as well (SAR data provided by ESA). 70
Figure 54. SAR image sensed on 27 September 2009 at 0555 UTC exemplifying atmospheric gravity waves and roll vortices originated by land features (see detail in Figure 55). The wind is weak and from the southeast. Offshore of Point Sur, there's a large rectangular feature (see detail in Figure 56). (SAR data provided by ESA). 72
Figure 55. Detail of atmospheric gravity waves (1) and roll vortices (2) at the bottom of image captured on 27 September 2009 at 0555 UTC. The wind is weak and from the southeast. Offshore of Point Sur, there's a large rectangular feature (see detail in Figure 56). (SAR data provided by ESA). 73
Figure 56. SAR image sensed on 27 September 2009 at 0555 UTC, showing a rectangular feature (2.3km x 1.8km) 32km offshore of Point Sur and a wake signature (SAR data provided by ESA).....73
Figure 57. MODIS Terra True Color product from 27 September 2009 at 1910 UTC showing atmospheric patterns in the Monterey Bay area. Note the rectangular feature SW of Point (After LANCE-MODIS, http://lance-modis.eosdis.nasa.gov/imagery/subsets/?project=aeronet&subset=Monterey). 74
Figure 58. SAR image from 21 July 2007 at 1820 UTC and HF radar currents (red) and surface winds (green) from the closest hour (SAR data provided by ESA).....79

Figure 59. SAR image from 25 August 2007 at 1820 UTC and HF radar currents (red) and surface winds (green) from the closest hour (SAR data provided by ESA).....80
Figure 60. SAR image from 23 September 2007 at 0555UTC and HF radar currents (red) and surface winds (green) from the closest hour (SAR data provided by ESA).....81
Figure 61. SAR image from 3 November 2007 at 1820 UTC and HF radar currents (red) and surface winds (green) from the closest hour (SAR data provided by ESA).....82
Figure 62. SAR image from 3 November 2007 at 1820 UTC and HF radar currents (red) and surface winds (green) from the closest hour (SAR data provided by ESA).....83
Figure 63. SAR image from 10 February 2008 at 0555 UTC and HF radar currents (red) and surface winds (green) from the closest hour (SAR data provided by ESA).....84
Figure 64. SAR image from 16 February 2008 at 1820 UTC and HF radar currents (red) and surface winds (green) from the closest hour (SAR data provided by ESA).....85
Figure 65. SAR image from 15 May 2008 at 1823 UTC and HF radar currents (red) and surface winds (green) from the closest hour (SAR data provided by ESA).....86
Figure 66. SAR image from 25 May 2008 at 0555 UTC and HF radar currents (red) and surface winds (green) from the closest hour (SAR data provided by ESA).....87
Figure 67. SAR image from 13 June 2008 at 0558 UTC and HF radar currents (red) and surface winds (green) from the closest hour (SAR data provided by ESA).....88
Figure 68. SAR image from 05 July 2008 at 1820 UTC and HF radar currents (red) and surface winds (green) from the closest hour (SAR data provided by ESA).....89
Figure 69. SAR image from 28 August 2008 at 1823 UTC and HF radar currents (red) and surface winds (green) from the closest hour (SAR data provided by ESA).....90
Figure 70. SAR image from 7 September 2008 at 0555 UTC and HF radar currents (red) and surface winds (green) from the closest hour (SAR data provided by ESA).....91
Figure 71. SAR image from 13 September 2008 at 1820UTC and HF radar currents (red) and surface winds (green) from the closest hour (SAR data provided by ESA).....92
Figure 72. SAR image from 18 October 2008 at 1820 UTC and HF radar currents (red) and surface winds (green) from the closest hour (SAR data provided by ESA).....93
Figure 73. SAR image from 1 March 2009 at 0555 UTC and HF radar currents (red) and surface winds (green) from the closest hour (SAR data provided by ESA).....94

Figure 74. SAR image from 7 March 2009 at 1820 UTC and HF radar currents (red) and surface winds (green) from the closest hour (SAR data provided by ESA).....95
Figure 75. SAR image from 26 March 2009 at 1823 UTC and HF radar currents (red) and surface winds (green) from the closest hour (SAR data provided by ESA).....96
Figure 76. SAR image from 26 March 2009 at 1823 UTC (SAR data provided by ESA).....97
Figure 77. SAR image from 5 April 2009 at 0555 UTC and HF radar currents (red) and surface winds (green) from the closest hour (SAR data provided by ESA).....98
Figure 78. SAR image from 11 April 2009 at 1820 UTC and HF radar currents (red) and surface winds (green) from the closest hour (SAR data provided by ESA).....99
Figure 79. SAR image from 14 June 2009 at 0555 UTC and HF radar currents (red) and surface winds (green) from the closest hour (SAR data provided by ESA).....100
Figure 80. SAR image from 3 July 2009 at 0558 UTC and HF radar currents (red) and surface winds (green) from the closest hour (SAR data provided by ESA).....101
Figure 81. SAR image from 23 August 2009 at 0555 UTC and HF radar currents (red) and surface winds (green) from the closest hour (SAR data provided by ESA).....102
Figure 82. SAR image from 27 September 2009 at 0555UTC and HF radar currents (red) and surface winds (green) from the closest hour (SAR data provided by ESA).....103
Figure 83. SAR image from 1 November 2009 at 0555 UTC and HF radar currents (red) and surface winds (green) from the closest hour (SAR data provided by ESA).....104
Figure 84. SAR image from 12 December 2009 at 1820 UTC and HF radar currents (red) and surface winds (green) from the closest hour (SAR data provided by ESA).....105
Figure 85. SAR image from 21 March 2010 at 0555 UTC and HF radar currents (red) and surface winds (green) from the closest hour (SAR data provided by ESA).....106
Figure 86. SAR image from 14 August 2010 at 1820 UTC and HF radar currents (red) and surface winds (green) from the closest hour (SAR data provided by ESA).....107
Figure 87. SAR image from 2 September 2010 at 1823 UTC and HF radar currents (red) and surface winds (green) from the closest hour (SAR data provided by ESA).....108
Figure 88. SAR image from 12 September 2010 at 0555 UTC and HF radar currents (red) and surface winds (green) from the closest hour (SAR data provided by ESA).....109

Figure 89. SAR image from 18 September 2010 at 1820 UTC and HF radar currents (red) and surface winds (green) from the closest hour (SAR data provided by ESA).....110
Figure 90. SAR image from 7 October 2010 at 1823 UTC and HF radar currents (red) and surface winds (green) from the closest hour (SAR data provided by ESA).....111

THIS PAGE INTENTIONALLY LEFT BLANK

LIST OF TABLES

Table 1. Backscatter dependency of ASAR C-band (After Holt, 2004, Figures 2.5, 2.6, 2.8; ASAR Users Guide, n.d.).....11

Table 2. Standard specifications for ASAR IMP and IMS products (After ASAR users guide, Table 2.1).....13

Table 3. The depth of the current observations depends on the depth of influence of the particle motions of the Bragg waves (After Stewart and Joy, 1974).....17

Table 4. Characteristics and specifications of ESA's ENVISAT ASAR C-band and HF CODAR installed in Central California (After Canada Centre for Remote Sensing, n.d., Graber et al., 1996; McCandless & Jackson, 2004, ESA portal, http://www.esa.int).....21

Table 5. Characteristics of Ocean Features on SAR imagery (From Holt, 2004, Table 2.1).....22

Table 6. Example of multilooking tests performed on IMS products.....31

Table 7. Ocean and land stations for wind measurements (After NOAA, MBARI, NPS-MR).....36

THIS PAGE INTENTIONALLY LEFT BLANK

LIST OF ACRONYMS AND ABBREVIATIONS

AATSR	Advanced Along Track Scanning Radiometer
AP	Alternating Polarization mode
ASAR	Advanced Synthetic Aperture Radar
CCRS	Canada Centre for Remote Sensing
CCS	California Current System
CencalCurrents	Central California Currents
CeNCOOS	Central and Northern California Ocean Observing System
COCMP	Coastal Ocean Currents Monitoring Program
CODAR	Coastal Ocean Dynamics Applications Radar
CTDP	Centre de Traitement Doris Poseidon
DEM	Digital Elevation Model
DORIS	Doppler Orbitography and Radiopositioning Integrated by Satellite
EM	Electromagnetic
ENVISAT	Environmental Satellite
ERS	European Remote Sensing Satellite
ESA	European Space Agency
GM	Global Monitoring mode
HF	High Frequency
HH	Horizontal Transmit / Horizontal Receive
HV	Horizontal Transmit / Vertical Receive
IM	Image Mode
IMP	Image Mode Precision image
IMS	Image Mode Single-Look Complex image

IR	Infra-Red
IS	Image Swath
MBARI	Monterey Bay Aquarium Research Institute
MERIS	Medium Resolution Imaging Spectrometer
MODIS	Moderate Resolution Imaging Spectroradiometer
MUSIC	Multiple Signal Classification
MW	Micro Wave
NDBC	National Data Buoy Center
NEST	Next ESA SAR Toolbox
NOAA	National Oceanic and Atmospheric Administration
NPS-MR	Naval Postgraduate School - Meteorology Department
NRCS	Normalized Radar Cross Section
NRL	Naval Research Laboratory
OSCR	Ocean Surface Current Radar
RAR	Real Aperture Radar
ROI	Region of Interest
SAR	Synthetic Aperture Radar
SLC	Single Look Complex
SRGR	Slant Range to Ground Range
SST	Sea Surface Temperature
UTC	Coordinated Universal Time
VH	Vertical Transmit / Horizontal Receive
VV	Vertical Transmit / Vertical Receive
WS	Wide Swath mode
WV	Wave mode

ACKNOWLEDGMENTS

I would like to thank my advisor, Dr. Jeffrey Paduan, for his guidance and good judgment through this thesis process. I'm also grateful to Mr. Benjamin Holt for his helpful comments and insightful expertise and to Mr. Mike Cook for the endless, invisible programming work of putting everything together. This project could not have been done without their wisdom and dedication.

All SAR data was provided by the European Space Agency to whom I owe great appreciation. I would also like to thank several people who contributed with their know-how and data including: Dr. Fred Kruse, Dr. Philip Durkee, Dr. Leslie Rosenfeld, Dr. Timour Radko, Dr. John Ryan, Mr. Richard Lind, Mr. Richard Cook and Mr. Robert Creasey.

Finally, I'd like to express my thankfulness to my family and friends who have supported and encouraged me throughout the years.

THIS PAGE INTENTIONALLY LEFT BLANK

I. INTRODUCTION

A. MOTIVATION AND BACKGROUND

Knowledge of the oceans is important for all strands of human life, impacting populations economically, socially, politically and strategically. Civilization does not know the world without water, and man's own survival may depend on an understanding of the global ocean and its processes. Navigation, maritime transportation, energy and resource exploitation, naval military operations, search and rescue, oil spill response, recreational activities, and offshore engineering all depend on some degree of information about the ocean. Recent awareness of climate changes has focused media and popular attention on environmental concerns and triggered the hunt for answers. For the last 150 years, oceanographic data have been collected with a large contribution of *in situ* data, particularly after the 1950s and satellite ocean measurements starting in the 1970s (Talley et al., 2011, Chapter 1).

Nowadays, more and more sophisticated sensors are available for monitoring and deciphering coastal and oceanic processes as near to real time as possible. Remote sensing methods are critical in these efforts. Ocean remote sensing is defined as the use of electromagnetic radiation to acquire information without physically contacting the target or event under investigation (Martin, 2004). Along with a wide range of sensors, high frequency (HF) radar and synthetic aperture radar (SAR) are of special interest in this present study.

In North America and, in particular, along the central California coast, there exists a large data set of surface currents derived from HF radar observations that can be overlapped with coverage from modern SARs. The combination of both remote sensors has the potential to lead to a high-resolution map of surface features extending from coastline to approximately 100 km offshore.

This study aims to analyze an ensemble of 31 SAR images distributed over a wide range of wind conditions over the period 2007–2010, overlap them with corresponding HF radar-derived surface current maps, characterize the wind speed conditions for each

image, and identify, where possible, the detected features and the differences and similarities in how these features are resolved (imaging mechanisms) in each distinct data set. The different imaging mechanisms include advection of surfactants, convergence/divergence zones, or cross correlation between SAR backscatter, winds, and surface currents on the scale of the HF radar observations (Clemente-Colon & Yan, 1999; Holt, 2004; Lyzenga, Marmorino & Johannessen, 2004). Other relevant questions are addressed, such as: What kind ocean features are detectable by SAR for different wind conditions? What are the thresholds for which SAR imagery has poor or no backscatter difference and, thus, does not allow the visualization of ocean features? What is the interval of optimal wind conditions to retrieve certain ocean features in SAR imagery?

B. CONTRIBUTIONS

This thesis presents a first step towards understanding coastal phenomena as perceived by a synergetic overlapped product of HF radar-derived surface currents and SAR imagery of the oceanic region between Point Reyes, north of San Francisco, and Point Sur, south of Monterey (Figure 1).

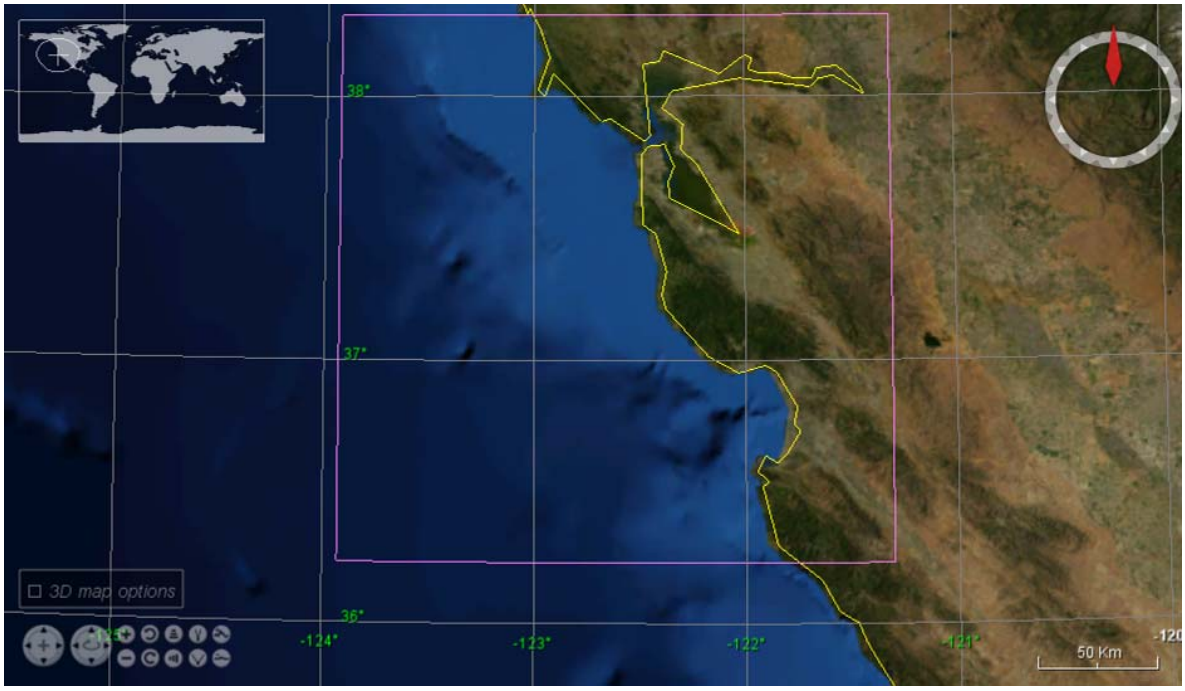

Figure 1. Oceanic region of interest included in the square (After Eoli-sa ESA)

C. THESIS ORGANIZATION

Chapter II reviews sensor background and characteristics of both SAR and HF radar. Chapter III describes the data and methodology of retrieving HF surface currents and SAR imagery, including the work flow associated with the European Space Agency's (ESA) processing software Next ESA SAR Toolbox (NEST). Description of *in situ* measurements from National Oceanic and Atmospheric Administration (NOAA) and Monterey Bay Aquarium Research Institute (MBARI) buoys is presented in this chapter, as well, and the process of overlapping HF, SAR and wind data is demonstrated. In chapter IV, results are assessed and a discussion of the limitations is presented. Chapter V summarizes the key results, concludes, and offers recommendations pointing toward areas of further research. The appendices contain all SAR imagery and HF products analyzed. Supplementary images are maintained online by Naval Postgraduate School (NPS) at http://calhoun.nps.edu/.

THIS PAGE INTENTIONALLY LEFT BLANK

II. BACKGROUND

This chapter presents the background of both SAR and HF radar, focusing on these remote sensors' products used in the present study. The relevant characteristics and specifications are analyzed and the most important concepts are briefly defined.

A. SAR

1. SAR Background and Ocean Applications

Spaceborne SAR took its first solid steps in 1978 with the launch of SEASAT, providing an exclusive and detailed view of the sea's surface (Fu & Holt, 1982). Wind conditions, especially wind intensity, contribute greatly to the surface roughness from which backscatter differences permit the visualization of a variety of ocean features, such as internal waves, surface waves, eddies, shallow bottom topography, ocean currents, oil slicks, upwelling events, rainfall, ships and ship wakes (Martin, 2004). SAR is capable of imaging the earth's surface with fine resolution, on the order of meters, and doing it independently of cloud cover and solar illumination.

The Environmental Satellite (ENVISAT; Figure 2) is the improved follow-on from the European Remote Sensing Satellite (ERS) -1 and -2 missions. Launched in 2002, ENVISAT has been globally and regionally sensing the earth and providing data to scientific and application users through a vast payload instruments, such as Advanced SAR (ASAR), Advanced Along Track Scanning Radiometer (AATSR), Medium Resolution Imaging Spectrometer (MERIS), and Doppler Orbitography and Radiopositioning Integrated by Satellite (DORIS), among others. ENVISAT does not have a scatterometer onboard as did the ERS missions. ASAR's new capabilities include beam steering for acquiring images with different incidence angles, dual polarization, and wide swath coverage through ScanSAR (http://www.esa.int).

Figure 2. ESA's ENVISAT (From ESA).

2. What is SAR?

SAR is a high resolution, side-looking imaging sensor that illuminates the surface of the earth via active micro wave (MW) frequencies (Figure 3) and the retrieved backscatter measurements from the detected surface varies by surface roughness and dielectric constant. Since its active radar pulse illuminates the surface, sunlight is not required, thus providing 24-hour coverage. Through a full transmitting C-band with frequency of 5.3 GHz and corresponding wavelength of 5.6 cm (see Figure 3 and Table 1), ENVISAT's ASAR collects earth's information in nearly all weather conditions. This constitutes a direct advantage over visible or infrared (IR) frequency radiometers that only provide good data with a cloud-free atmosphere (Martin, 2004; McCandless & Jackson, 2004).

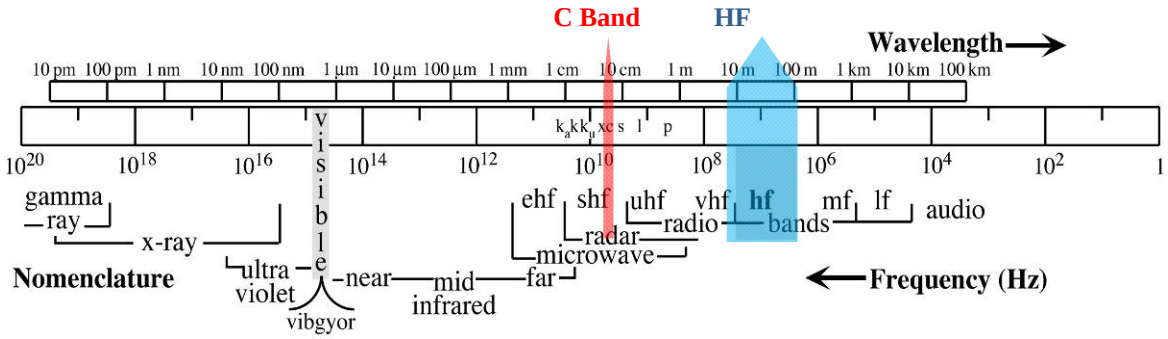

Figure 3. The Electromagnetic Spectrum (After Paduan & Graber, 1997)

3. How Does SAR Work?

In a basic approach, SAR follows the same principles as real aperture radar (RAR) if synthetic aperture is not considered. It calculates the distance from the radar to an object by multiplying the speed of light ($c = 3 \times 10^8$ m/s) and one half of the measured time between transmission and reception of the electromagnetic (EM) wave that illuminates the object. The returned energy received by the radar is called backscatter. Backscatter coefficient or normalized radar cross section (NRCS) is dimensionless, expressed by σ_o in decibels (dB), and depends mainly on wind and radar parameters (see Table 1).

Synthetic aperture is the mechanism that enables SAR to achieve its fine resolution, on the order of 30m for ASAR image mode (IM) products. As illustrated in Figure 4, synthetic aperture consists of a virtual augmentation of the antenna size to the equivalent distance travelled by the satellite while illuminating the target and, then, integrating the time history of the precisely measured amplitude and phase (coherent radar). RAR azimuth resolution is set by the azimuth beam width, while SAR improves azimuth resolution to shorter than the antenna length through signal processing (Henderson & Lewis, 1998; Martin, 2004). McCandless and Jackson (2004) define SAR as a mix of radar and signal processing techniques, greatly boosting the spatial resolution.

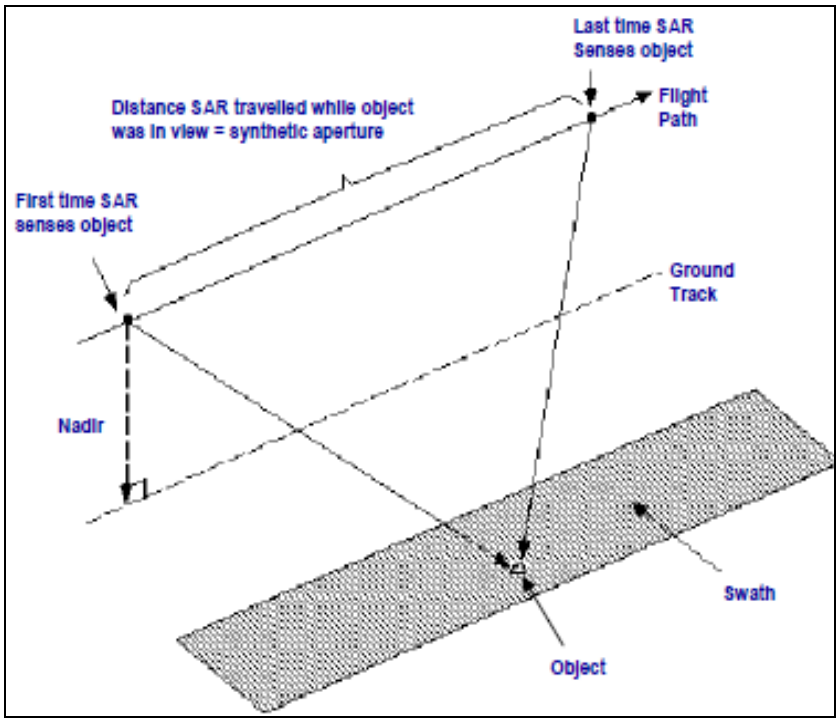

Figure 4. Concept of synthetic aperture (After Canada Centre for Remote Sensing, n.d.)

4. Bragg-Resonant Backscatter and Surface Roughness

For ASAR typical incidence angles of 15° to 45°, resonant (Bragg) scatter dominates over specular scatter, and the received backscatter is enhanced due to coherent combinations of signals reflected back from the small-scale surface wave field. Over the ocean, Bragg scatter requires reflecting features on the sea surface within the same order of wavelength as the radar waves being utilized. Highlighted in Figure 5a, the resonant wavelength is given by Equation 1:

$$\lambda_B = \frac{\lambda_r}{2\sin\theta} \tag{1}$$

where λ_B is the sea surface wavelength, λ_r is the EM wavelength and θ is the incidence, or viewing angle (off-nadir). The waves matching this criterion are on the order of centimeters or less, corresponding to the shorter surface waves called capillary waves whose restoring force is surface tension.

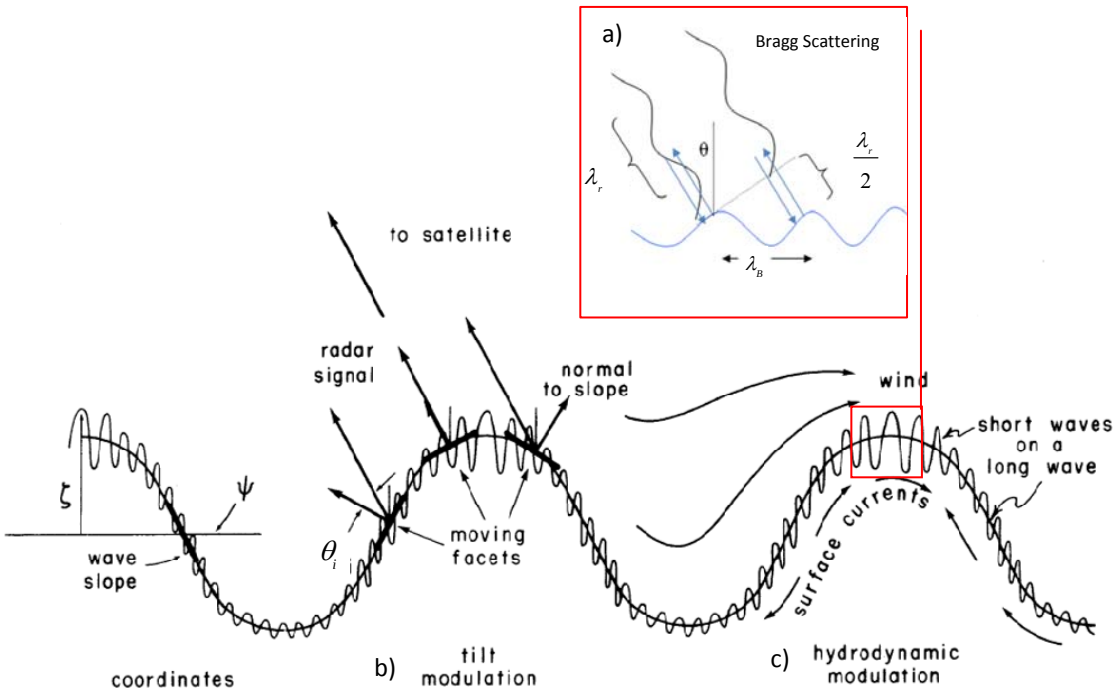

Figure 5. Illustration containing a) Bragg scattering mechanism; b) Tilt modulation – long wave pattern modifies short-wave local incident angle, and c) hydrodynamic modulation – surface currents affect distribution of short waves along a long wave. ζ is the surface elevation and ψ is the wavenumber spectrum. (After Stewart, 1985, Figure 13.6; Canada Centre for Remote Sensing, n.d)

Detectable variations of σ_o are sensed by SAR due to modification of Bragg waves by larger waves (swell), small-scale wind patterns, current shear, bottom-current/wave interaction, oil slicks, ships, and ship wakes.

Some of the oceanic mechanisms that enhance or suppress backscatter, hence modulating Bragg scattering, include tilt and hydrodynamic modulations (Stewart, 1985; Holt, 2004) as well as surfactant damping and velocity bunching.

Tilt modulation, illustrated in Figure 5 b), occurs when a long wave pattern modifies the slope of short waves, tilting them differently over the crests and the troughs, and thus causing a change in local incidence angle, θ_i, (or moving facets) along the longer propagating wave.

Hydrodynamic modulation, shown in Figure 5 c), occurs when Bragg scale waves change due to wave orbital velocities. Here Bragg waves accumulate on crests and stretch out on troughs creating convergence and divergence zones, respectively.

Surfactants damping lowers the surface tension, causing suppression of Bragg scale waves and, thus, enhancing surface smoothness. Surfactants are surface active agents that can be either biogenic or mineral oils that lower the surface tension.

Velocity bunching is an ingredient of the SAR system caused by a non-stationary ocean surface, yet it does not influence quantitatively the returned energy. The natural displacement of the waves while the sensor is orbiting will induce an additional Doppler offset, in the satellite's line-of-sight component (radial), translated into a shift in positioning of azimuth-travelling waves, as in the train-off-the-track example in Rufenach, Shuchman and Lyzenga (1983).

Backscatter depends greatly on the geometric and electrical characteristics of the target. Over the water, the backscatter is mainly a function of the surface roughness caused by capillary waves which in turn are induced by local wind stress. The electrical properties of the target also contribute to the returned energy; they are expressed by the dielectric constant ε_c (Table 1), which expresses the reflectivity and conductivity of a medium. The dielectric constant of the ocean water is relatively high and varies by temperature, salinity, and frequency (Holt, 2004).

Wind variation is of extreme importance in generating surface roughness. Under normal meteorological conditions, high wind speeds (up to ~15 m/s) create greater backscatter and thus brighter imagery, whereas winds greater than 15 m/s cause ocean clutter to mask surface features in SAR imagery. For wind speeds below ~2-3 m/s the scattering surface will be low, thus providing little backscatter and dark imagery. Therefore, the optimal wind interval for better responsiveness to surface roughness is 2 to 15 m/s (Johannessen et al., 1996; Clemente-Colon & Yan, 1999; Holt, 2004). Upwind or downwind satellite looks also reflect more energy than crosswind looks. Table 1 gives a general description on backscatter dependency applied to ASAR C-band.

Table 1. Backscatter dependency of ASAR C-band (After Holt, 2004, Figures 2.5, 2.6, 2.8; ASAR Users Guide, n.d.)

	σ_o = NRCS or Backscatter coefficient	After Holt, 2004, Figures 2.5, 2.6, 2.8
Wind direction	**Upwind & downwind** have higher σ_o than **crosswind.** Upwind has higher σ_o than downwind.	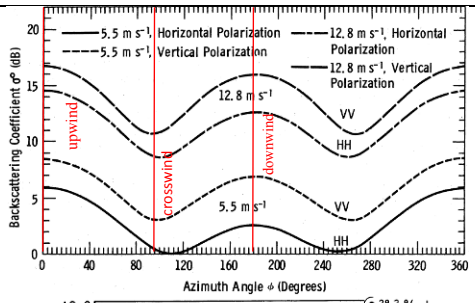
Wind speed	As wind increases, σ_o increases. Cut off at 2 m/s and 15m/s (see Table 2 for detailed information).	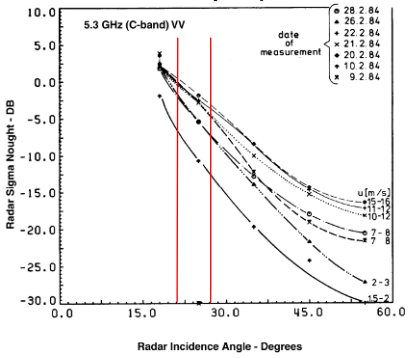
Radar parameters	**Ocean radar return with Incidence angle** (15° < θ < 45°): Increasing θ decreases σ_o. The data set in the present study uses images with incident angles 19.2° < θ < 26.7°.	
	Polarization - VV returns more σ_o than other combinations.	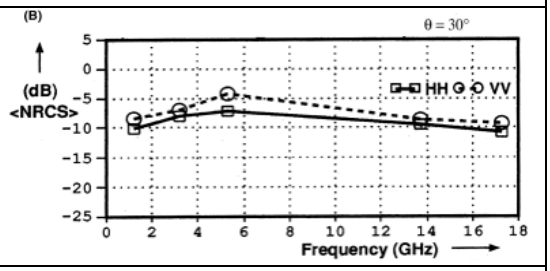
	Frequency - Maximum σ_o at ~5.5GHz.	
Electric properties	Dielectric constant ε_c: The higher ε_c, the higher is σ_o. ε_c varies by temperature, salinity, and frequency.	

*VV – Vertical transmit and vertical receive polarization (see Figure 6)
**HH – Horizontal transmit and horizontal receive polarization

5. ASAR Polarization

For purposes of studying surface roughness caused by wind-driven capillary waves, VV polarization has a larger backscatter coefficient than other combinations

(ASAR Users Guide, n.d.; Holt, 2004). All ASAR imagery contained in this study has VV (vertical transmit – vertical receive) polarization (Figure 6). For in-depth information on ASAR polarization, the reader is referred to ASAR Users Guide, (n.d.).

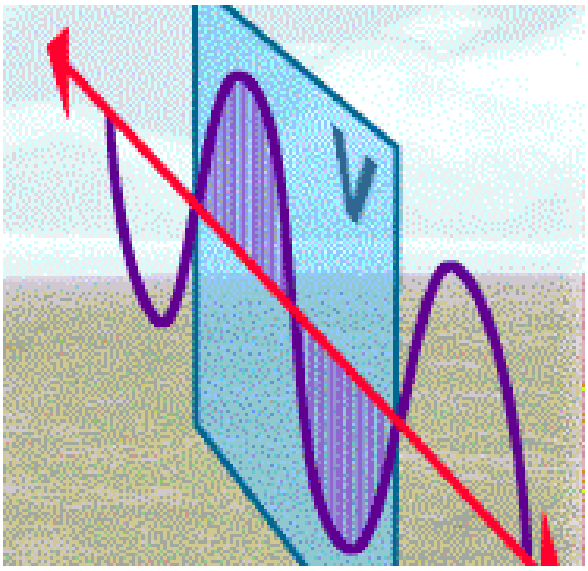

Figure 6. VV Polarization (From ASAR Users Guide, n.d., Figure 1.20)

6. ASAR Measurement Modes

ASAR can operate in 5 distinct measuring modes with varying incidence angles and swath widths:

- Image Mode (IM, see Figure 7)
- Alternating Polarization Mode (AP)
- Wide Swath Mode (WS)
- Global Monitoring Mode (GM)
- Wave Mode (WV)

As defined in ASAR Users Guide (n.d.), "IM products are high-resolution, narrow swath products based on data acquired at one of seven subswaths. Swath widths range between approximately 56 km (swath 7 – IS7) and 100 km (swath 1 – IS1) across-track. Spatial resolution of approximately 30 m (for Precision IM product)." SAR imagery in this study focuses on IS2 with incidence angles 19.2°- 26.7°.

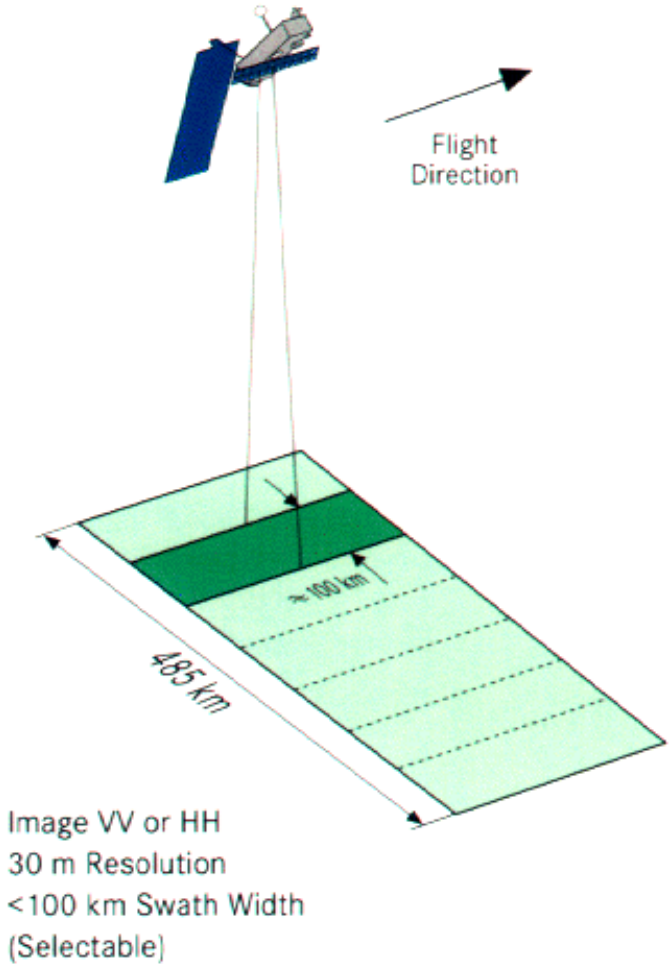

Figure 7. Image Mode (After ASAR users guide, n.d., Figure 1.10)

The present research exploits Level 1b IM products, particularly Image Mode Single-Look Complex image (IMS) and Image Mode Precision image (IMP).

Table 2. Standard specifications for ASAR IMP and IMS products (After ASAR users guide, Table 2.1)

Product ID	**Nominal Resolution(m) (range x azimuth)**	**Nominal Pixel Spacing (m) (range x azimuth)**	**Approx.Coverage (km) (range x azimuth)**	**Equivalent No. of Looks**
IMP	30 x 30	12.5 x 12.5	56-100 x 100	> 3
IMS	9 x 6 - -	natural	56-100 x 100	1

B. HF RADAR

1. HF Background and Ocean Applications

High frequency (HF) radio bands have been providing evidence of their value throughout the last three decades. They work by exploiting Bragg scattering information related to ocean surface waves and currents as described in Barrick, Evans and Weber (1977) and later demystified by, among others, Paduan and Graber (1997) and validated in Chapman and Graber (1997) and Paduan and Rosenfeld (1996).

Radars using HF can be divided into two major configurations: direction- finding and beam forming (a phased-array system). Coastal Ocean Dynamics Applications Radar (CODAR) utilizes direction-finding mode, while Ocean Surface Current Radar (OSCR) uses beam-forming. More versatile Wellen Radar (WERA) units can operate in either configuration (Paduan and Washburn, 2012; Teague, Vesecky & Fernandez, 1997).

Ocean surface-current maps analyzed in this study are derived from CODAR-type HF radar using SeaSonde units. These employ a compact antenna with direction finding configuration and use the Multiple Signal Classification (MUSIC) algorithm to determine ocean surface-current bearings (Paduan & Graber, 1997).

Several applications benefit directly from ocean surface currents mapped through long-time scales over large, spatial ocean coastal areas, such as data assimilation in ocean circulation models accounting for search and rescue operations, oil spill response, harmful algal bloom monitoring, larvae transport, natural resource exploitation, tsunami warning, surface-tidal current mapping, and wastewater discharge (Paduan & Washburn, 2012).

2. What is HF Radar?

Earlier defined in Barrick et al. (1977), "this instrument [HF radar system] deduces current velocity from the echoes scattered continuously from the ocean waves; buoys and drifters are not required." HF sensors are shore-based stations using EM radio waves with real aperture to provide real-time, 24-hour, all-weather reflectivity of ocean wave spectra. Several sensors are required to provide overlapping detection regions

necessary to determine direction. The main product derived from the spectra is a 2-D map of ocean surface currents with a horizontal resolution of ~3km, spanning up to 100km from near a coastline. Besides current maps, the energy density spectrum generated by this remote sensor (sampled in Figure 8), allows retrieving wind direction and sea state (significant wave height, mean direction and peak period; Graber & Heron, 1997).

3. How Does HF Radar Work?

HF systems operate at frequencies ranging from $f = 3$ to 50 MHz (from http://www.codar.com/), which corresponds to radio wavelengths, λ_r, between ~6-100m (Equation 2); they exploit Bragg scattering energy echoes from surface gravity waves (similar to SAR), where the wavelength of the Bragg waves, λ_B, is one-half of λ_r (Equation 3) i.e.,

$$\lambda_r = \frac{c}{f} \tag{2}$$

where speed of light $c = 3 \times 10^8$ m/s

$$\lambda_B = \frac{1}{2}\lambda_r \tag{3}$$

In a simple approach, the method to retrieve radial surface currents takes into account the relationship between the Doppler frequency shift of resonant backscatter, $\pm f_{Bragg}$, and the speed of deep-water gravity waves, c_o (Equations 4 and 5) plus additional displacement, Δ_f, caused by the underlying current field. Equation 6 shows the Doppler principle, where V_r is the component of surface current along the radial direction (Barrick et al., 1997; Paduan and Washburn, 2012; Thompson, Graber & Carande, 1994).

$$f_{Bragg} = \frac{2c_o}{\lambda_r} \tag{4}$$

$$c_o = \sqrt{\frac{g}{k}} \tag{5}$$

where g is the gravitational acceleration and $k = \frac{2\pi}{\lambda_B}$ is the wavenumber

$$\Delta_f = \frac{2V_r}{\lambda} \tag{6}$$

The expected Doppler shift due to Bragg waves, f_{Bragg}, is known so any additional Doppler, Δ_f, is attributed to the current (Paduan & Graber, 1997). Figure 8 illustrates a typical Doppler spectrum for OSCR-type HF radar. Spectra from direction-finding radar (CODAR) have wider Bragg peaks (Paduan & Washburn, 2012).

Gathering information from two or more HF radar stations, provided the surveyed area overlaps with good geometry, allows the estimation of current vectors and, thus, construction of surface maps of current speed and direction.

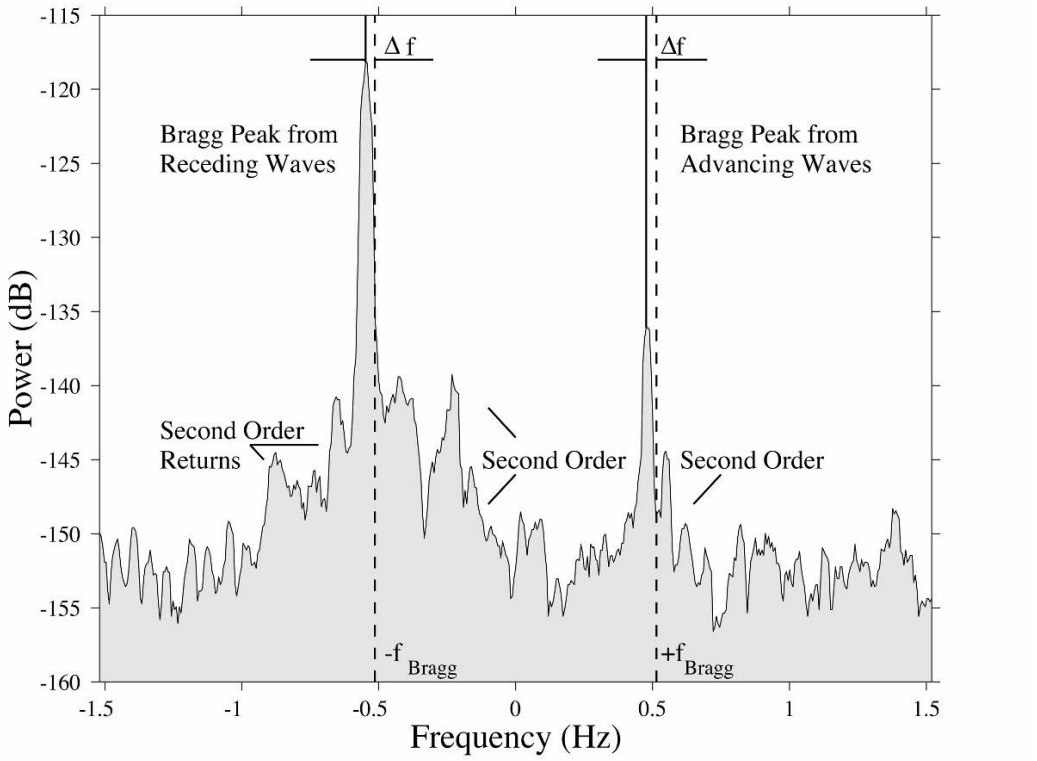

Figure 8. Typical Doppler spectrum collected by an OSCR system, showing prominent Bragg peaks due to waves advancing toward and receding from the receiver. Bragg frequencies, $\pm f_{Bragg}$, correspond to positions of no-currents shown by the vertical dashed lines. Δ_f is the additional Doppler shift related to ocean currents (after Graber et al., 1996; Paduan & Graber, 1997).

Despite the fact that HF radio waves don't literally penetrate the sea surface, they measure the backscatter of short gravity waves, moving with deep-water phase speed, that are influenced by long waves and currents beneath. A similar process at different spatial scales is SAR's hydrodynamic modulation, depicted in Figure 5c. The interaction of the orbital motion of individual particles with long waves and currents drives the effective depth of Bragg wave influence, which is not more than two meters as shown in Table 3.

Table 3. The depth of the current observations depends on the depth of influence of the particle motions of the Bragg waves (After Stewart and Joy, 1974)

Frequency (MHz)	**Depth of influence (m)**
4.8	~ 1.5
6.8	~ 1.2
13.4	~ 0.8
21.8	~ 0.5

4. Site Description

The importance of installing HF radar systems close to the shoreline to allow maximum range and benefit from surrounding wet and sandy soils, which enhances signal strengths, is pointed out in Paduan and Graber (1997). Radio interference, high sea states and dry or rocky terrain around sensors constitute limitations to the received power.

Locations of CODAR HF radar antennas used in the present study are illustrated in Figure 9. All 16 systems are managed and maintained by local academic institutions (http://www.cencoos.org/index.html).

Figure 9. Site localization of HF antennas (after CeNCOOS http://www.cencoos.org/index.html)

The stations PILR, PSLR and RAGG, seen in Figure 9, operate in the frequency range 4-5 MHz, while MLML works in 24-27 MHz frequency band. All the other HF stations operate in 11.5-14 MHz range. The horizontal range of the CODAR type HF radar in the region of interest (ROI) depends on each station frequency and spans from 30km to 150km from the coastline.

C. SAR AND HF RADAR CHARACTERISTICS

Although both SAR and HF respond to Bragg scattering, they work with distinct frequency bands, detecting different scales of resonant surface waves and, thus, not perceiving the ocean in the same manner. C-band ASAR at 5.3 GHz monitors wind-driven surface roughness caused by capillary waves on the order of 5.6 cm wavelength, with a nominal spatial resolution of 30 m (ASAR Users Guide, n.d.), sensing the skin of the ocean, while HF radar, taking as example a frequency of 12 MHz reflects a short gravity wave field with 12 m wavelength to obtain information about radial currents over an area of 3 km and a penetration depth influence close to 1 m. The wave characteristics in Figure 10 demonstrate the differences between the two surface waves. SAR observations also have the potential to measure Doppler shifts in the radial direction, and preliminary comparisons between HF radar and SAR current measurements appear promising (Danilo et. al., 2007). Yet this approach is not explored in the present study.

Having a reasonable assessment of the overlap between SAR and HF radar products requires understanding the differences between these instruments. For this matter, radiation frequency, antenna footprint, and scattering geometry (Danilo et. al., 2007) assume particular interest, therefore any method to compare both remote sensor products must be cautiously formulated.

Differences in frequency, and the corresponding Bragg waves' sensitivity that these systems respond to, limit the features one can notice simultaneously on SAR images and HF surface-current maps to eddies, fronts, and convergence/divergence zones. Wind speed, the detection of multiple type of surface features, and frequency place boundaries on the quality and level of detail seen in SAR imagery. Table 4 summarizes the most relevant characteristics and specifications of both sensors.

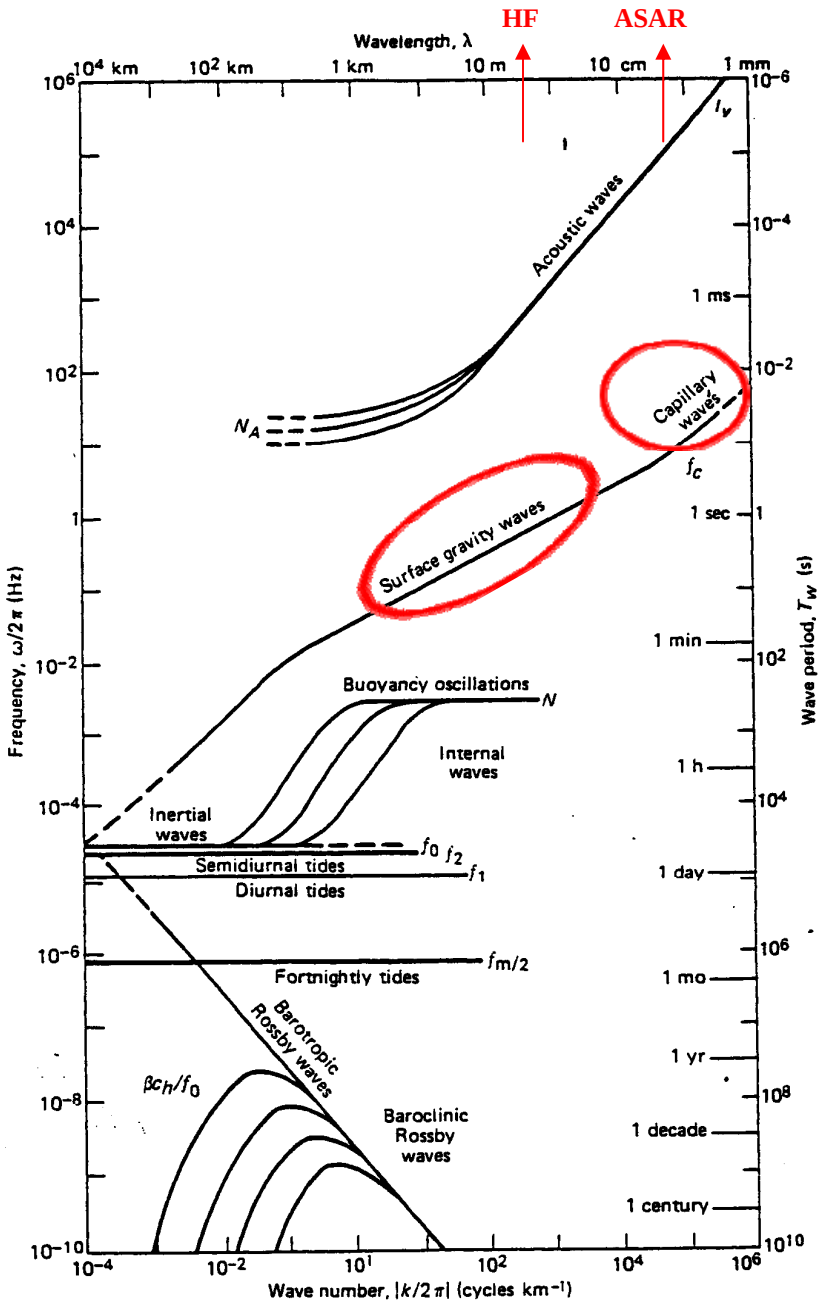

Figure 10. Dispersion diagram and wave characteristics. Capillary waves on an order of centimeters or less and surface gravity waves on the order of tens of meters (After Hasselmann, 1982, Figure 1; Chu, n.d., Figure 6.54).

Table 4. Characteristics and specifications of ESA's ENVISAT ASAR C-band and HF CODAR installed in Central California (After Canada Centre for Remote Sensing, n.d., Graber et al., 1996; McCandless & Jackson, 2004, ESA portal, http://www.esa.int)

PARAMETER	ENVISAT ASAR C-BAND	CODAR HF RADAR
Country	European Space Agency	USA
Operation start date	2002–2012	2006
Frequency	5.3 GHz	4- 27 MHz
Bragg wavelength	5.6 cm	5.5 to 35 m
Spatial Resolution (range and azimuth):	IM, WV and AP: ~ 30m x 30m. WS: ~150m x 150m GM: ~ 1000m x 1000m	Azimuthal: ~5° Range: ~3 km
Radiometric resolution in range	1.5-3.5 dB	N.A.
Radiometric accuracy	0.65 dB	N.A.
No. of looks	IMS = 1 / IMP > 3	N.A.
Swath width	IM and AP: up to 100km WV: 5km WS and GM: 400km or more	N.A.
Range	Variable with mode	30 - 150km
Mean altitude	800 km	Variable with terrain
Orbit velocity	7.45 km/s	N.A.
Incident angle	15° - 45° (For IS2: 19.2°-26.7°)	90°
Inclination	98.55°, sun-synchronous	N.A.
Polarization	VV, HH, VV/HH, HV/HH, or VH/VV	VV Ground-wave
Measurement cycle	N.A.	20 min
Repeat cycle	35 day	NA
Measurement depth	Order of millimeters	< 1m
Accuracy radial current	~1 cm/s	~10 cm/s
Access data	ESA – project proposal	Contact: CeNCOOS.org

*IM – Image mode, WM - Wave mode, AP - Alternating Polarization mode, WS - Wide Swath mode, GM - Global Monitoring mode, IS2 – Image Swath 2.

It is the goal here to identify the imaging mechanisms at work in ASAR imagery that can have a significant expression on HF radar-derived surface-current maps. Given the scales, the different imaging mechanisms are expected to include advection of surfactants, convergence/divergence zones, or cross correlation between SAR backscatter, winds, and surface currents on the scale of the HF radar observations (Clemente-Colon & Yan, 1999; Holt, 2004; Lyzenga et al., 2004). Imaging mechanisms whose content is reproduced in Table 5, can be found in NOAA's SAR marine user's manual chapter 2 (Holt, 2004, Table 2.1).

Table 5. Characteristics of Ocean Features on SAR imagery (From Holt, 2004, Table 2.1)

OCEAN FEATURES					
Feature	**Scale**	**Derived Measurement**	**Imaging Mechanism**	**Range of Wind Speed m s^{-1}**	**Characteristics and Considerations**
Surface Waves	100-600 m wavelength	Wavelength Propagation direction Wave height	Tilt Hydrodynamic Velocity Bunching	3-40	Azimuth-traveling waves may be nonlinear without correction. Other limiting factors include wavelength, wave height and fetch.
Internal Waves	0.3-3 km wavelength	Wavelength Direction Amplitude Mixed layer depth	Convergence/Divergence Surfactants	2-10	Curvilinear packets with multiple waves, decreasing wavelength from front to back. Sensitive to wind conditions, wave crest orientation to platform.
Internal Tides	10-20 km	Wavelength Direction	Interaction of centimeter Waves/Currents/Surfactants	3-7	
Currents and Fronts	1-100 km	Location Shear Strain Velocity	Shear/Convergence Convergence Wind stress Surfactants	3-10 3-10 3-10 3-7	Sensitive to wind conditions. Often multiple mechanisms present simultaneously.
Eddies	1-200 km diameter	Location and source Diameter Velocity Shear Strain	Shear/Convergence Wind Stress Surfactants	3-10 3-10 3-7	Sensitive to wind conditions. Often multiple mechanisms present simultaneously.
Shallow Water Bathymetry	5-50 m depth	Location/change detection Current velocity Depth	Convergence	3-12	Sensitive to wind, current properties, depth.

III. DATA SET AND METHODOLOGY

A. DATA SETS

Ocean data have been collected along the central California coast, from Point Reyes to Point Sur, including the areas around San Francisco and Monterey Bay (Figure 1). These data span the period 2007–2010, and they include HF-derived surface current maps, ENVISAT ASAR imagery and *in situ* wind speed and direction from eight ocean buoys - five from the National Data Buoy Center (NDBC), and three from the Monterey Bay Aquarium Research Institute (MBARI). The area is part of the California Current System (CCS) along the eastern boundary of the north Pacific subtropical gyre (Talley et. al, 2011) which, along with the geomorphology of the coast and bottom topography leads to a wide range of ocean phenomena. San Francisco Bay's narrow entrance accounts for a strong tidal flood and ebb, and Half Moon's and Monterey Bay's geometries often create atmospheric rolls and vortical features. Previous studies conducted in the region demonstrate the large diversity of oceanographic features, such as upwelling events, currents evolving from major wind reversals, mesoscale eddies, current fluctuations dominated by semidiurnal tidal forcing and diurnal sea breeze forcing at shorter timescales (Paduan & Cook, 1997), frontal slicks and localized upwelling shadows (Ryan et al., 2010).

Over the next sections, the method to obtain surface currents from CODAR-type HF radar is described. The process of attaining calibrated and geocoded SAR images is also demonstrated. Overlapping of near-concurrent SAR images and HF radar currents is discussed next and finally quantitative assessment and a validation test is described.

B. HF RADAR SURFACE CURRENT PROCESSING STEPS

Each of the 16 HF radar stations collects Bragg backscatter from surface gravity waves, for different depth influences, in accordance with each unit frequency. The MUSIC algorithm is applied to generate hourly radial currents. Overlapping radials from

two or more units are then attached to a pre-defined spatial grid and combined in *Matlab* or CODAR software to produce total surface current vectors. These vectors are stored in a data server. (M. Cook, personal communication, 2012).

HF current data can be accessed through the Coastal Ocean Currents Monitoring Program (COCMP) webpage (http://www.cencalcurrents.org/data.shtml).

C. SAR DATA SET AND IMAGE PROCESSING FLOW

1. Data Access

SAR archived images are attained through the open software *Eoli-sa* from ESA. *Eoli-sa* is ESA's catalogue interface, which allows users to see browse images, select available data and order the preferred products, as described in the *Eoli* video tutorial (http://earth.esa.int/EOLi/EOLi.html).

The ordering step requires users to submit a project data proposal at ESA's scientific community by following the "Guidelines for the Submission of Project Proposal" (https://earth.esa.int/web/guest/pi-community/apply-for-data/full-proposal).

In this study, the SAR imagery selection process considered the availability of data for the period and ROI, preferred ASAR modes (see Figures 11 and 12), temporal overlapping with HF products (example in Figure 13), and different wind regimes (see Figure 14).

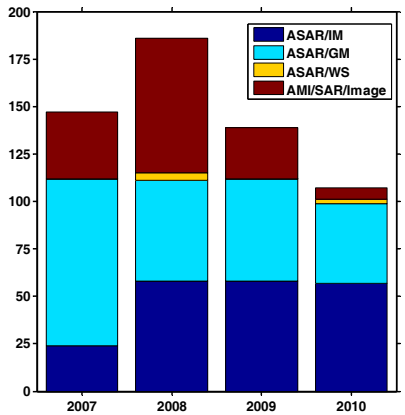

Figure 11. Histogram of images in Eoli-sa catalogue for the period and ROI. The vertical axis represents the quantity of images. In the legend, ASAR is from ENVISAT and AMI/SAR from ERS-2.

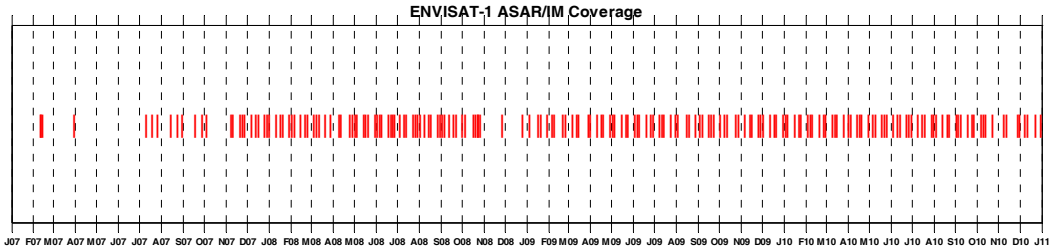

Figure 12. ASAR image mode coverage from period 2007-2010 and ROI. Each vertical red segment represents one image.

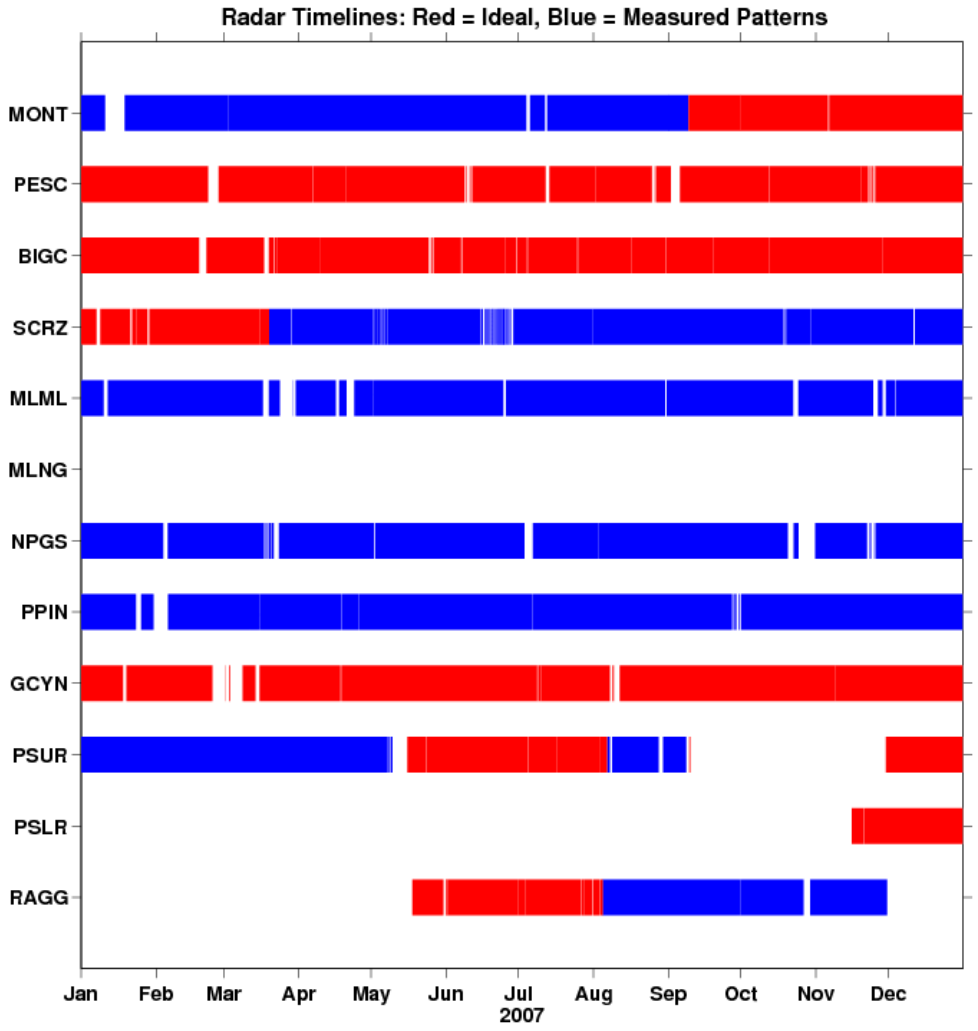

Figure 13. Example of HF radar data available for 2007. Vertical axis shows different HF radar stations illustrated in Figure 9.

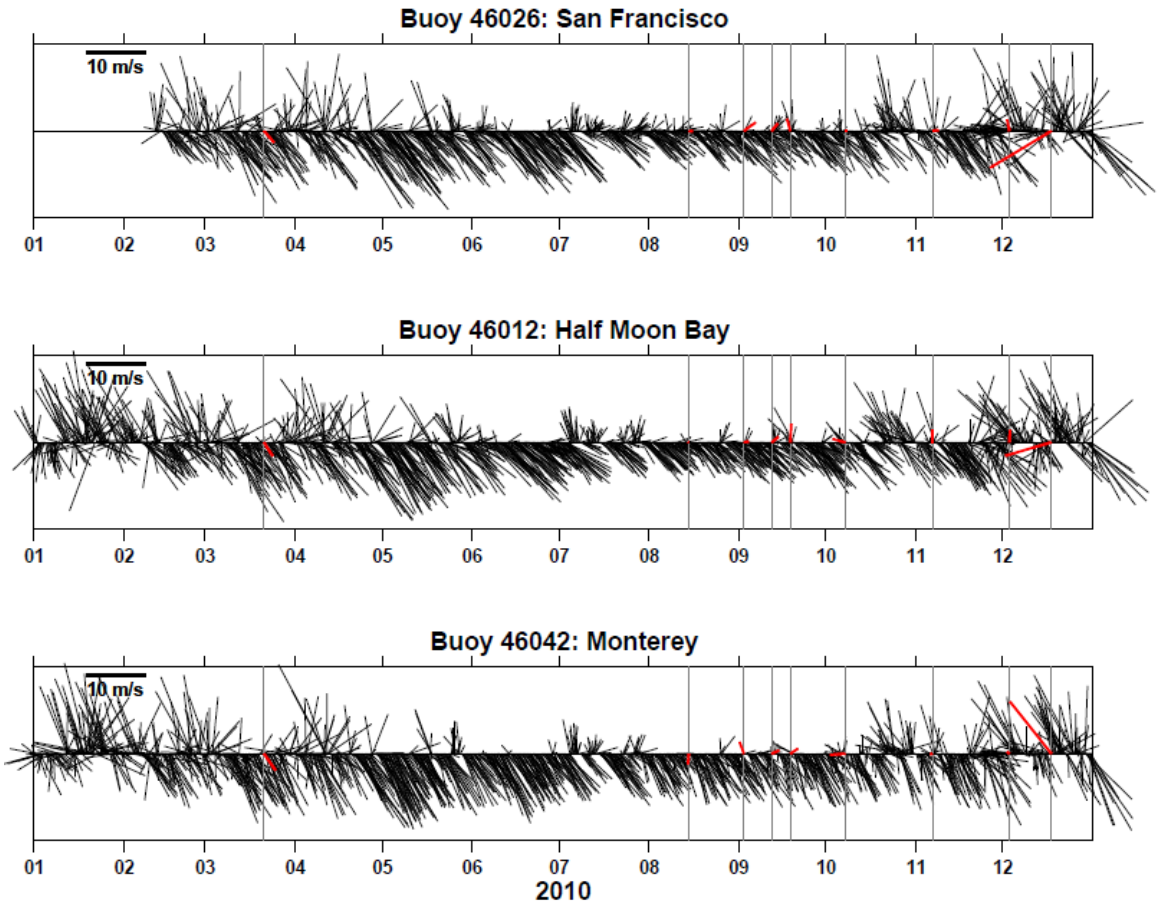

Figure 14. Example of wind plots from in situ buoy measurements on the ROI for 2010. The vertical solid black segments indicate available ASAR image and solid red segments indicate surface wind direction and magnitude at the time of ASAR image formation.

2. Processing Flow

A freely available software package, NEST, was available from ESA for SAr imagery. NEST (Next ESA SAR Toolbox) is used for reading, post-processing, analyzing and visualizing the large archive of data (from level 1) of ESA missions including ERS-1 & 2, ENVISAT, as well as third party SAR-data (NEST User Manuals, n.d.). Level 1b SAR imagery presented in this study was processed with *NEST*, with a nominal resolution of 25 x 25 m for IMS and 16 x 9 m for IMP produts.

Level 1B imagery are geolocated products, derived from Level 0, in which data has been converted to engineering units, auxiliary data has been separated from

measurements, and selected calibrations have been applied to the data. Level 1B products are the foundation from which higher level products are derived" (ASAR Users Guide, n.d.).

The processing flows shown in Figures 15 and 16 are semi-automatic batch procedures built to process single look complex image product (IMS) and detected or precise image product (IMP), respectively.

ESA's ASAR User Guide defines IMS data as a high-resolution, narrow swath product based on data acquired from IS1 to IS7. It is intended for SAR image quality assessment, calibration and interferometric or wind/wave applications. Whereas, IMP product is a multi-look, ground range, digital image suitable for most applications. It is intended for multi-temporal analysis and for deriving backscatter coefficients. (ASAR Users Guide, n.d.).

The batch processing assembles graphs from a list of available SAR and geometry-tool operators in *NEST* software, where the user specifies settings and several options, as well as the source image. The operator's selection and processing chain order depend on the image type and preferred final product. Training tutorials and practical exercises are found in Mahapatra and Hanssen, (2011); Minchella, (2011); Minchella and Costantini, (2011); Veci, Minchela, and Engdahl, (2009); Marinkovic, (2009), as well as the NEST User Manual (n.d.), all available at ESA and *NEST* websites (http://nest.array.ca/web/nest).

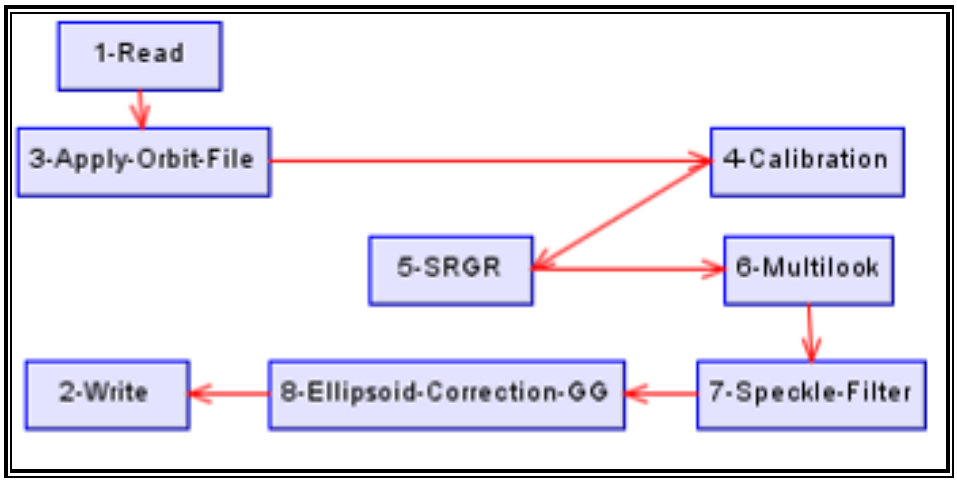

Figure 15. Work flow for SAR IMS with ESA's software NEST.

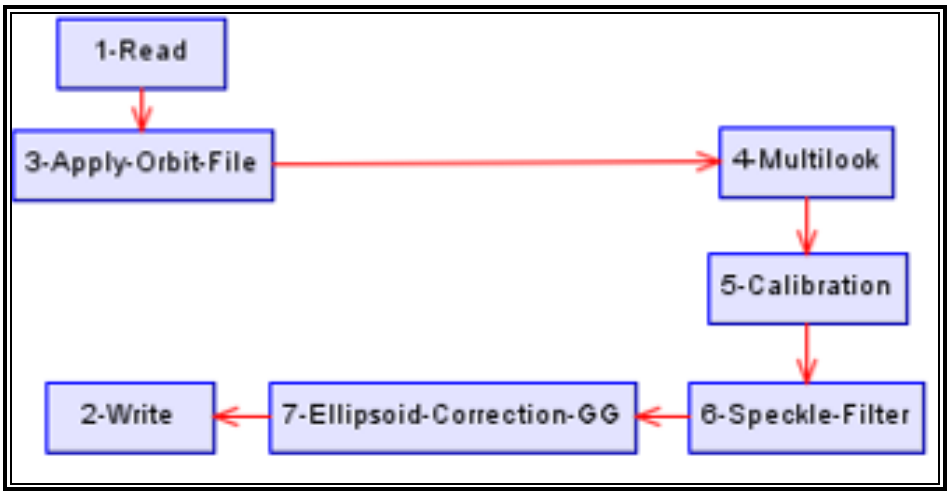

Figure 16. Work flow for SAR IMP with ESA's software NEST.

a. Precise Orbit Files

Precise orbit files constitute an ENVISAT product generated by the Centre de Traitement Doris Poseidon (CTDP) and the Delft University of Technology, which in accordance with ESA's portal is made available days to weeks after the sensing. It's used to refine orbital parameters and update abstracted metadata with more accurate position and velocity (Mahapatra & Hanssen, 2011).

The *Apply orbit file* operator automatically downloads required information from the DORIS server, provided firewall permissions are granted. Alternatively, data can be requested from ESA and manually downloaded by FTP. For comparison purposes a sample image was processed with and without the DORIS precision file. When analyzing ocean surface, no significant changes were found in the SAR image intensity or backscatter.

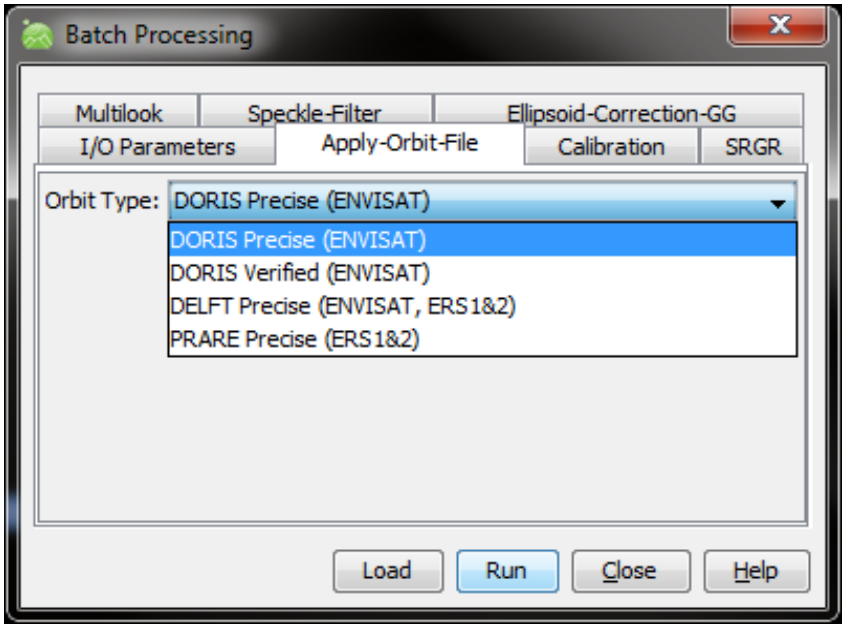

Figure 17. Apply orbit file operator

b. Absolute Calibration

The *Calibration* operator, under radiometric correction, builds a quantitative image where the pixel value directly represents radar backscatter of the scene (Mahapatra & Hanssen, 2011). For solely qualitative assessments, uncalibrated SAR imagery is sufficient (NEST User Manual, n.d.), but the calibration step also provides a visually balance image for viewing.

For IMS, processing options are illustrated in Figure 18, where all bands (I,Q, intensity, phase) are computed by default, if none is selected. The ENVISAT auxiliary file is the latest file option, where the most recent parameters for incident angle, absolute calibration constant, range-spreading loss, and antenna pattern gain are applied. The *Calibration* operator is performed before the *Multilook* operator.

For IMP, the *Calibration* operator is performed after the *Multilook* operator (Figure 16), and the product auxiliary file option is selected since the antenna gain-pattern compensations and range spreading-loss corrections have been applied during the formation of the image (NEST User Manual, n.d.).

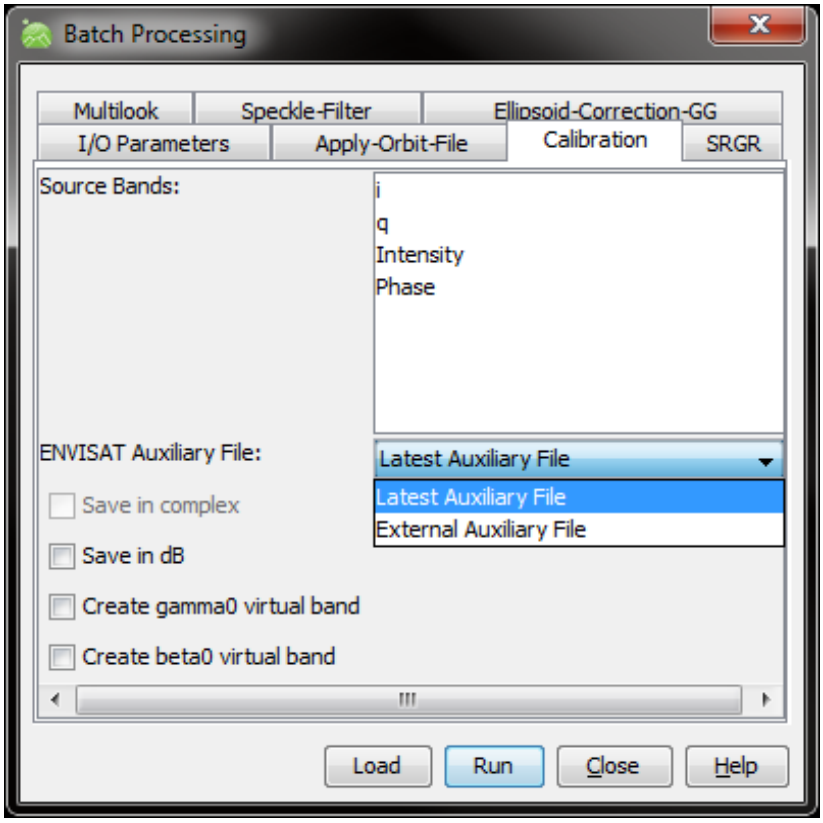

Figure 18. Calibration operator for IMS products.

b. Slant Range to Ground Range Correction

The *Slant range to ground range (SRGR)* operator re-projects the image to ground range spacing from the satellite's nadir along the pre-defined ellipsoid (NEST User Manual, n.d.). It's not the same as geocoding, but does allow the user to have a reasonable interpretation of the SAR image before taking further steps. This transformation is unnecessary if other geometric operators like *Ellipsoid correction* are applied, though it is included at this stage to better adjust results from multilooking tests (see Table 6). In the *SRGR* operator, the order of the warp polynomial is six and the interpolation method is nearest-neighbor, as shown in Figure 19.

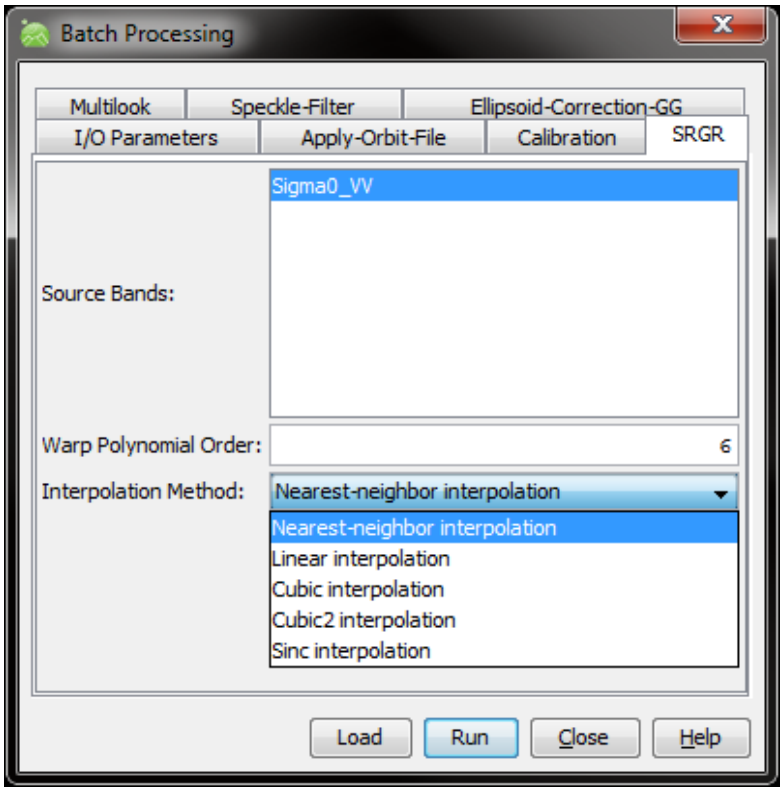

Figure 19. Slant range to ground range operator.

c. Multilook

Multilook is a SAR tool operator that allows reducing the inherent speckle appearance by averaging the pixels (NEST User Manual, n.d.). The number of range and azimuth looks confines ground resolution. More looks lead to pixel blending and less speckle, yet inferior ground resolution. It's also the procedure for obtaining ground-squared pixels in range and azimuth directions. For IMP products, the *Multilook* operator is applied before the *Calibration* operator. Multilooking tests performed on IMS images are presented in Table 6.

Table 6. Example of multilooking tests performed on IMS products.

Number of looks in Range	Azimuth	Resolution	Speckle	Image quality
1	6	< 25 m	Decreasing speckle with increasing number of looks	Less contrast and sharpness with increasing number of looks
2	12	< 50 m		
3	18	< 75 m		

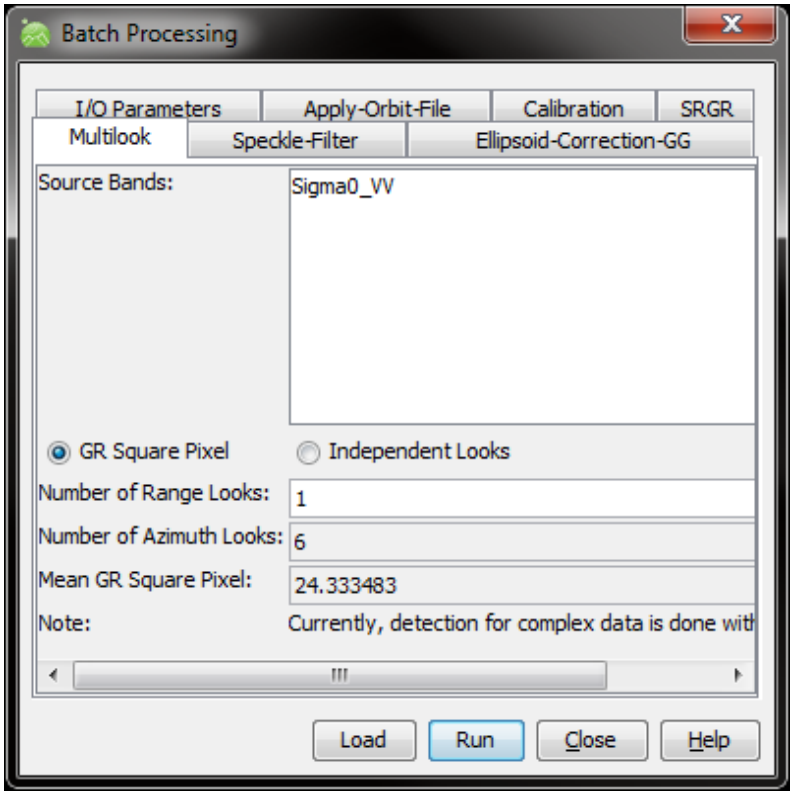

Figure 20. Multilook operator for IMS products.

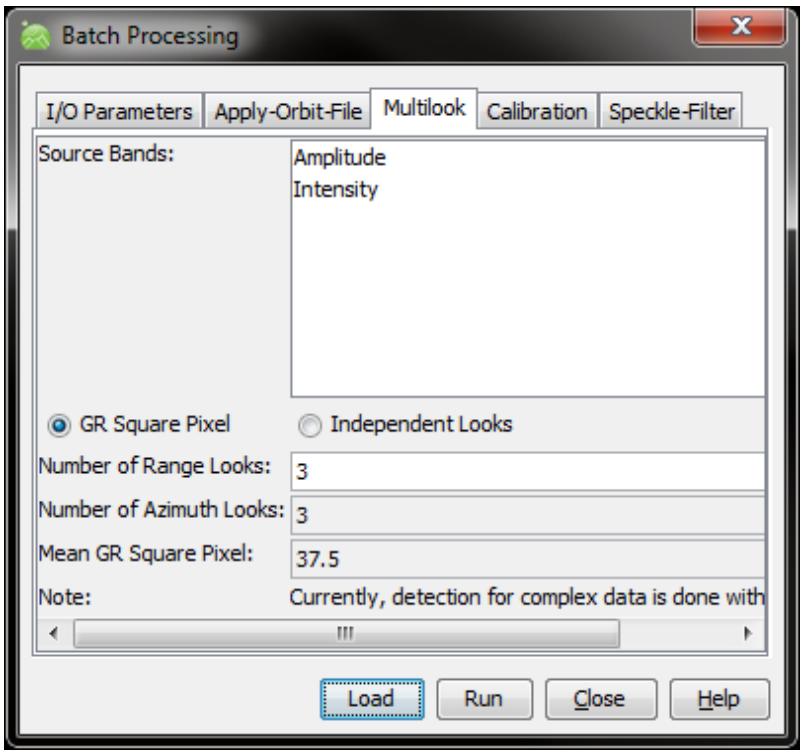

Figure 21. Multilook operator for IMP products.

d. Speckle Noise Filter

Simplistically, speckle is a SAR artifact that results from interference patterns of scattering elements. It's often called the salt and pepper ingredients of an image, referring to constructive and destructive interferences.

The *Speckle filter* operator is intended to reduce the grainy aspect of SAR imagery, thereby increasing the quality of radar coherent images. Techniques available on *NEST* are reviewed in Mansourpour, Rajabi and Blais (2006).

Qualitative filtering tests shows that an adaptive filter Gamma-MAP with a 3x3 filter size decreases radar speckle with minimal effects on spatial characteristics for the actual ASAR data set.

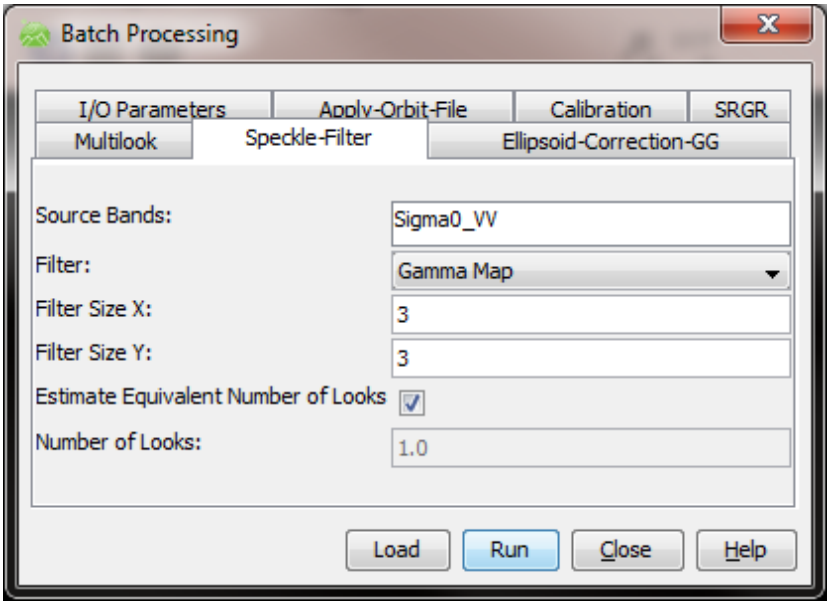

Figure 22. Speckle filter operator

e. Ellipsoid Correction

Ellipsoid correction with the *geolocation grid* method, under geometric tools, corrects the SAR image of distortions caused by topographical variations of a scene and the tilt of the satellite sensor (NEST User Manual, n.d.). The final product is a geocoded image in the projection chosen by the user (WGS 84 in this case). The resampling method is the nearest neighbor.

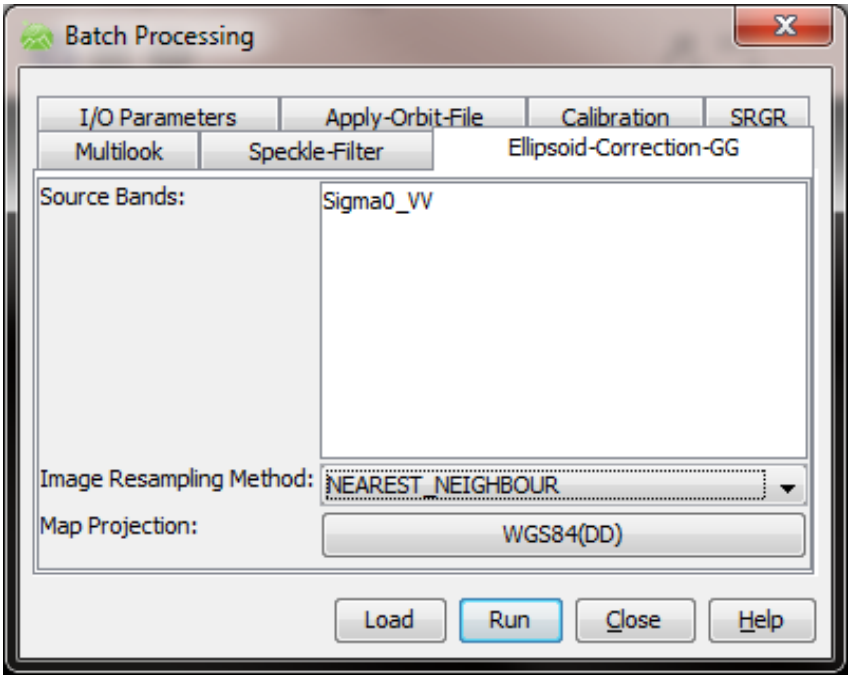

Figure 23. Ellipsoid correction – geolocation grid operator

f. Mosaic

Mosaic is a geometric operator that merges geocoded individual frames (images) into a single composite product. The source images have to be terrain- (or ellipsoid-) corrected and calibrated. The resampling method is nearest neighbor; the number of pixels adjusts automatically to the scene size and is kept the default; and the number of feather (pixels) is five (Figure 24). In the cases where the overlapping regions between frames shows blurring or defocusing results the feather number is increased up to a maximum of 100.

The final product loses the ENVISAT "status" since the mosaic operator does not blend the metadata information from all source images. This might be inconvenient for purposes of performing other *NEST* operations, such as *object detection, oil-spill detection*, or *wind-field estimation*.

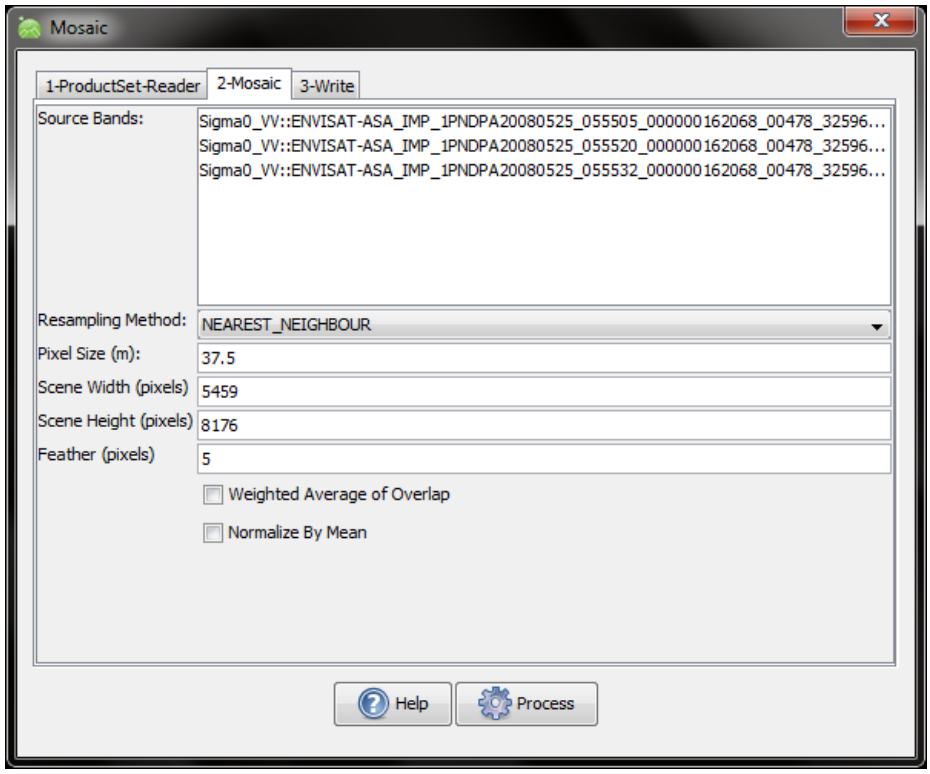

Figure 24. Mosaic operator

D. WIND DATA

Surface wind data is attained from eight buoys and five shore stations, as shown in Table 7. The extraction of measured wind speeds and directions is near-concurrent to SAR imagery and the HF radar products' period of observation. All wind vector components are averaged hourly.

The purpose of retrieving wind measurements over the ROI is: 1) to evaluate the wind speed during the initial selection process of SAR images from ESA's catalog, in order to have quantitative representation of different wind scales; 2) to assess and interpret ocean SAR features given their dependency on wind-induced surface roughness and to avoid ocean cluttered images (Holt, 2004).

In situ measurements from oceanographic buoys are available at NDBC website http://www.ndbc.noaa.gov/ and at MBARI website http://www.mbari.org/. Meteorological data from shore stations is collected through the Naval Postgraduate

School (NPS) Meteorology Department (MR). Table 7 shows wind stations utilized in the study, where actual buoy positions correspond approximately to the ones in the 2007-2010 period.

Table 7. Ocean and land stations for wind measurements (After NOAA, MBARI, NPS-MR)

Station / NDBC number	Sponsor	Position	Anemometer height (sea level)
Buoys			
Bodega / 46013	NDBC	38.242 N - 123.301 W	5 m
San Francisco / 46026	NDBC	37.759N - 122.833W	5 m
Half Moon Bay / 46012	NDBC	37.363N - 122.881W	5 m
Monterey / 46042	NDBC	36.785N - 122.469W	5 m
Cape San Martin / 46028	NDBC	35.741 N - 121.884 W	5 m
M2 / 46093	MBARI	36.69N - 122.41W	4 m
M1 / 46092	MBARI	36.75N - 122.02W	4 m
M0 / 46091	MBARI	36.835N - 121.899W	4 m
Shore stations			
Long Marine Lab	UC Santa Cruz	36.95N - 122.07W	28 m
Range 7 (Fort Ord)	NPS-MR	36.65N - 121.82W	52 m
Monterey Aquarium	Monterey Aqua.	36.62N - 121.90W	31 m
Granite Canyon	NPS-MR	36.44N - 121.92W	24 m
Point Sur	NPS-MR	36.30N - 121.89W	20 m

E. OVERLAP HF RADAR PRODUCTS AND SAR-PROCESSED IMAGES

SAR images are exported with the *NEST* writing tool to a *GeoTIFF* format and overlapped with HF-derived surface current vectors in *Matlab*. The *Matlab* algorithm preserves the SAR image resolution for analysis and interpretation.

F. HORIZONTAL DIVERGENCE TEST

Quantitative assessment of the imaging mechanism (Table 5) present in SAR imagery is challenging and often speculative without any ancillary *in situ* information. This owes to the likely presence of more than one mechanism in the formation of ocean surface features (Holt, 2004). A divergence test is computed in order to validate the qualitative analysis of SAR ocean features and HF radar surface currents.

The goal of the horizontal divergence test is to verify, on the scales of HF radar observations, the existence of positive divergence or negative divergence (convergence) compression zones in HF radar surface currents maps.

It is expected that similar processes to hydrodynamic modulation and internal wave interaction with the surface, causing convergence and divergence zones, also occur at the larger spatial scales of HF radar.

The horizontal divergence, introduced in Sanderson (1995), derives from the continuity equation:

$$\frac{du}{dx}+\frac{dv}{dy}=-\frac{dw}{dz} \tag{7}$$

It is inferred, that horizontal divergence implies replacement of water through upwelling, whereas negative horizontal divergence relates to downwelling.

This test computes the spatial derivative of the velocity fields averaged over one hour and linearly fits the results over an area of 10km radius. The result of the test is a scalar with frequency units and it is expected to be bounded by f and - f, where $f = 10^{-4}$ s^{-1} is the coriolis parameter. The weaker (closer to zero) horizontal divergence values represent small scale phenomena difficult to represent and are removed due to their proximity to the noise levels.

THIS PAGE INTENTIONALLY LEFT BLANK

IV. RESULTS

In this section, examples of overlapping SAR and HF are discussed. This chapter covers some examples of features that are sensed by SAR and provides possible explanations by looking at the ocean dynamics. The complete set of the SAR images with the near-concurrent HF radar and wind products is shown in Appendix A, and notes on the possible features are described in Appendix B.

The different imaging processes for SAR ocean-feature detection, as described in Clemente-Colon and Yan (1999); Holt (2004); and Lyzenga et al. (2004) include:

- Advection of surfactants where accumulation of oil slicks indicate current convergence and a darker SAR surface.
- Convergence/divergence zones associated with the interaction between the direction of the long-wave field and the type of surface current, which can in turn lead to divergence, convergence, or shear.
- Atmospheric instability effects where colder air over warmer water causes an increase in surface wind stress due to convective instabilities, thereby enhancing the backscatter in the presence of warmer ocean surface. When the temperature gradient is large enough, 2°C or more, the frontal signatures become more evident.

For atmospheric features seen in SAR imagery, the main imaging mechanism is wind stress (Monaldo & Beal, 2004). Atmospheric features identified in the present data set are roll vortices and gravity waves (see Appendix).

In order to better interpret the ROI's coastal ocean dynamics in the imagery, Moderate Resolution Imaging Spectroradiometer (MODIS) derived products are assessed. Sea Surface Temperature (SST), True Color and Chlorophyll Concentration maps are, when available, compared with the data set. All MODIS data is attained from Bio-Optical/Physical Processes and Remote Sensing Section of Naval Research Laboratory (NRL) at http://www7240.nrlssc.navy.mil/.

The following nine subsections present examples of different ocean features and imaging mechanisms found on the actual data set. Some atmospheric features depicted by C-band SAR are also mentioned. All SAR images contain overlapping information of the near-concurrent HF-derived surface currents represented by red vectors as well as *in-situ*

wind measurements represented by green vectors. At the San Francisco channel's mouth, there's a vector (red arrow) indicating the tidal cycle and strength as derived from the predicted tidal current from historical measured data, which is not related to CODAR HF antenna measurements, thus appearing with a typically greater size than the surface currents. All times are in coordinated universal time (UTC).

A. EXAMPLE 1 - WIND INTENSITY VS. BACKSCATTER

The SAR image in Figure 25, taken on 05 July 2008 at 1820 UTC, shows the ocean's surface response to a high-wind condition. The surface and near-surface wind measurements (green vectors) indicate 7 to 11 m/s, which leads to an ocean clutter in which most of the features are masked. A True Color map from the same day at 2143 UTC shows the distribution of the cloud cover pattern (Figure 26). The HF radar surface-current vectors (red) and the wind-measurement vectors (green) overlap on the SAR image.

Both images, in Figures 25 and 26, suggest a well-organized, linear oceanically and atmospherically similar pattern in which there's a large fetch with strong winds, as well as information about the wind direction, which is parallel to the aligned dark and bright stripes. In the north part of Monterey Bay, one can see a wind-shadowing effect on the surface roughness illustrated by a darker region representing lower backscatter. In this image the satellite orbit is descending and, since ENVISAT's ASAR always "looks" right, we can see a brighter reflection on the bottom right part of the swath, corresponding to the area closest to the satellite's nadir. In the Point Sur area, there are frontal signatures with slightly less backscatter in the SAR image, which seems to be coincident with flow pattern as perceived by HF-radar surface currents. HF radar also depicts an anti-cyclonic eddy offshore of Point Sur which is masked in the SAR image by wind cluttering, mainly due to the high wind condition.

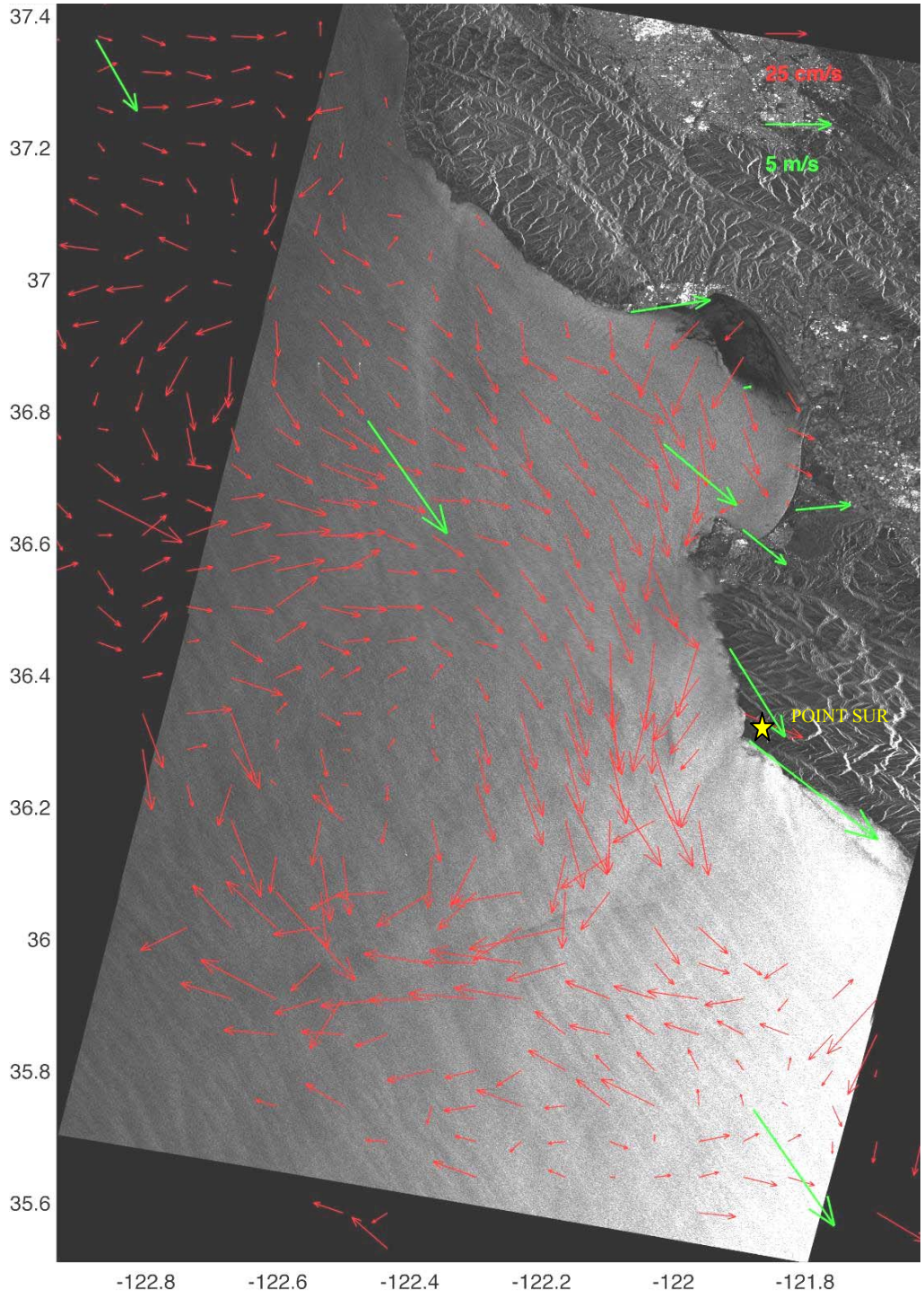

Figure 25. SAR image with HF surface currents (red) and wind vectors (green) on 05 July 2008 at 1820 UTC. The image shows well-organized oceanic pattern in which there's a large fetch with strong winds, as well as wind-shadowing effect on the surface in the north part of Monterey Bay (SAR data provided by ESA).

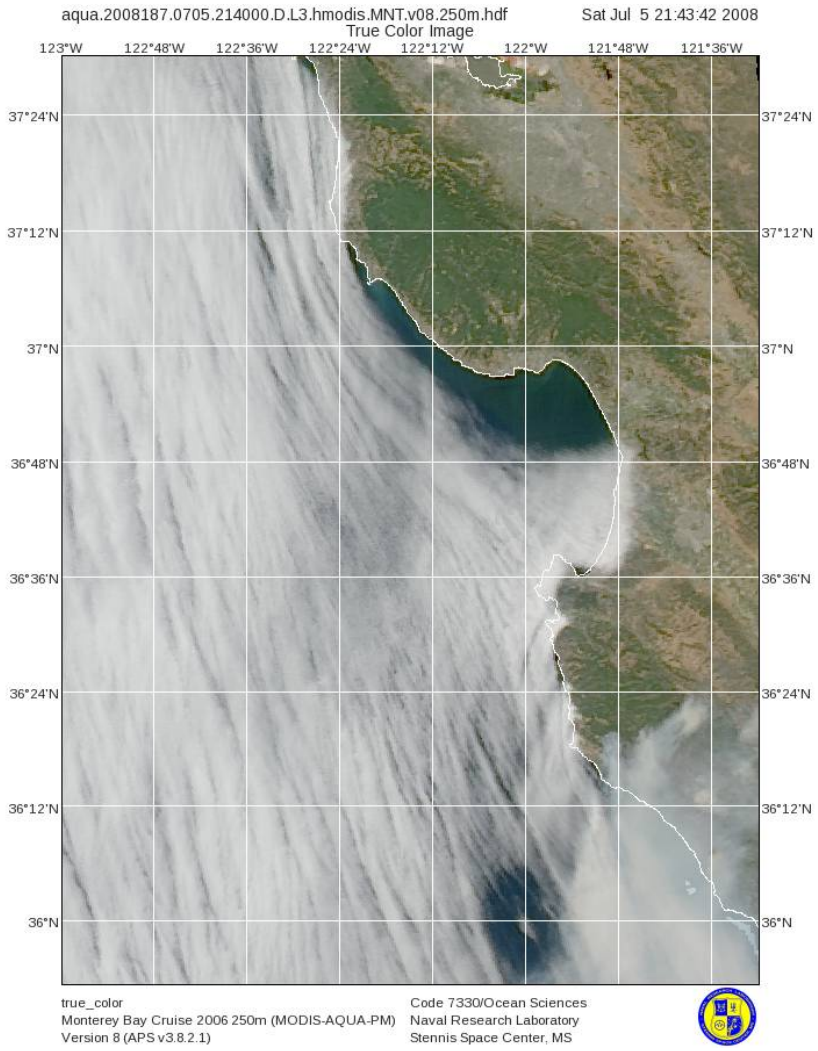

Figure 26. True Color map taken on 05 July 2008 at 2143 UTC showing a well-organized atmospheric pattern agreeable with the ocean surface structure in Figure 25 (after NLR, http://www7240.nrlssc.navy.mil/).

B. EXAMPLE 2 - WIND FRONT

In this example, the SAR image was created on 28 August 2008 at 1823 UTC (Figure 27), the True Color image was obtained later in the same day at 2107 UTC (Figure 28), and the SST map was constructed on 27 August 2008 at 2201 UTC (Figure 29).

A frontal feature is depicted offshore of Pigeon Point, between 36.5N-122.8W and 37.2N-123W by a sharp contrast in backscatter on the SAR image. A cloud cover image in the True Color map taken less than three hours later expresses a similar

structure in the atmosphere, and a previous day SST map shows warmer water close to the coast. This front might be associated with more intense wind stress on the shore side due to atmospheric instability effects caused by warmer water below colder air, thus creating a rougher surface. Note the overall low backscatter due to weak local wind, close to 2 m/s.

The hourly-averaged HF radar surface currents show a general weak northward circulation pattern with meandering eddies and a convergence zone. The wind front detected in the SAR image is not visualized with the HF vectors.

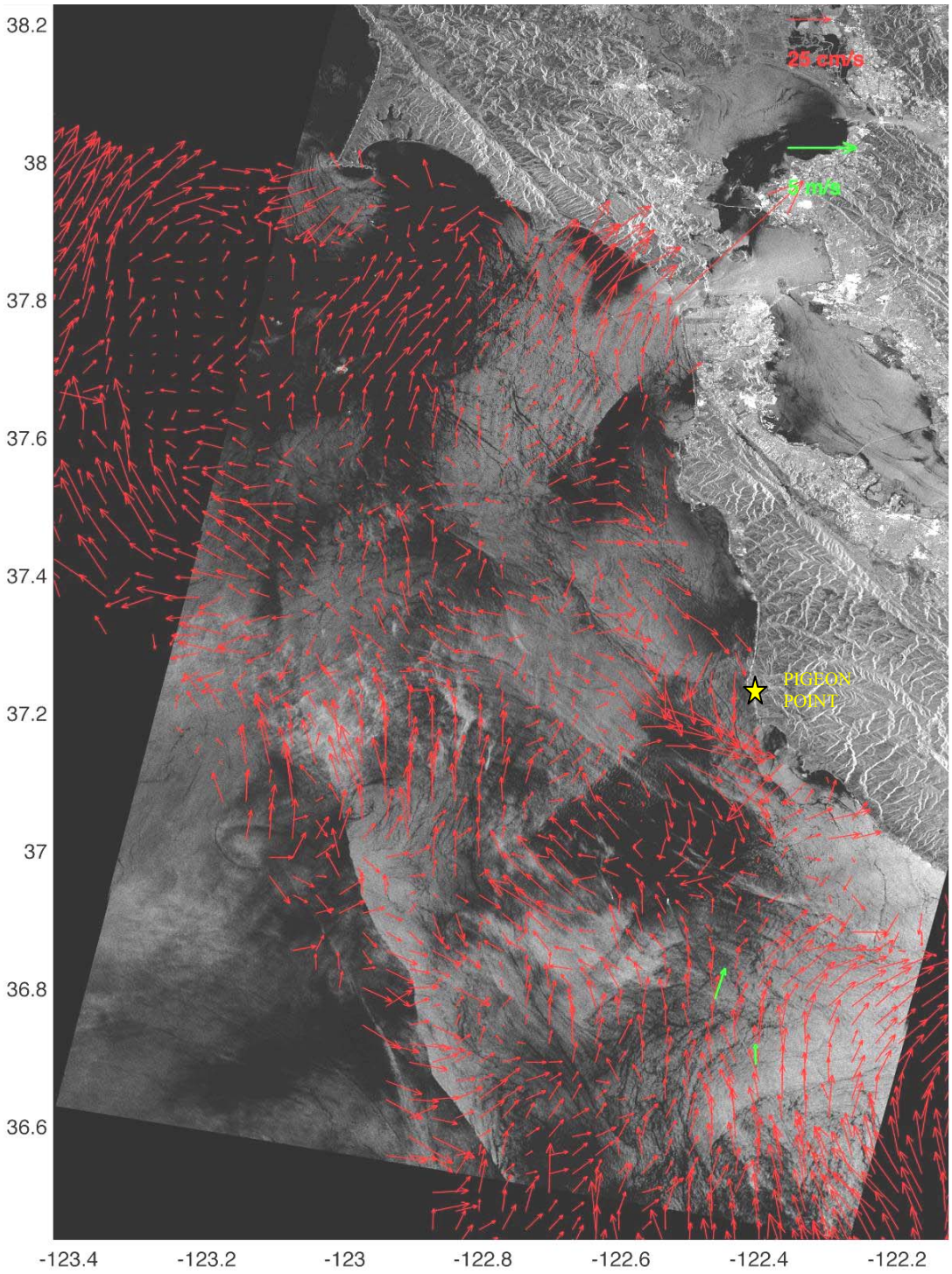

Figure 27. SAR image with HF currents (red) and wind vectors (green) on 28 August 2008 at 1823 UTC. A frontal feature offshore of Pigeon Point (36.5N-122.8W to 37.2N-123W) is depicted by a sharp contrast in backscatter in an overall low-wind condition ~2 m/s (SAR data provided by ESA).

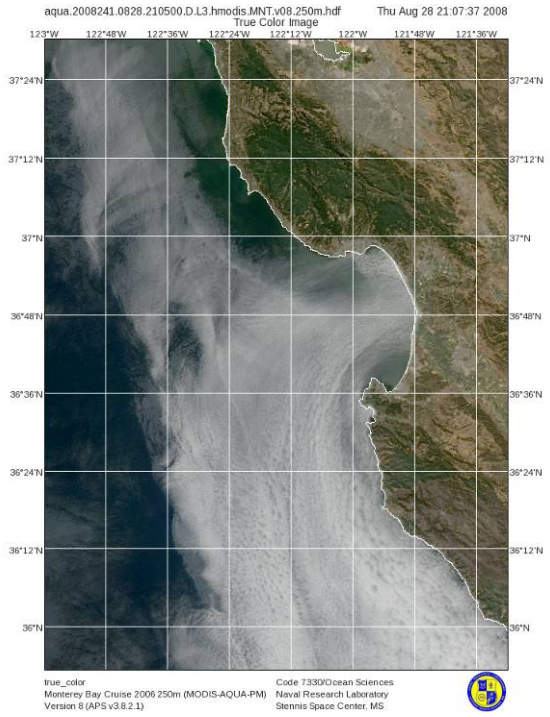

Figure 28. True Color image on 28 August 2008 at 2107UTC (From NLR, http://www7240.nrlssc.navy.mil/).

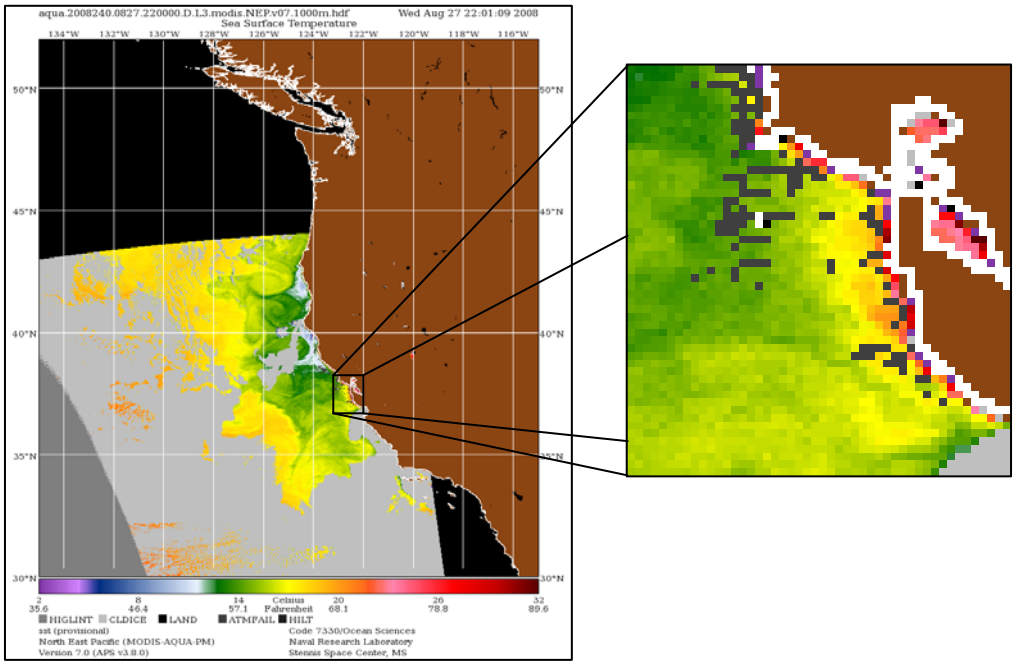

Figure 29. SST map on 27 August 2008 at 2201 UTC showing patches of warmer water close to shore and temperature fronts with an approximately 2° C gradient (After NLR, http://www7240.nrlssc.navy.mil/).

C. EXAMPLE 3 – UPWELLING EVENTS

Several studies (Johannessen et al., 1996; Clemente-Colon and Yan, 1999; Lyzenga, 2004) provide cases of SAR upwelling signatures associated with regions of low backscatter indicated by surfactants, temperature gradients, and atmospheric variability. Figures 30 a), b) and 31 demonstrate upwelling events near the coast on 6 September 2008 at 2100 UTC for SST and Chlorophyll images and 7 September 2008 at 0555 UTC for SAR. The SST shows colder water (greenish) extending from Half Moon Bay to Point Sur and over the Monterey Bay Canyon. The SAR image agrees with this assessment by exhibiting darker surface patches on the same locations. The upwelling of biogenic oils that dampen the SAR Bragg waves, thus decreasing backscatter, is depicted by the Chlorophyll Concentration image, where higher levels of chlorophyll are shown along the coast margins. The average seaward flow direction depicted by HF radar (Figure 31) is consistent with horizontal divergence at the surface.

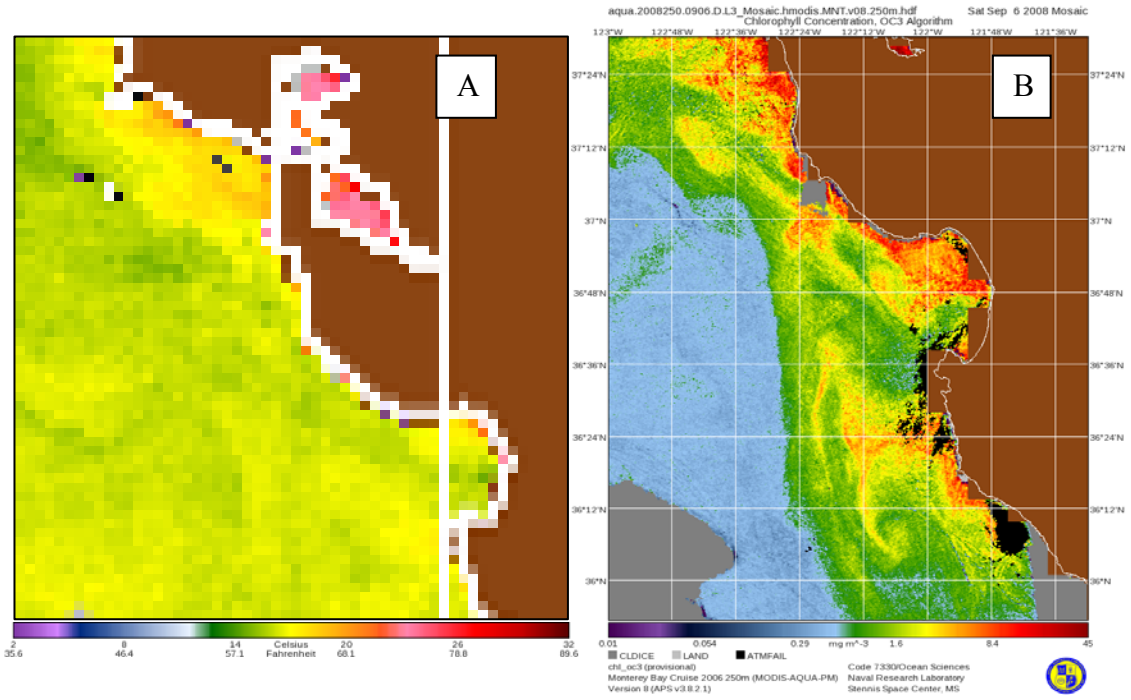

Figure 30. Upwelling event illustrated on both a) SST and b) Chlorophyll Concentration MODIS products on 6 September 2008 at 2100 UTC. In a) the colder water (greenish) extends from Half Moon Bay to Monterey Bay Canyon. In b) the image shows higher levels of productivity near the coast, corroborating the upwelling occurrence (After NLR, http://www7240.nrlssc.navy.mil/).

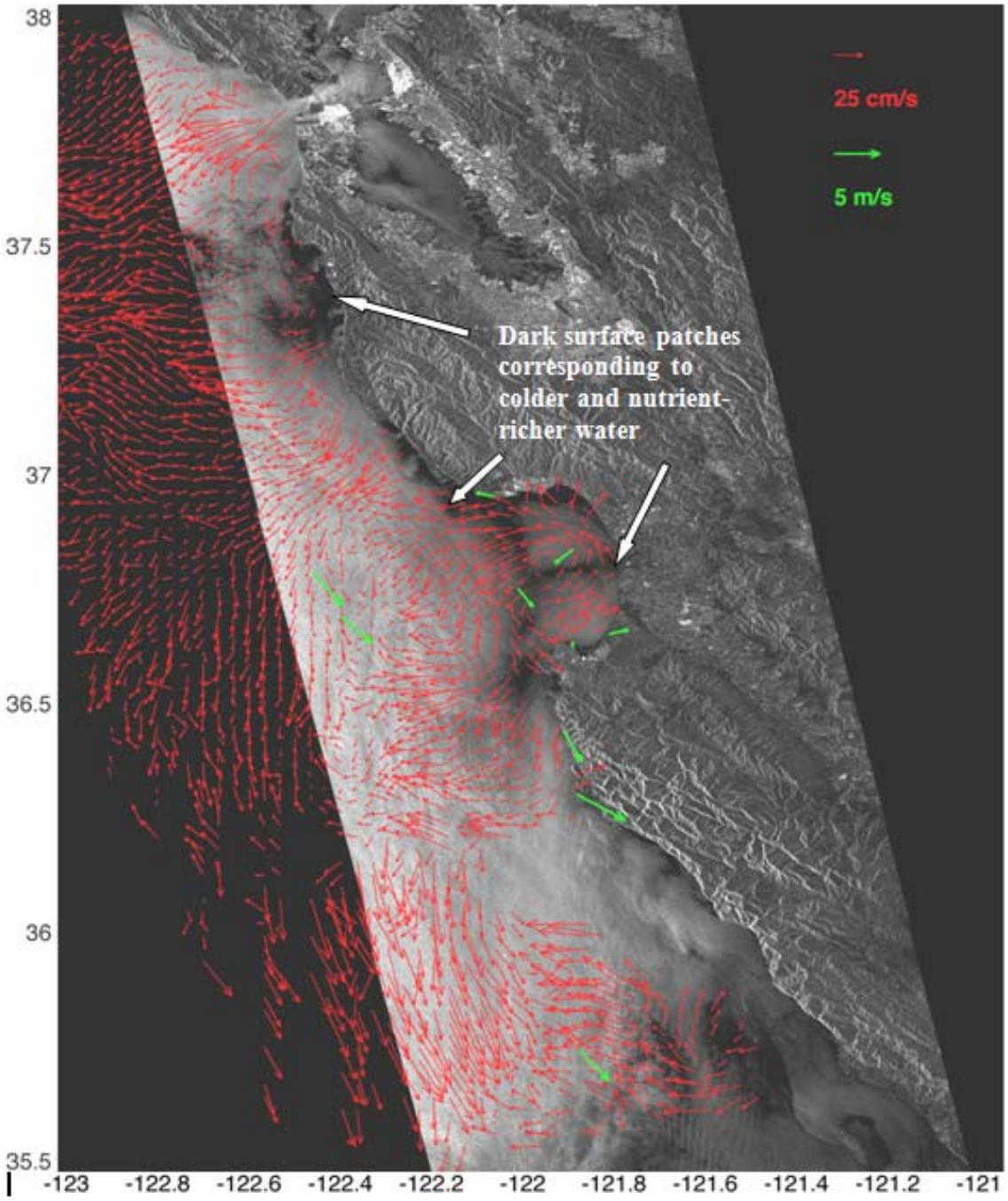

Figure 31. Upwelling event seen in SAR image on 7 September 08 at 0555 UTC. The darker patches show evidence of colder and biologically richer water from Half Moon Bay to Point Sur and over Monterey Bay Canyon. HF radar surface-current flow is seaward (SAR data provided by ESA).

Some of the imaging mechanisms contributing to the SAR surface roughness are surface wind, which is moderate and ranges from 2.5 to 5 m/s, in this case, damping by

surfactants, and atmospheric instability effects. The changes in stability in the atmospheric boundary layer induce more or less wind stress at the surface depending whether the ocean is warmer or colder than the atmosphere. As a result, warmer water is viewed as brighter image, whereas colder water as darker image.

Another example of upwelled-colder and nutrient-richer water in the San Francisco, Half Moon Bay and Pigeon Point areas is demonstrated in SAR and SST images. The SAR image in Figure 32 was formed on 7 October 2010 at 1823 UTC and the SST product 2.5 hours later (Figure 33). The lower SAR backscatter regions are consistent with the lower temperature areas in the SST image. The previous wind directions and intensities are plotted in Figure 34 for six days before the imaged event, showing favorable winds for north hemisphere eastern boundary upwelling.

Since the wind speed is lower than 2.7 m/s at the time of image processing, the presence of surfactant slicks and vortical features are depicted by this imaging mechanism. Another mechanism present is surface-wind stress caused by an atmospheric instability effect on the marine boundary layer, where brighter areas seen in SAR correspond to warmer water and darker patches adjoining coast to colder water in SST data.

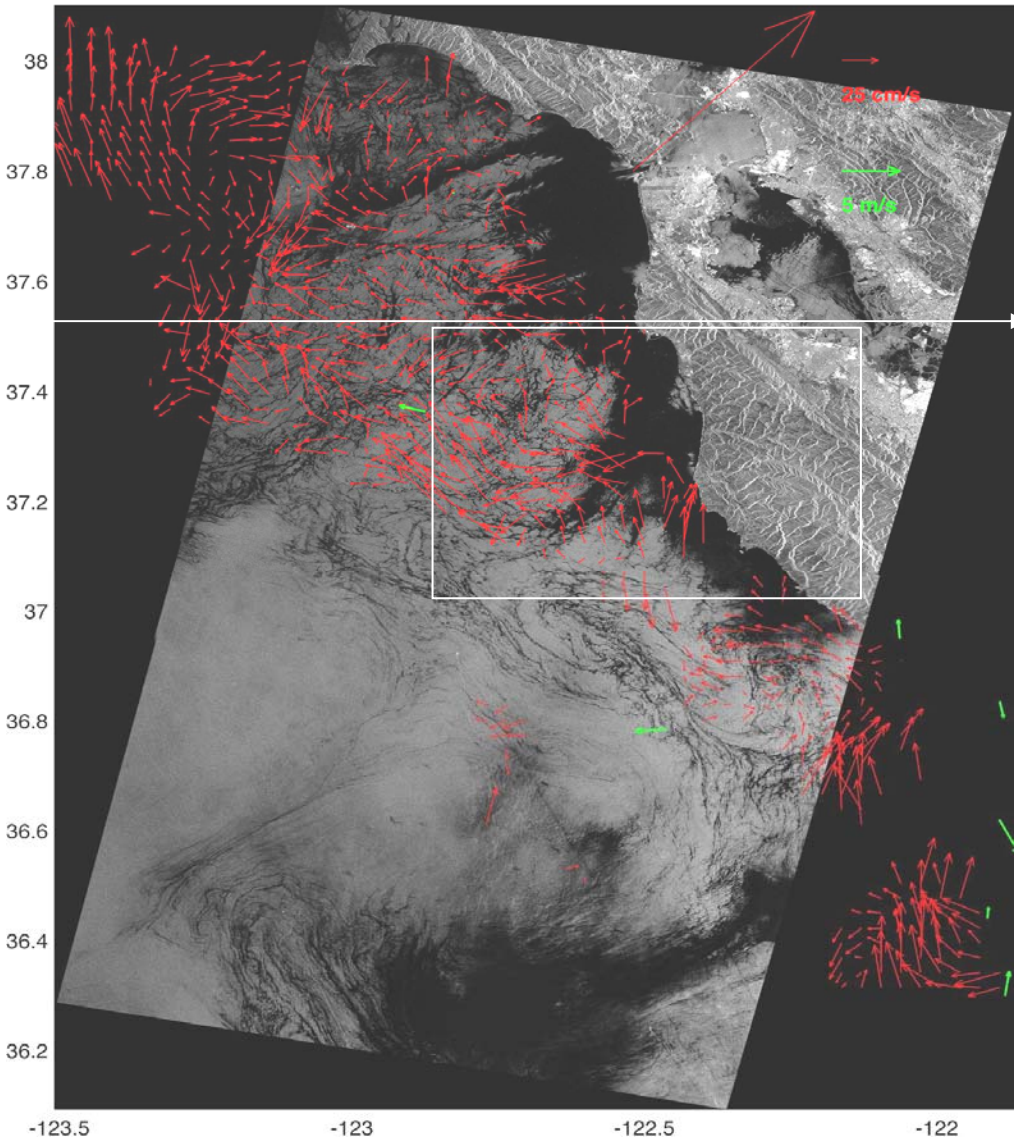

Figure 32. Upwelling event seen in SAR image on 7 October 2010 at 1823 UTC. The darker patches show upwelled-colder and nutrient-richer water along the west coast from San Francisco to Pigeon Point. Note the presence of surfactants associated with natural oils. The horizontal white line indicates the SST map northern latitude in Figure 33. The white box indicates the daily-average HF-radar surface currents seen in Figure 35 (SAR data provided by ESA).

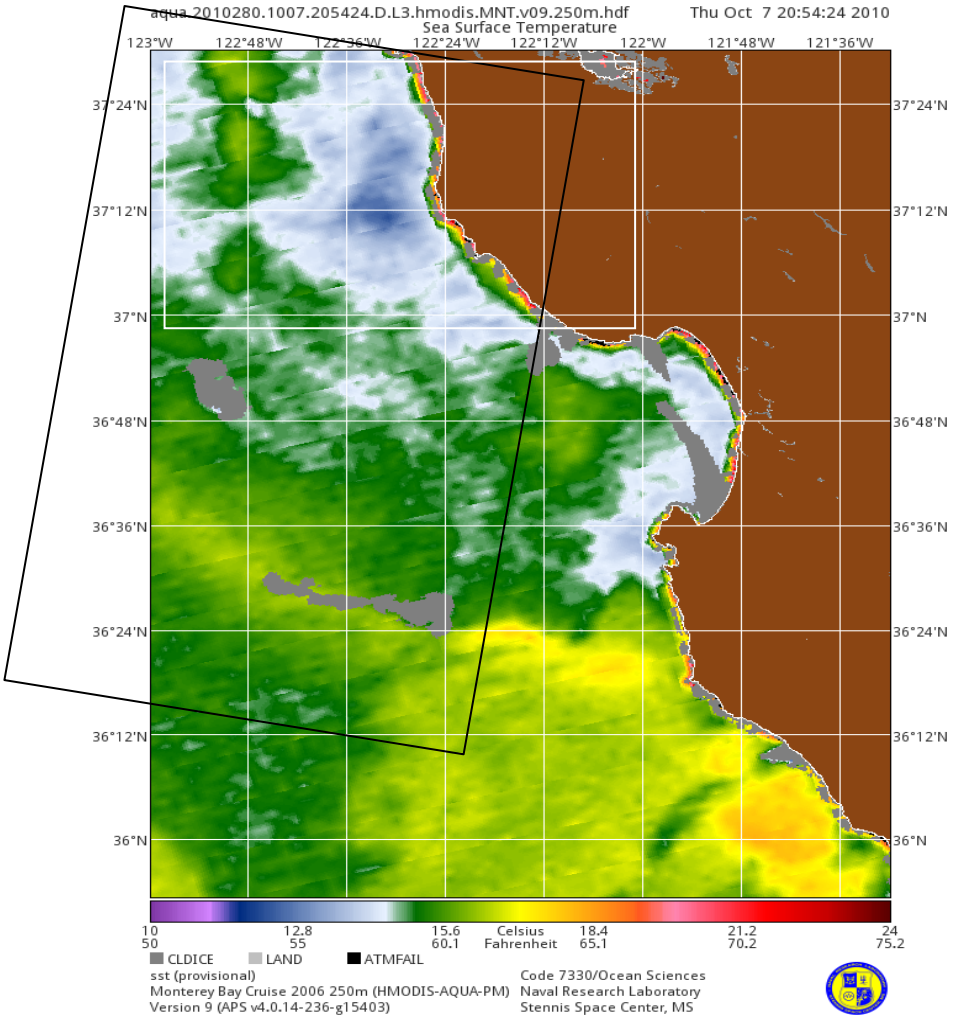

Figure 33. MODIS SST map from 7 October 2010 at 2054 UTC showing patches of colder water near the coast from Half Moon Bay to the Pigeon Point area. The black box indicates the SAR image seen in Figure 32, and the white box indicates the daily-average HF-radar surface currents seen in Figure 35. (After NLR, http://www7240.nrlssc.navy.mil/).

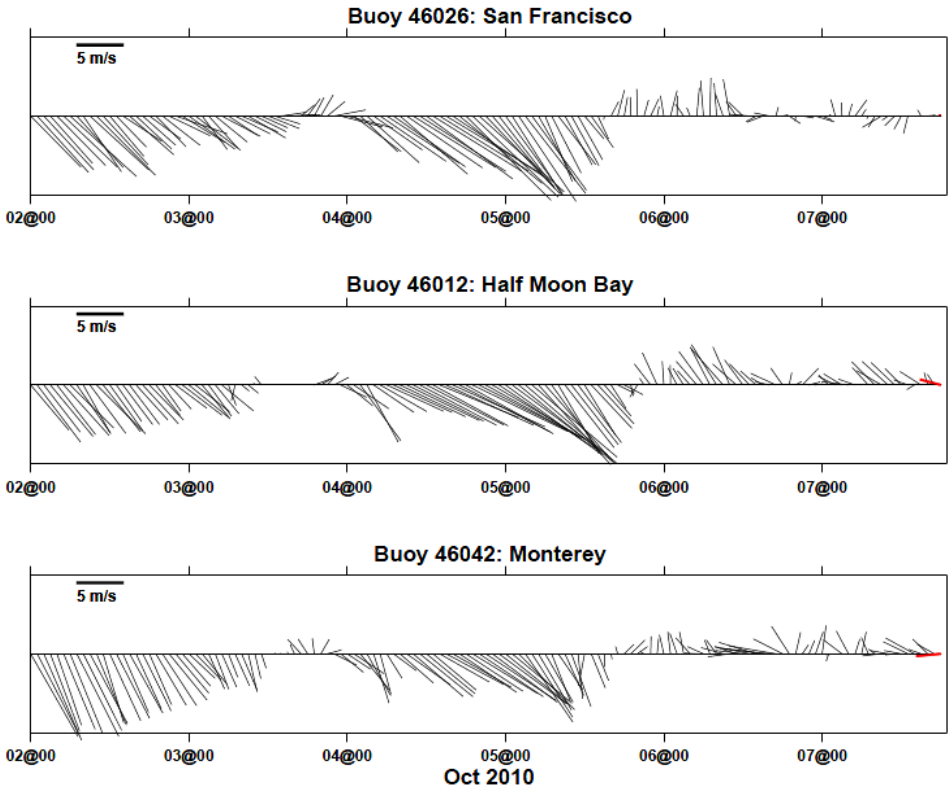

Figure 34. Three buoy wind plots for the six days preceding the SAR-image formation show upwelling favorable winds. The red segment indicates wind condition at the SAR image time.

The HF radar surface currents, overlapped on the SAR image in Figure 32, display an indication of the hourly average circulation pattern in the region. Though the information provided by HF radar is, in this case, inconclusive in terms of ocean feature visualization, one can complement the assessment of the ocean-surface dynamics by understanding the current circulation. Figure 35 shows a Central California Currents (CencalCurrents) HF radar derived product consisting of a daily-averaged (25 hour) surface currents where the tidal cycle is naturally removed and, therefore, biases caused by tides and the diurnal sea breeze are purged. This product is found in the Cencalcurrents portal or through the link http://cencalcurrents.org/PlotsRealTime/AverageTotals/. The surface currents seen in the daily-averaged HF product better expresses the circulation seen in the SAR image, namely a seaward filament depicted offshore of Pigeon Point as well as a general northward surface flow pattern.

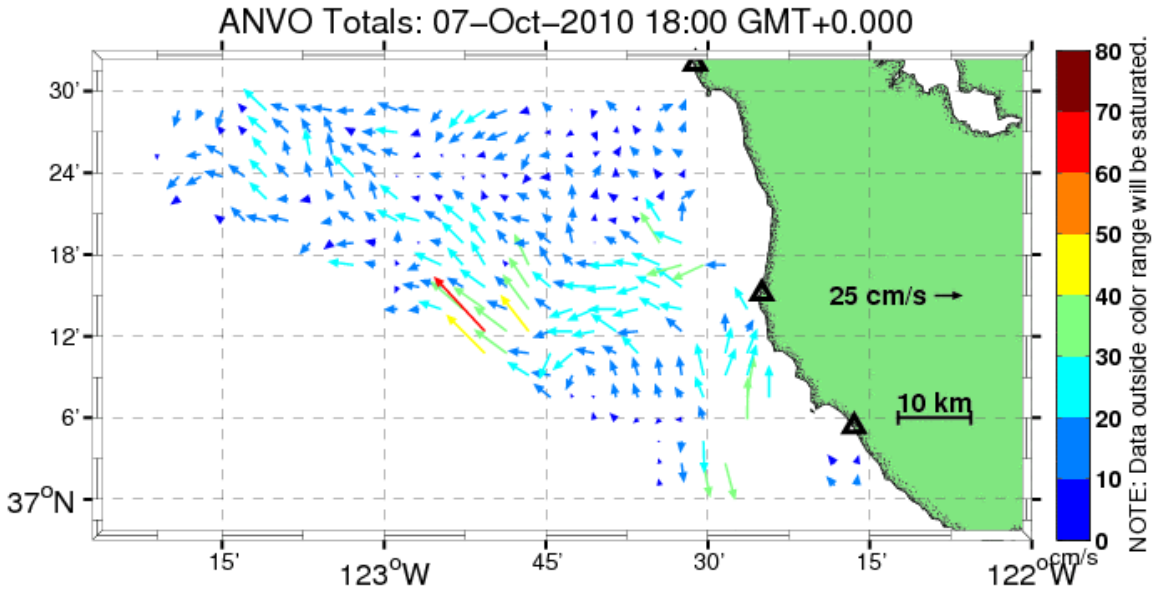

Figure 35. Daily-averaged HF-radar surface currents for the Half Moon Bay area corresponding to the white box on the SAR image (Figure 32). The tide is naturally removed. (From Cencalcurrents, http://cencalcurrents.org).

D. EXAMPLE 4 – CHANNEL OUTWARD FLOW AND INTERNAL WAVES

The features seen in the SAR image captured on 1 March 2009 at 0555 UTC are outward flow from the San Francisco channel and tidal packets of internal waves in the Half Moon Bay and Pigeon Point regions. The bathymetry contours are overlapped with the SAR image for analysis purposes. At the time, the tidal current is 2.5 hours into flood (Figure 36), and the wind is 6.5 m/s from SSE, shown as green vectors in the SAR image.

Lyzenga et al. (2004) point out that "fresher water runs seaward on successive ebb tidal cycles" creating a SAR visible feature like the one shown in Figure 37. The width of the San Francisco channel widens from 1.8km near the Golden Gate Bridge to 4.5 km at the bay's mouth. After exiting the bay's mouth, the 10km-radius plume has a dispersion shape that resembles the shelf's bottom topography. The outgoing flow edge has relatively higher backscatter than the surrounding pixels, which might be a consequence of sea surface temperature and salinity gradients, as well as constructive interference in the convergent front due to the "shock wave" between the outflowing tidal current and the new inward flood cycle. The converging front's signature imaging mechanism is then partially related to tidal hydrodynamic modulation of Bragg waves, wind stress, an

apparent contribution of seafloor steepness, likely temperature and some impact from dielectric constants of fresher and saltier water masses. This feature is recurring in the actual data set when the appropriate conditions are met, of which the most relevant condition is the completion of the ebb cycle, provided there's enough wind at the surface level.

The second feature, also recurring in this area, is packets of internal waves travelling parallel to the sea floor topography and dispersing in a near-bathymetric form off the coast of Half Moon Bay and Pigeon Point. The internal waves' structure induces turbulence at the surface, on the scale of Bragg waves, which is seen as consecutive bright and dark bands of backscatter with crests and troughs aligned parallel to the direction of propagation. The brighter bands are associated with convergence at the crests, and the darker with divergence at the troughs (Apel, 2004; Martin, 2004)

Coincidently, in the lower part of the image, we can see atmospheric gravity waves aligned parallel to the coast with approximately 2.5km wavelength. For better visualization of this feature, the reader is referred to Figure 73 in Appendix A.

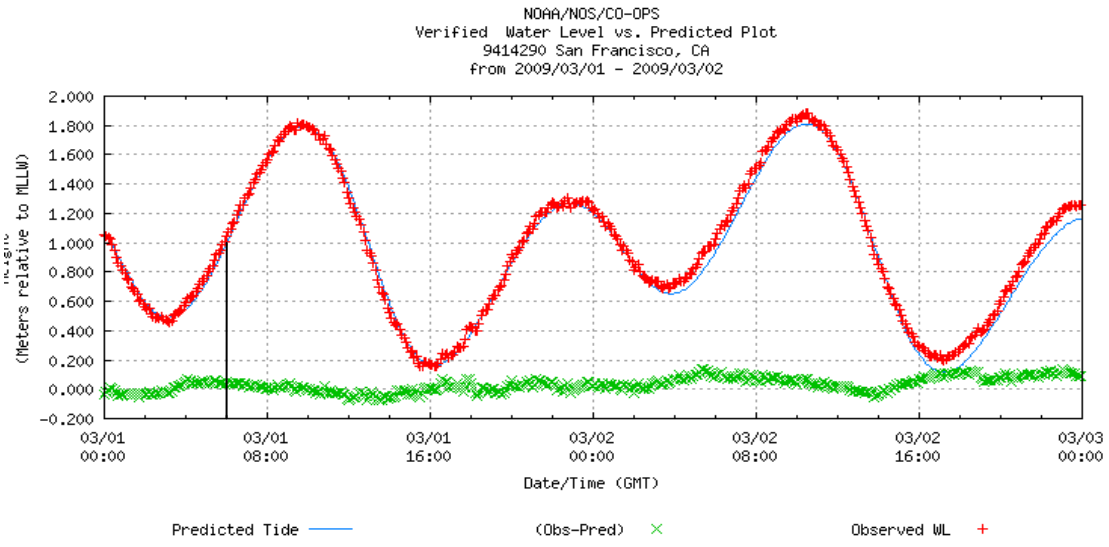

Figure 36. Observed tide in San Francisco on 1 March 2009. The vertical line corresponds to the SAR image time. (After NOAA, http://tidesandcurrents.noaa.gov/)

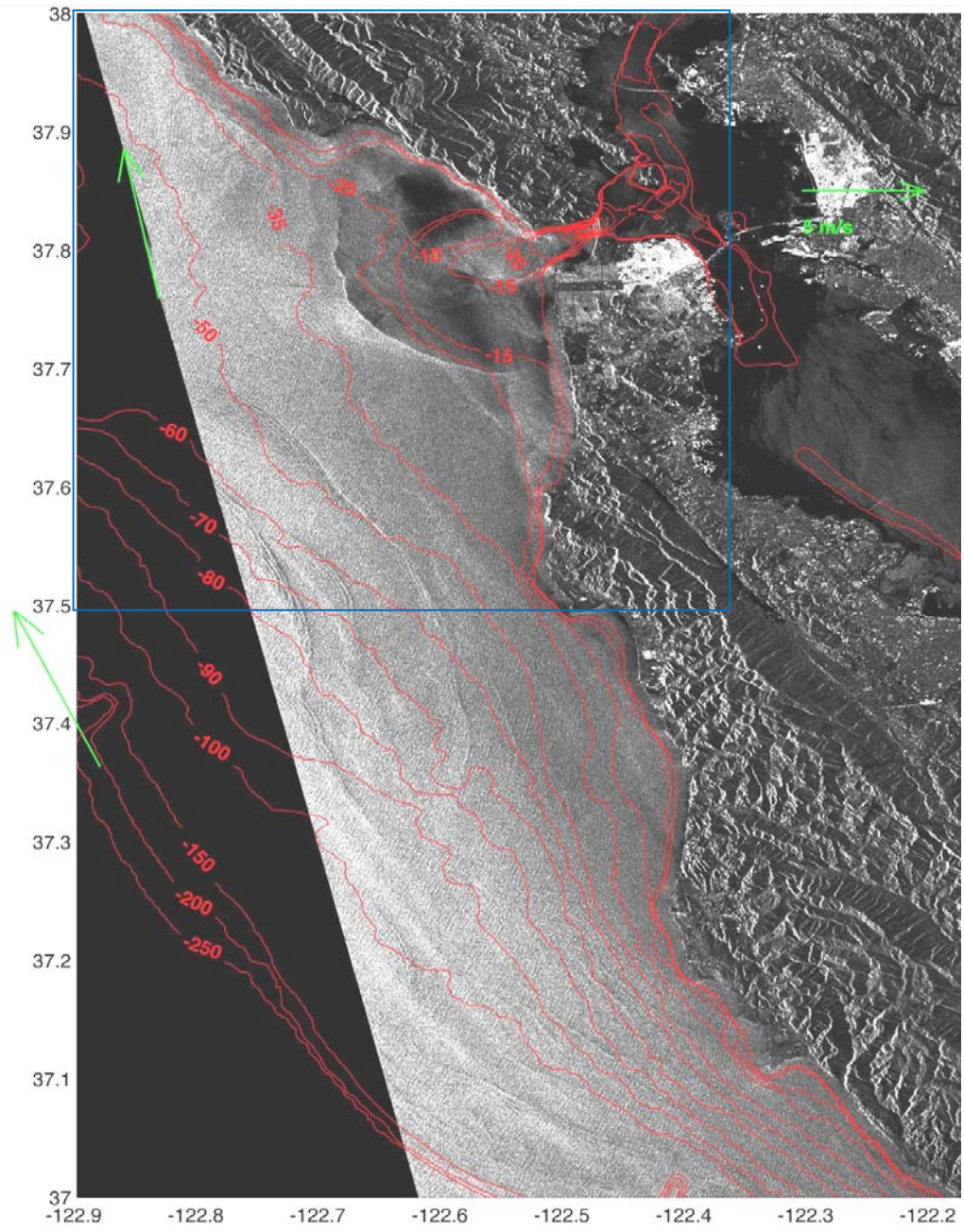

Figure 37. The SAR image is from 1 March 2009 at 0555 UTC and exhibits two recurring local features. In the San Francisco area, there's an outward flow which is imaged upon completion of the ebb tidal cycle and, farther south,internal waves are seen propagating shoreward. The bathymetry contours are overlapped. The blue box delimits the area of Figure 38 (SAR data provided by ESA).

A 24h HF radar surface-current trajectory product is plotted in Figure 38 for the San Francisco area. The understanding of the surface current field during the hours

preceding the formation of the SAR image facilitates the interpretation of the local dynamics. An animated plot of the 24h particle trajectories can be found at the CencalCurrents website (http://cencalcurrents.org/PlotsRealTime/Trajectories/).

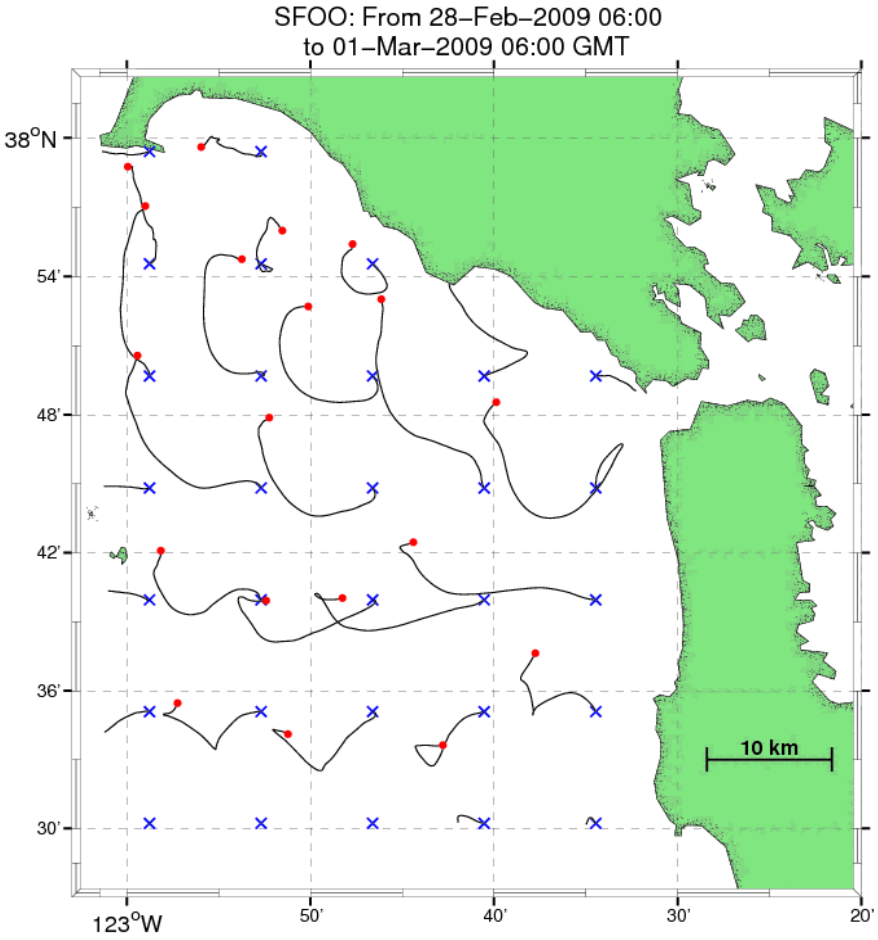

Figure 38. HF radar, 24h surface current trajectories for the San Francisco area, equivalent to the blue box in Figure 36. The blue x represents the starting time on 28-Feb-2009 at 0600 UTC, and the red dot the ending time on 01-Mar-2009 at 0600 UTC (From Cencalcurrents, http://cencalcurrents.org).

E. EXAMPLE 5 – HF-RADAR SURFACE CURRENTS AND SAR IMAGE ASSESSMENT

The following image product is an example of SAR backscatter and HF-radar surface-current contribution to the interpretation of coastal ocean dynamics. An atmospheric feature is also depicted in Monterey Bay. The SAR image created on 14

August 2010 at 1820 UTC is shown in Figure 39 along with the overlapped HF-radar surface-current vectors and wind measurements. The wind speed is low (3 m/s), yet the presence of surfactants provides guidance in the SAR image assessment.

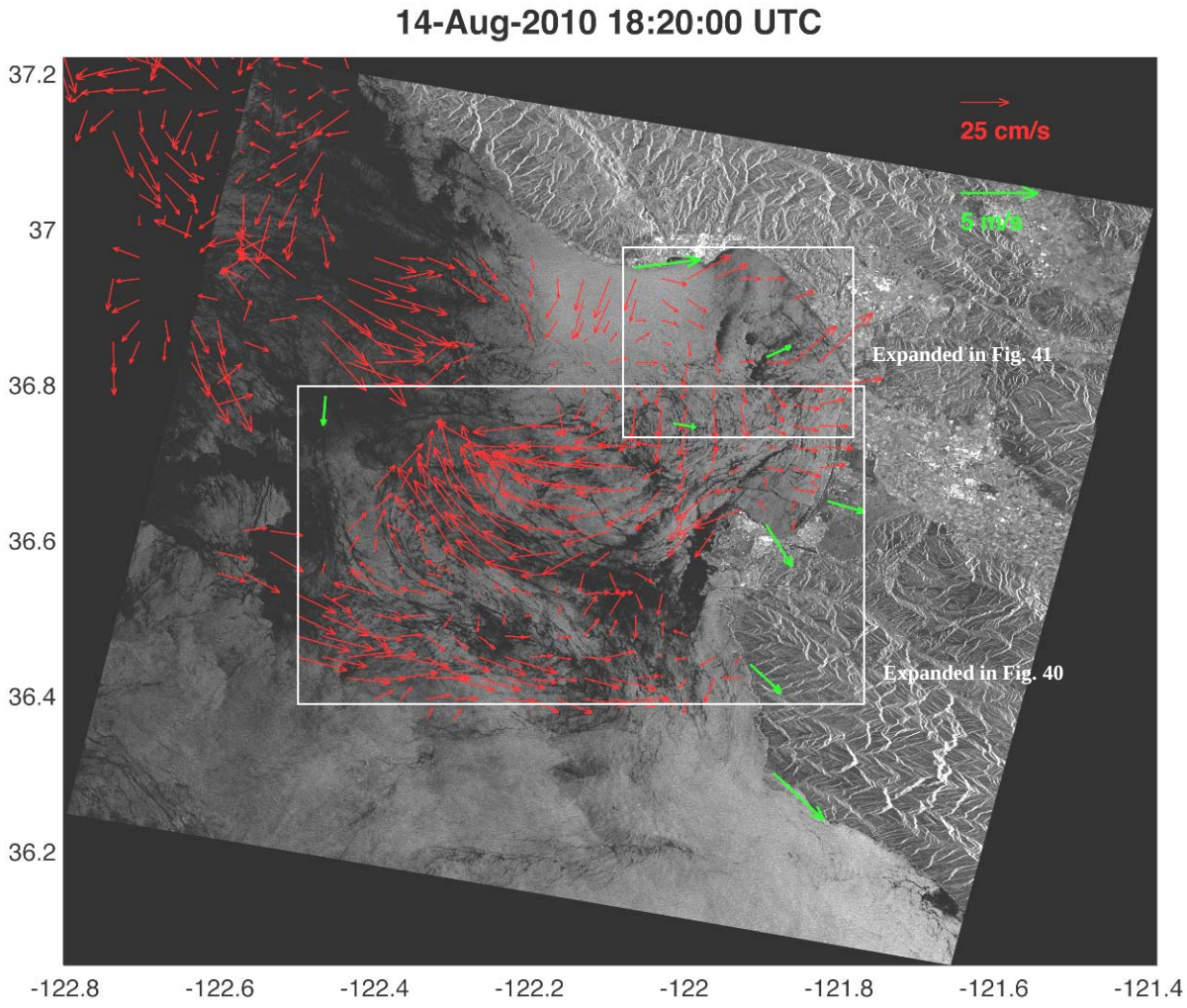

Figure 39. SAR image of Monterey Bay sensed on 14 August 2010 at 1820 UTC. Both SAR and HF-radar products contribute to the interpretation of coastal ocean dynamics. Several slick patterns are seen in the SAR image, and its interpretation is facilitated by the surface current (SAR data provided by ESA).

North of Point Pinos, there's an anti-cyclonic feature seen in SAR through surfactants, where the hourly-average surface current complements the interpretation of the circulation pattern. The mentioned feature leads to a curving set of slick stripes seen in SAR that appear to be flowing to the west and generally coincide with the HF pattern.

The plume is assessed in HF radar vectors, as well. In the lower part of the image, there's an inward flow that is clearly depicted from HF radar surface currents when overlaid on the SAR image (Figure 40). Through this example we recognize that the HF-radar surface current field helps to identify flow structures in the SAR image.

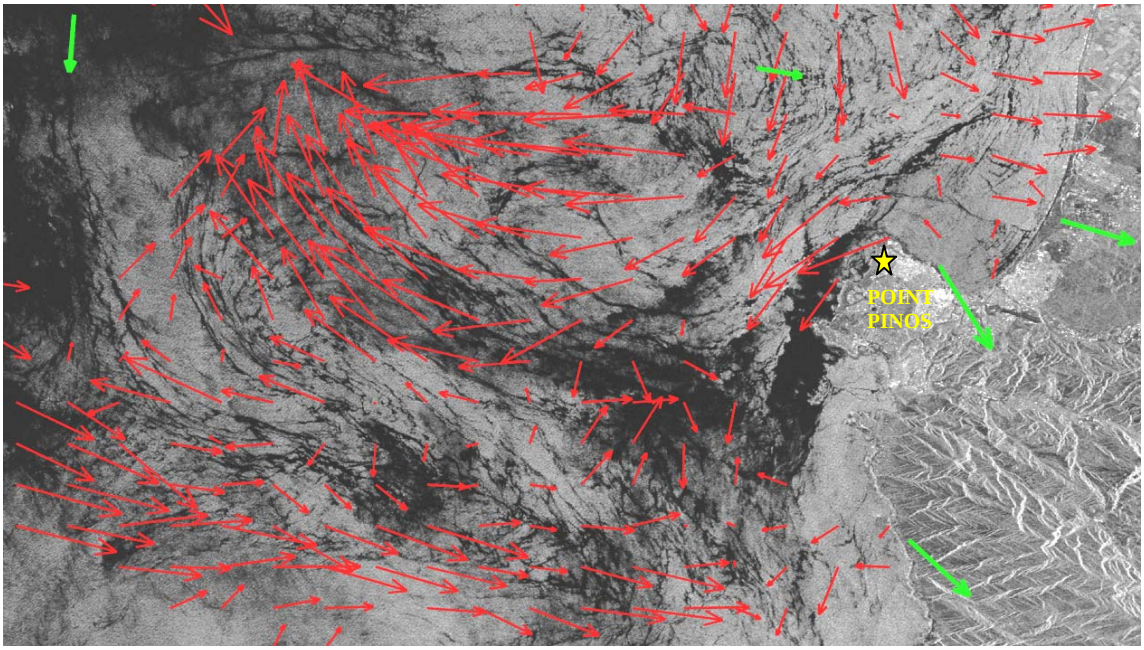

Figure 40. SAR meandering slick stripes assessed in HF-radar vectors, as well. The red arrows show current vectors, and the green arrows represent wind measurements (SAR data provided by ESA).

Above Elkhorn Slough in Monterey Bay, SAR depicts a feature resembling a rain or pressure cell as described in Alpers and Melsheimer (2004). The rain core is shown as a dark circular feature with ~ 1.2km diameter, in which the Bragg waves are dampening by the downdraft (Figure 41). Alpers and Melsheimer (2004) review how the downdraft spreading over the surface, around the core, creates roughness at the surface which in turn intensifies the backscatter. Around this feature there's no HF radar information which may or may not be related with the rain cell. MODIS Terra True Color product for 14 August 2010 at 1815 UTC shows evidence of cloud cover in Monterey Bay (http://lance-modis.eosdis.nasa.gov/imagery/subsets/?subset=AERONET_Monterey; not shown here).

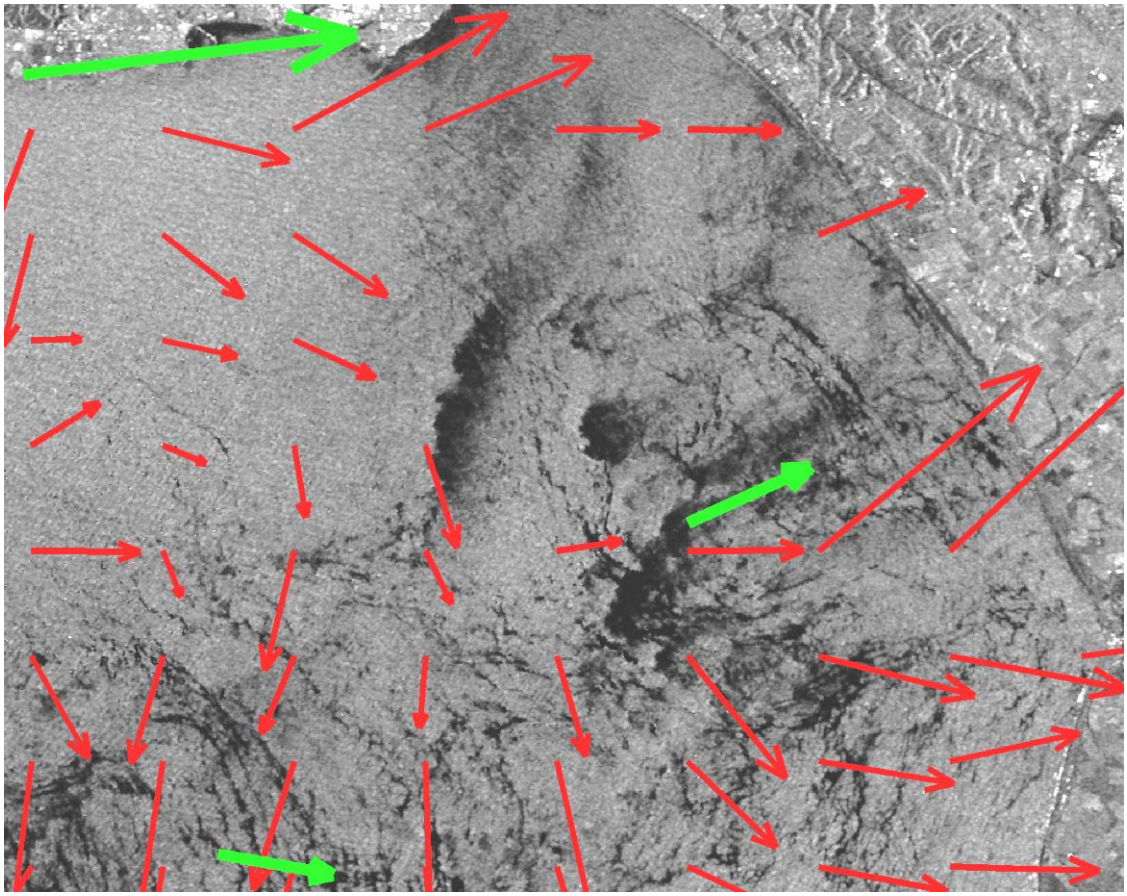

Figure 41. Detailed image of a rain or pressure cell depicted in Monterey Bay sensed on 14 August 2010 at 1820 UTC. (SAR data provided by ESA).

The correspondent 24h HF-radar surface-currents trajectory plot for the Monterey Bay area is shown in Figure 42. The perception of surface current motion ahead of the SAR imaging assists evaluation of local dynamics. An animated plot of the 24h particle trajectories can be found at the CencalCurrents website (http://cencalcurrents.org/PlotsRealTime/Trajectories/).

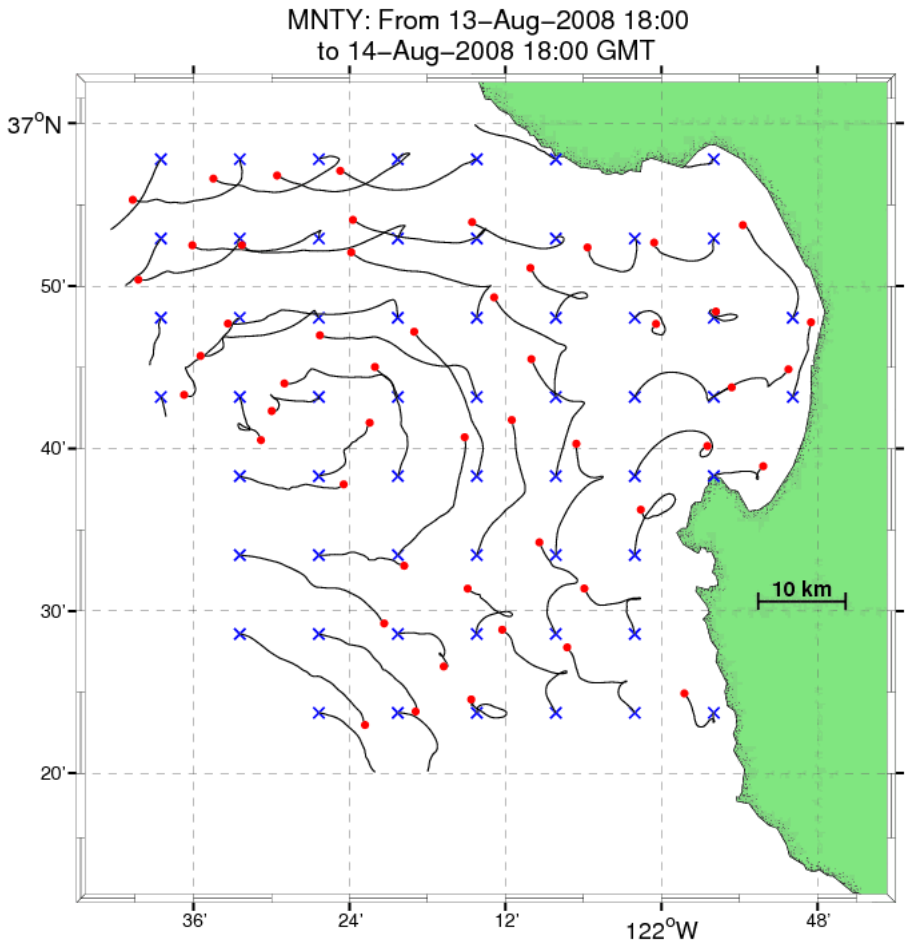

Figure 42. HF-radar, 24h surface current trajectories for the Monterey Bay area. The blue x represents the starting time on 13-Aug-2010 at 1800 UTC, and the red dot the ending time on 14-Augr-2010 at 1800 UTC (From Cencalcurrents, http://cencalcurrents.org).

Given the relatively slow ocean response to tides and surface winds, the SAR image reveals a moment that contains both contemporaneous atmospheric patterns as well as past-occurring patterns. Hourly HF-radar surface currents might not be sufficient to fully comprehend surface current expression in SAR imagery, and vice-versa. Figure 43 illustrates an HF-radar product consisting of daily-averaged (25 hour) surface currents where the tidal cycle is naturally removed and, therefore, biases caused by tides and the diurnal sea breeze are purged. This product is found in the Cencalcurrents portal or through the link http://cencalcurrents.org/PlotsRealTime/AverageTotals/. This example

demonstrates that the comparison of the SAR image with the different HF products reveals a closer match between the daily-averaged HF pattern with the SAR pattern.

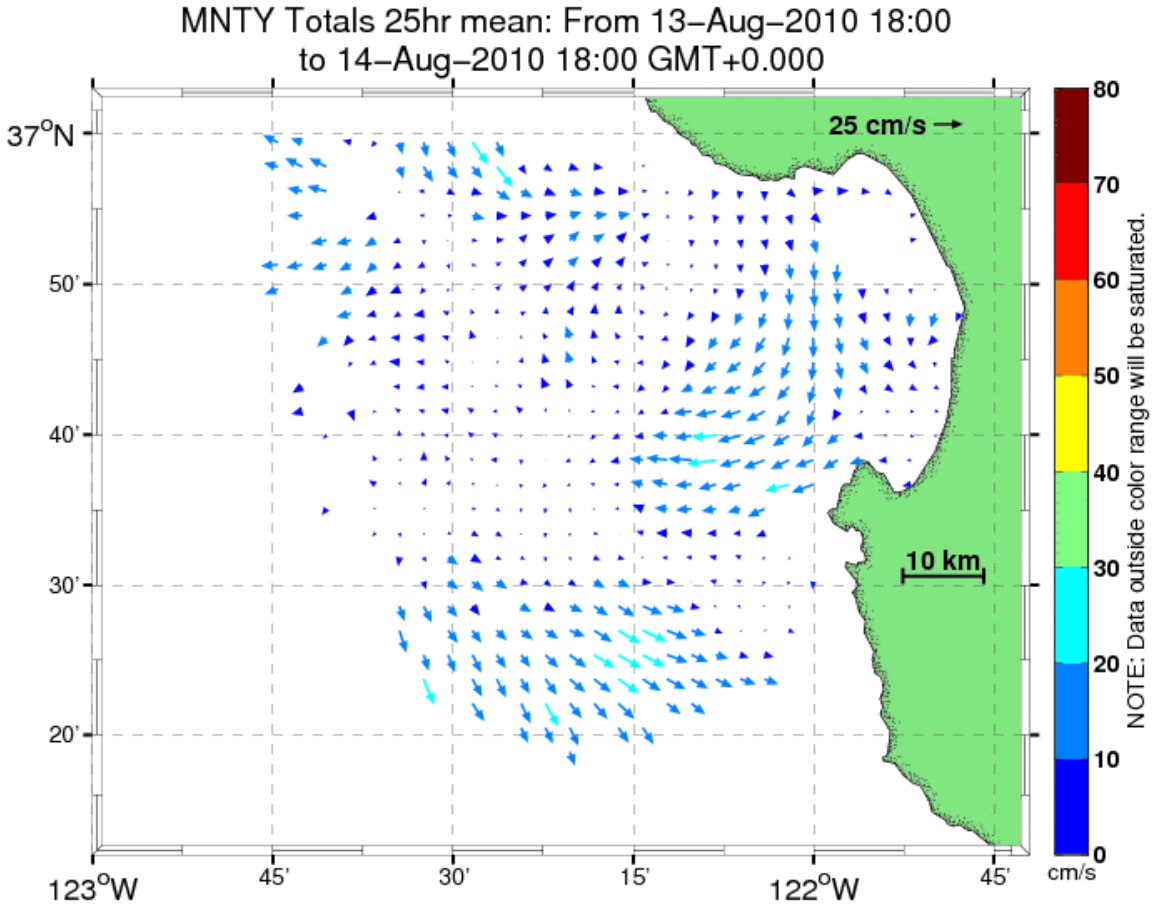

Figure 43. Daily-averaged HF-radar surface currents for the Monterey Bay area, ending time on 14-Aug-2010 at 1800. The tide is naturally removed. (From Cencalcurrents, http://cencalcurrents.org).

F. EXAMPLE 6 – DIVERGENCE TEST

The divergence test is performed in the entire data set, where positive or negative horizontal divergence is computed and plotted along with the HF current vectors. Despite the fact that several results don't clearly indicate a correlation between SAR features and HF surface currents, one example where there's a correlation is shown in Figures 44 and 45. The SAR image taken on 02 September 2010 at 1823 UTC (Figure 44) and the correspondent divergence test for HF surface currents exhibit a convergence front centered at 37N 122.5W, mapped by blue dots in the divergence image (Figure 45). The

current flow has a north-south alignment, which agrees with the orientation of the surfactant accumulation close to the frontal structure depicted in the SAR image. The divergence results that are close to zero are not plotted for visualization enhancement purposes.

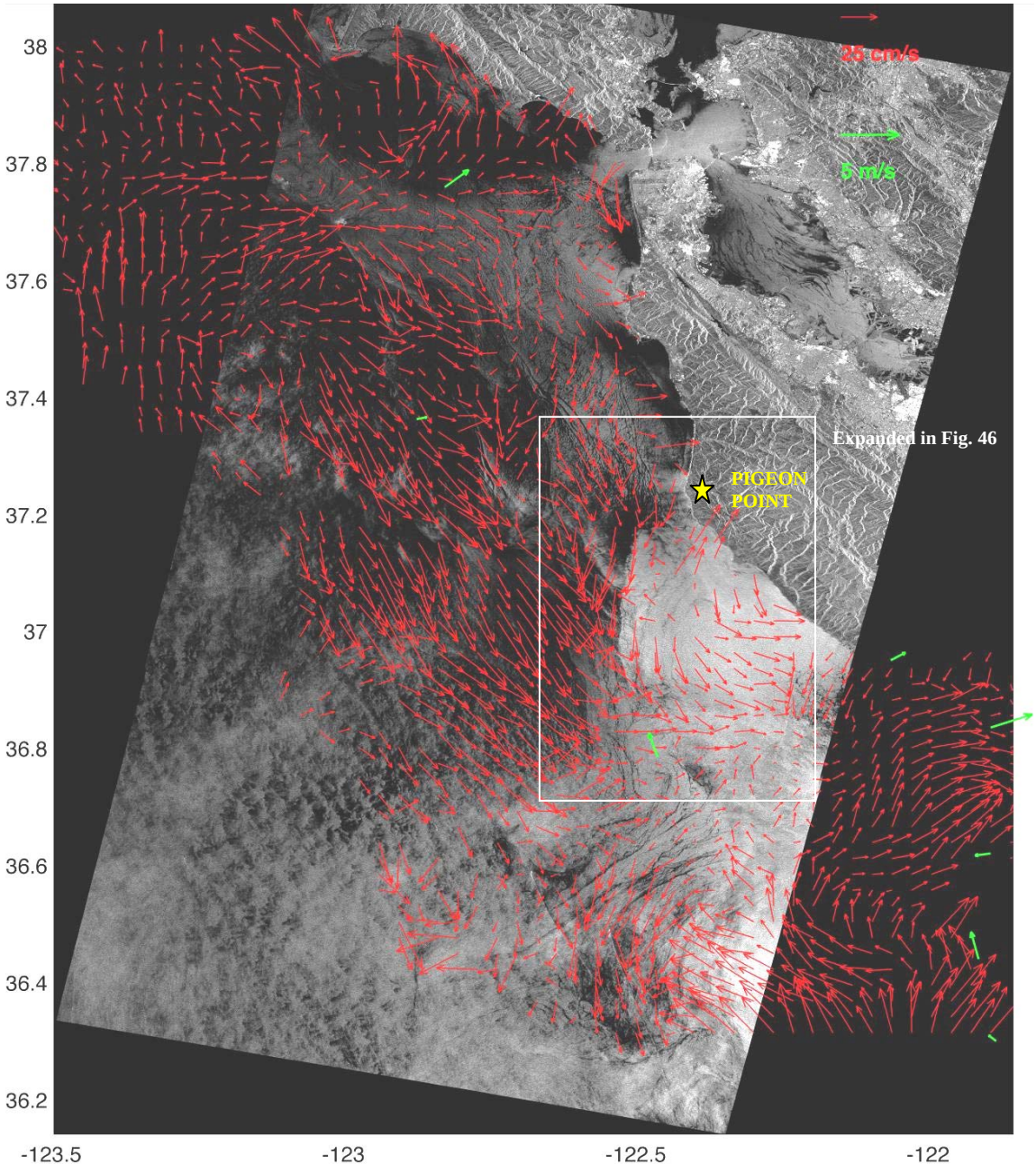

Figure 44. SAR image sensed on 02 September 2010 at 1823 UTC in which a frontal signature aligned north-south is depicted close to Pigeon Point. The white box corresponds to an enlarged area in Figure 46 (SAR data provided by ESA).

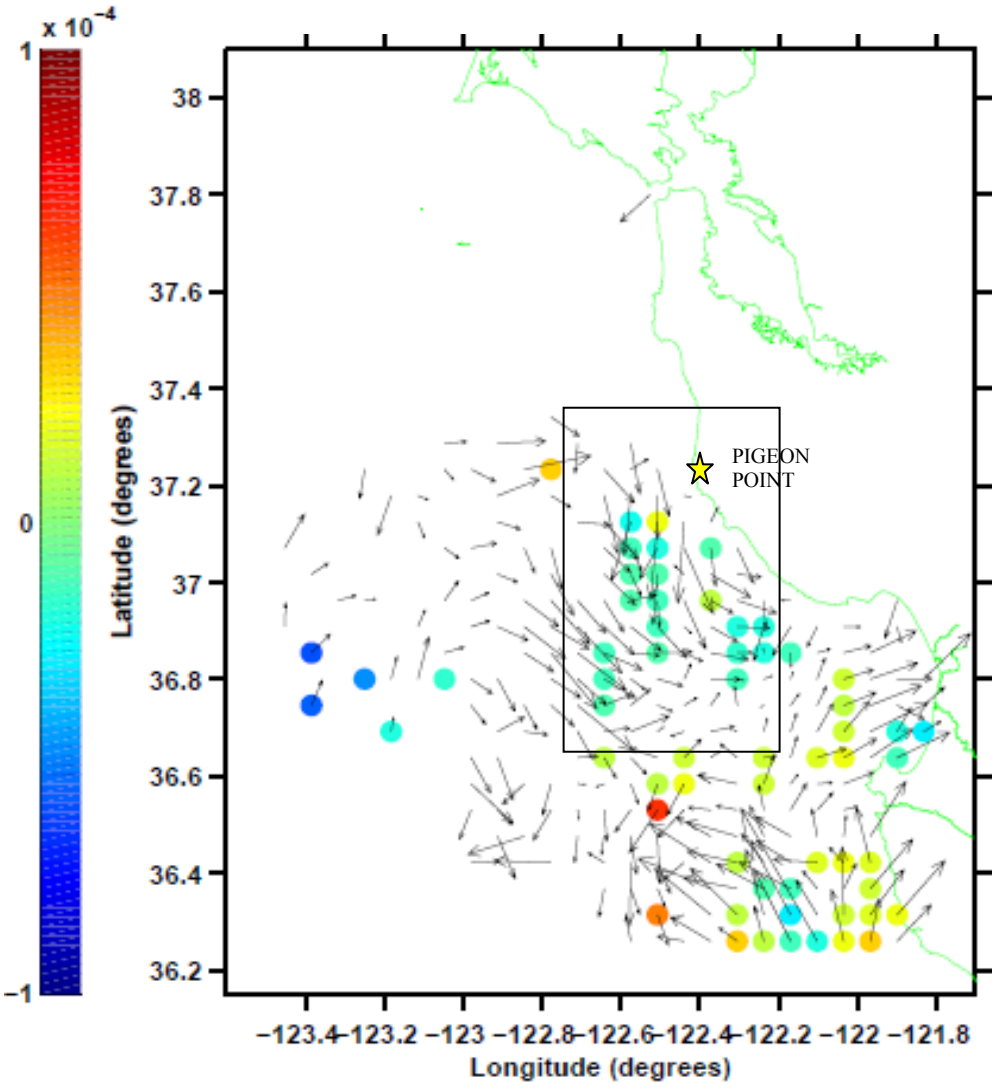

Figure 45. Divergence test shows a convergence (bluish dots) front centered at 37N 122.5W, where the flow has a north-south alignment. This agrees with the orientation of the surfactants close to the frontal structure depicted in the SAR image in Figure 44 and in the enlarged area in Figure 46.

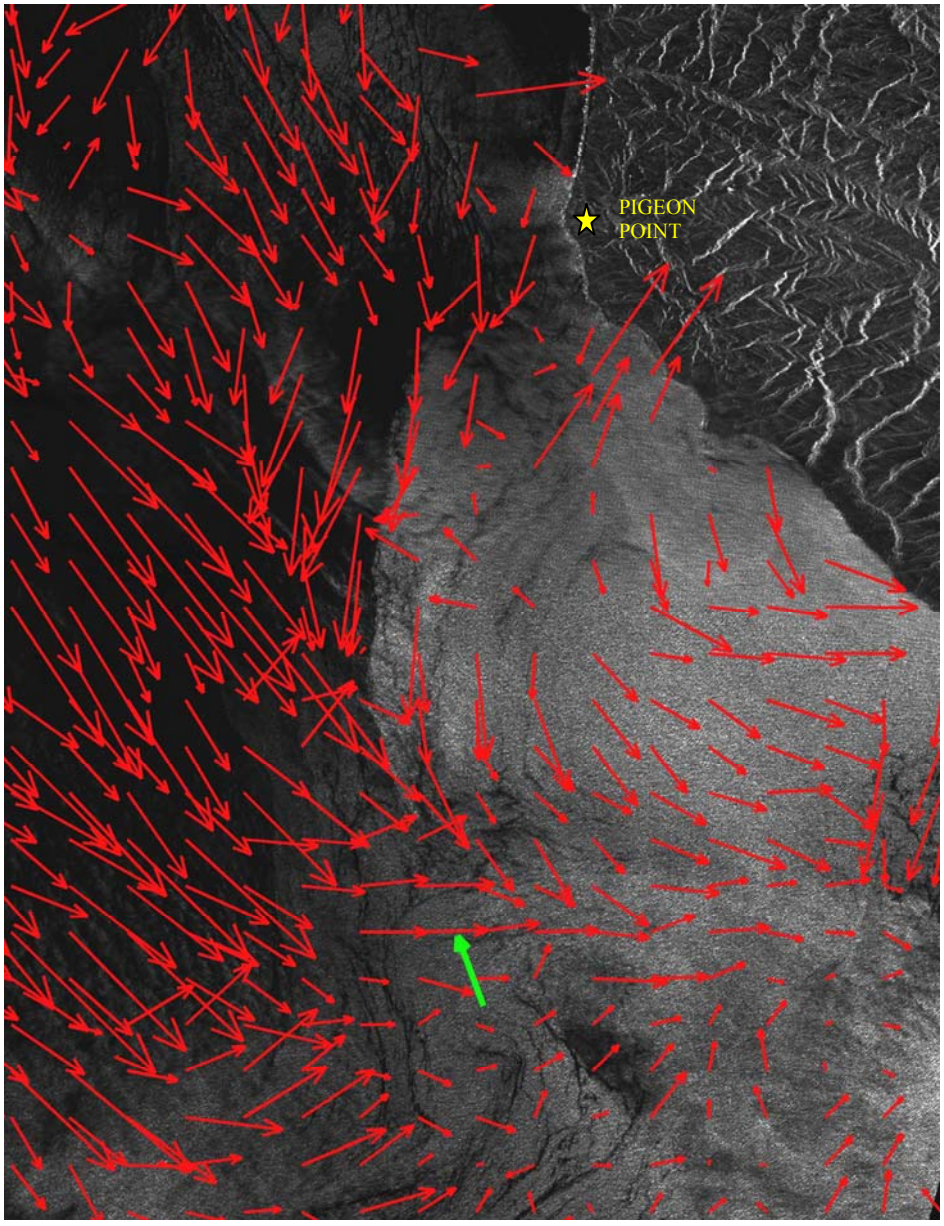

Figure 46. Detail image of a convergence zone depicted by SAR and by the horizontal divergence test in Figure 45. The flow has a north-south alignment (SAR data provided by ESA).

As pointed out earlier, there's often more than one imaging mechanism present in the formation of a SAR ocean image (Holt, 2004). Surface winds on the order of 2-10 m/s and surface currents on the order of 20-50 cm/s transfer energy to the wave field and interact with SAR Bragg waves at different scales. Induced roughness by surface currents tends to be 10 to 20 times less prominent than roughness caused by surface wind.

In this example, a wind speed below 3 m/s contributes little to the surface roughness, allowing the detection of features by other mechanisms. In the SAR image, the boundary between the bright and the dark regions that can be associated with warm and cold water masses is identified as a convergence (negative divergence) zone in the HF-radar surface current map (Figure 46). In Figure 47, the visible part of an SST map for 02 September 2010 at 2200h, 4 hours after the SAR image, illustrates the type of coastal temperature gradients surrounding the convergence zone but, unfortunately, cloud cover masks the exact location being discussed. The example described shows that in cases with relatively low wind condition, it might be possible to visualize the HF-scale surface current contribution to the features seen by SAR.

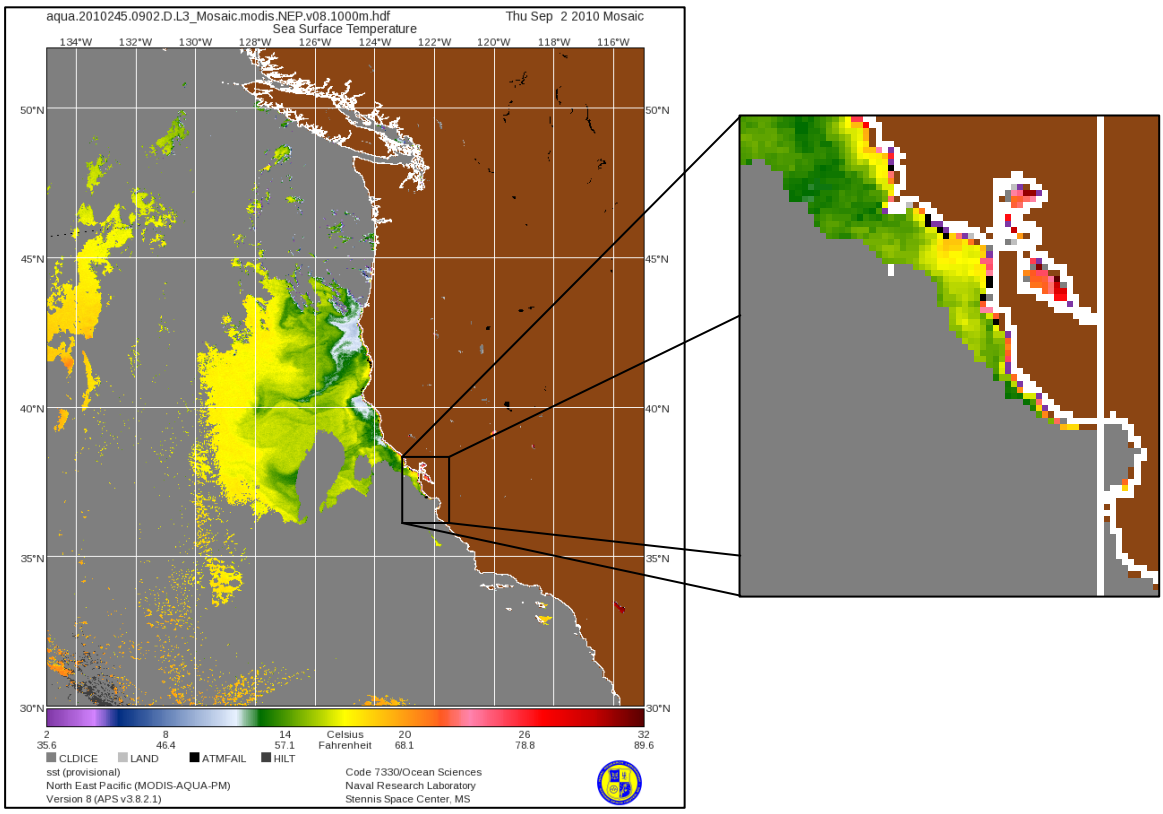

Figure 47. SST map with 1km resolution for 02 September 2010 at 2200 UTC, 4 hours after the SAR image, illustrating the type of coastal temperature gradients surrounding the convergence zone. The area being discussed is masked by cloud cover (After NLR, http://www7240.nrlssc.navy.mil/).

G. EXAMPLE 7 – SAR FEATURES SEEN IN HF-RADAR SURFACE CURRENT

The SAR image in Figure 48 provides examples of oceanic surface features within the HF-radar large scales. The image was sensed on 25 May 2008 at 0555 UTC. The local wind is weak (~ 3m/s) and from the southeast.

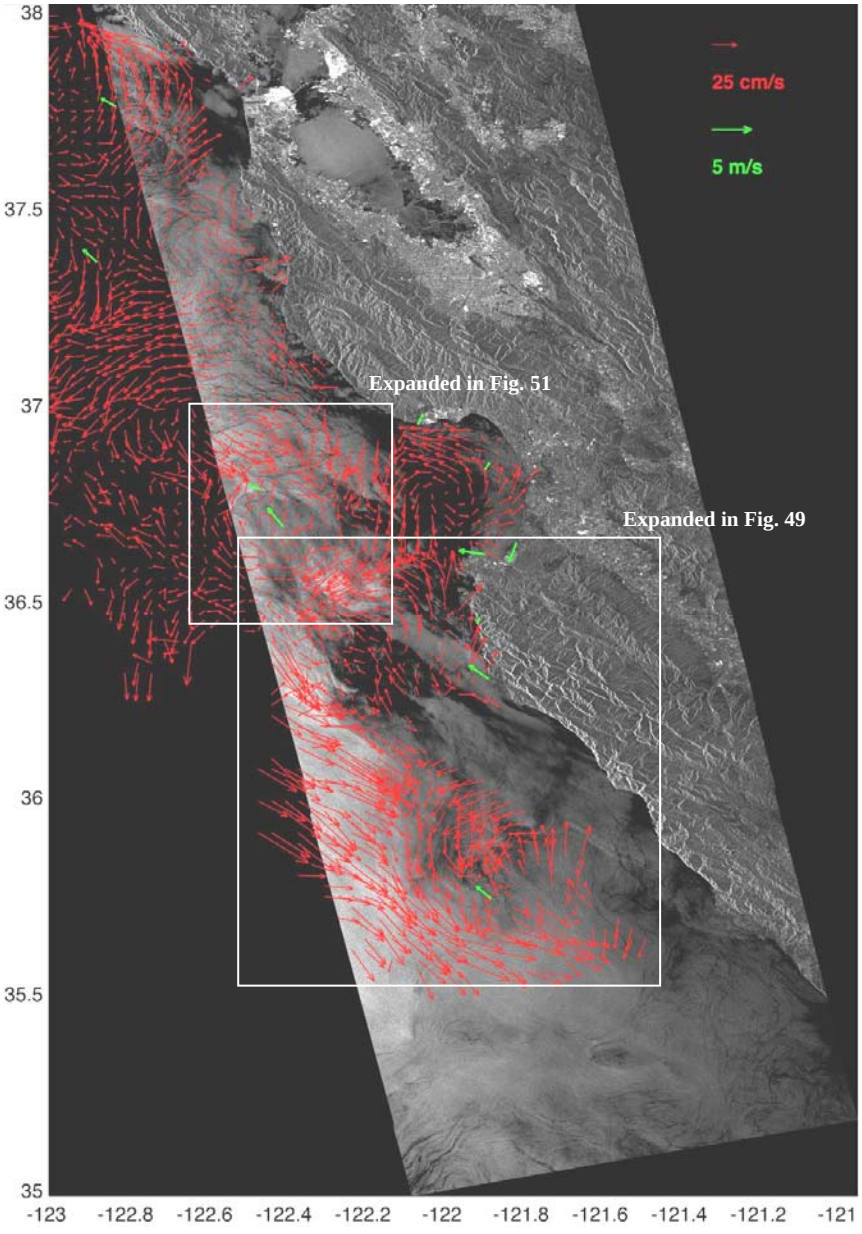

Figure 48. SAR image sensed on 25 May 2008 at 0555 UTC where both SAR- and HF-radar products detect a frontal signature offshore of Point Sur (details in Figure 49) and an anti-cyclonic eddy offshore of Monterey (details in Figure 50). The average wind is ~ 3m/s (SAR data provided by ESA).

Offshore of Point Sur, Figure 49 shows a frontal signature seen in SAR with a brighter edge where one of the mechanisms at work is convergence. The visible flow field sensed by the HF-radar indicates the presence of a strong southeastward surface current that turns south and then east, in total agreement with the plume edge. The water mass closer to shore evidences the presence of biogenic slicks which might indicate recent upwelled water.

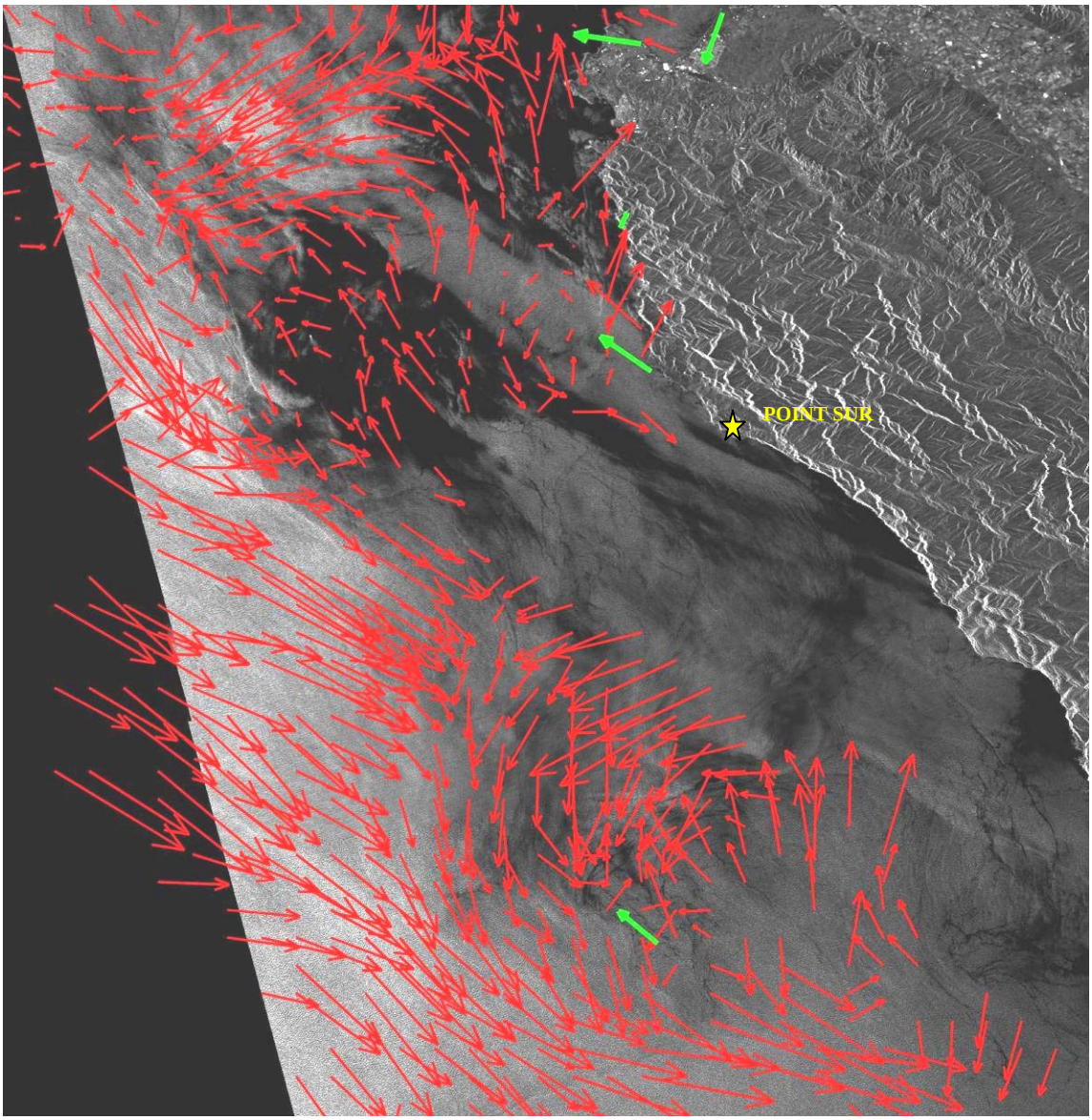

Figure 49. Detail of the SAR image sensed on 25 May 2008 at 0555 UTC where a frontal signature offshore of Point Sur is depicted by both SAR- and HF-radar products (SAR data provided by ESA).

Given that, we propose that HF radar and SAR are capable of measuring the same ocean phenomenon under low wind conditions and strong surface currents, providing the features are large enough. The divergence map in Figure 50 illustrates converging HF-radar currents (inside the circle) in the Point Sur area, which is coincident with the brighter frontal signature seen in the SAR image in Figure 49.

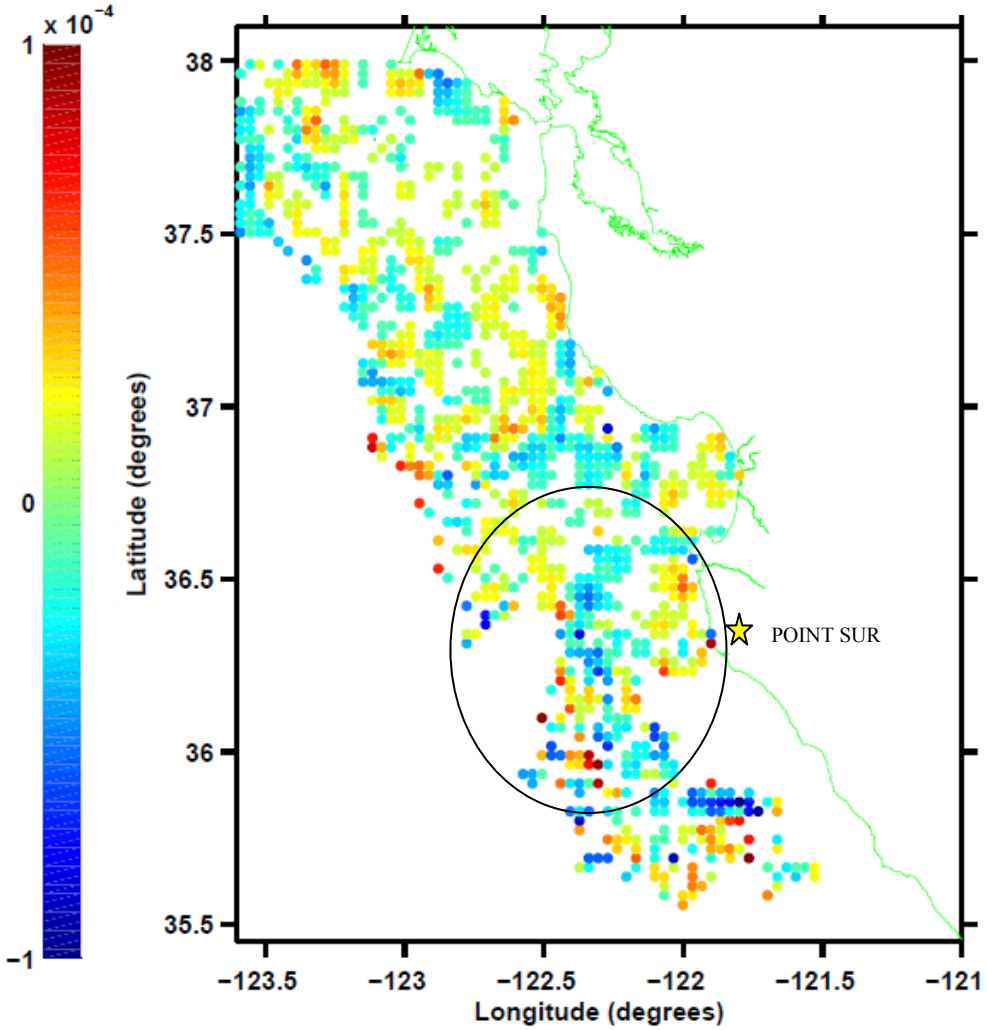

Figure 50. Divergence test shows a convergence (bluish dots inside the black circle) feature centered at 36.4N 122.25W, where the corresponding SAR image demonstrates a brighter frontal structure (Figure 49).

Figure 51 shows a detail of an anti-cyclonic eddy offshore of Monterey Bay. The HF-radar surface currents clearly demonstrate a vortical feature, and the SAR image

illustrates a darker core with brighter boundaries and the presence of slicks. With relatively low wind speed, the surface current enhancement role is captured on the SAR image.

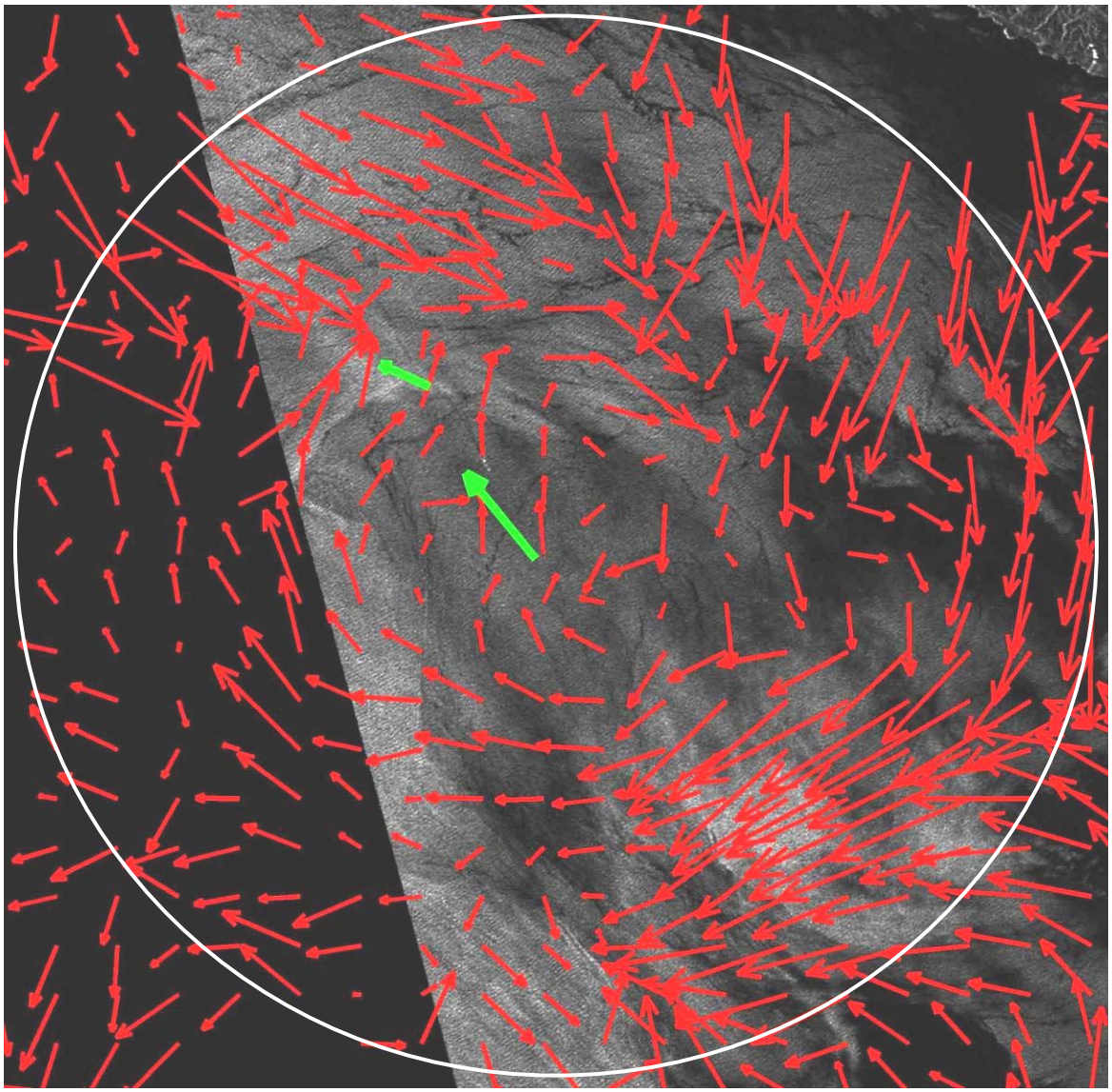

Figure 51. Detail of the SAR image sensed on 25 May 2008 at 0555 UTC with an anti-cyclonic eddy offshore of Monterey Bay, depicted by both SAR- and hourly-averaged HF-radar products (SAR data provided by ESA).

H. EXAMPLE 8 – SLICK OFF POINT SUR

North of Point Sur there's a narrow band feature oriented NE-SW that is seen on the Chlorophyll Concentration (Figure 52-A) and True Color (Figure 52-B) images from

10 February 2008 at 2155 UTC. Other bands are also detected in Monterey Bay. Figure 53 shows the corresponding SAR image at 0555 UTC, where a slick and frontal features are depicted close to Point Sur. This slick is related to productivity at the surface that dampens the SAR Bragg waves. The available HF-radar surface currents help assessing the flow patterns.

Other features seen in the SAR image are the edge of a fresh water plume in the San Francisco area imaged through a strong convergent front, as well as packets of internal waves in the Half Moon Bay and Pigeon Point areas.

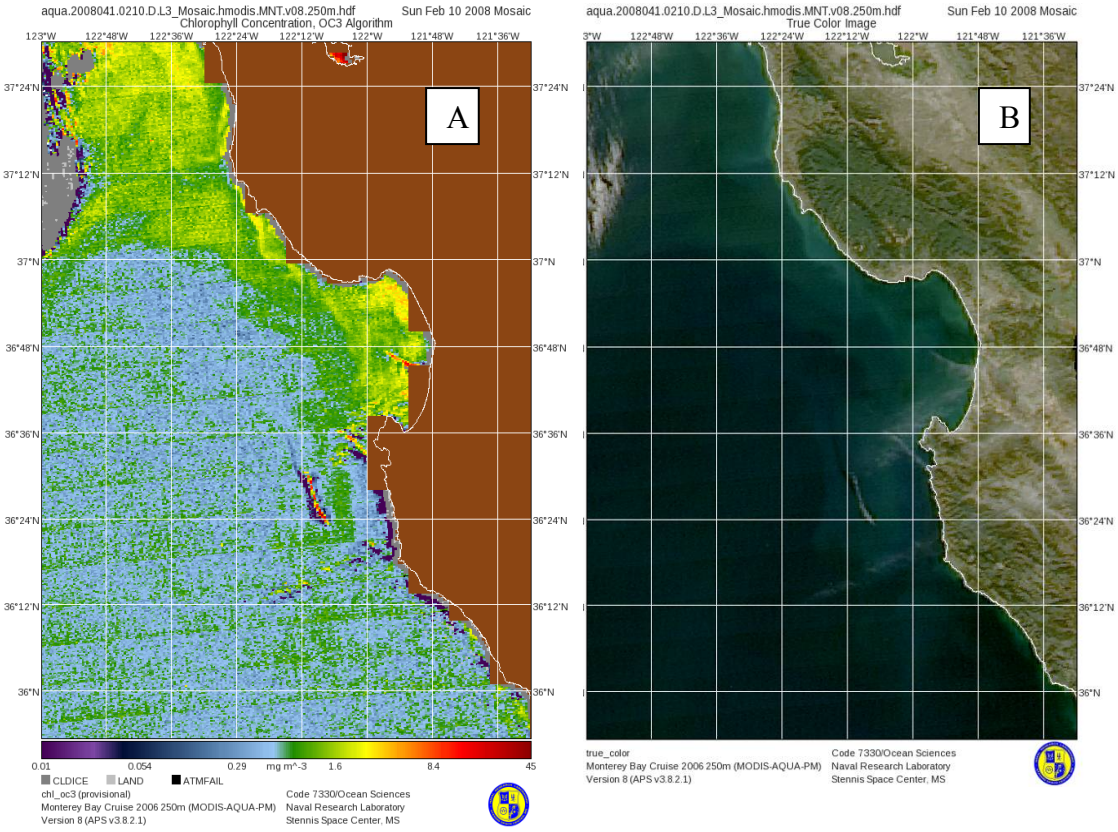

Figure 52. MODIS Chlorophyll Concentration and True Color products from 10 February 2008 at 2155 UTC showing a slick oriented NE-SW (After NLR, http://www7240.nrlssc.navy.mil/).

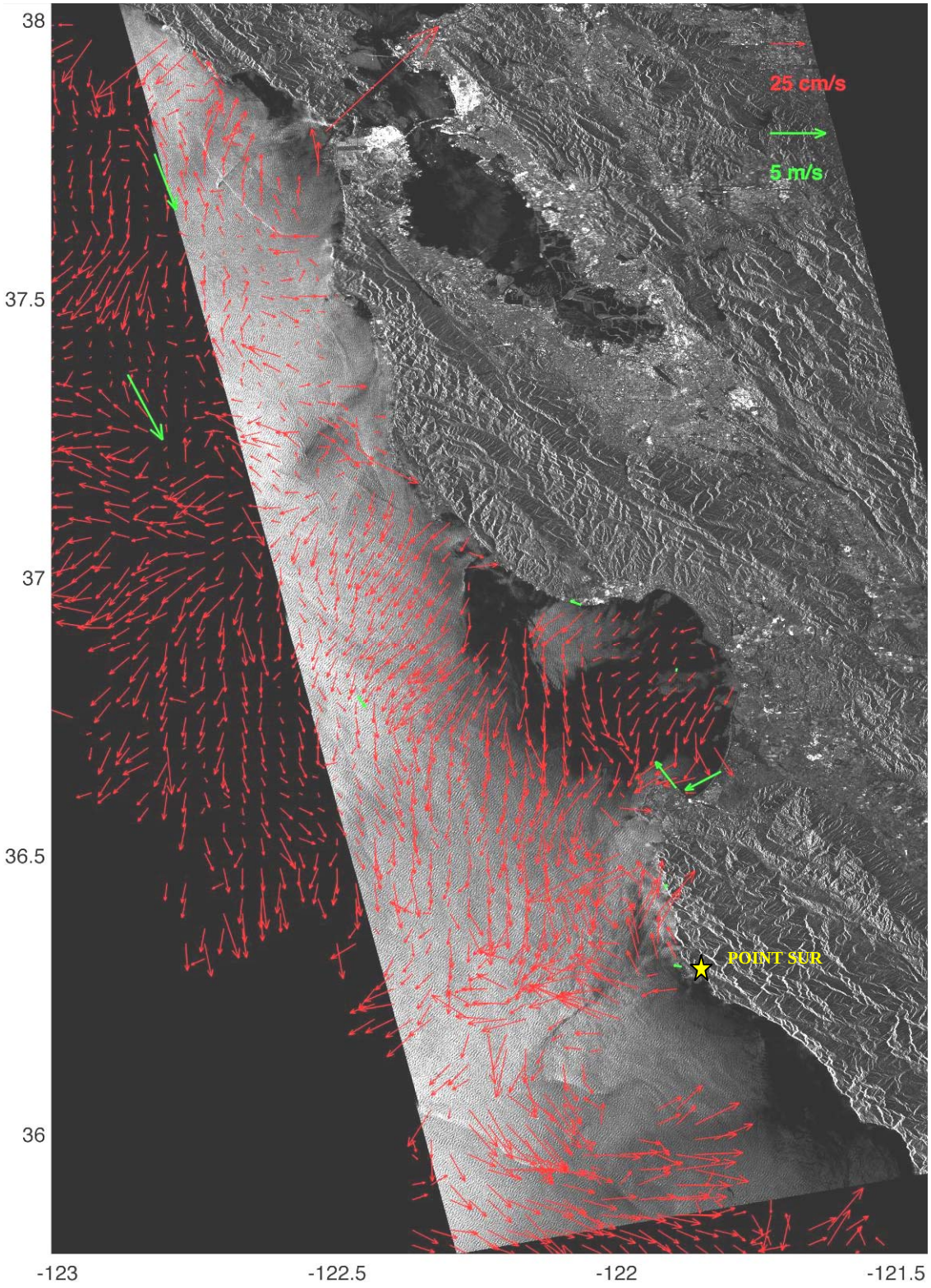

Figure 53. Image captured on 10 February 2008 at 0555 UTC. Close to Point Sur there's evidence of frontal features and a slick oriented NE-SW, which is illustrated in Figures 52 a) and b), as well (SAR data provided by ESA).

I. EXAMPLE 9 – ATMOSPHERIC FEATURES AND A CURIOUS RECTANGULAR FEATURE

The SAR image in Figure 54 was taken on 27 September 2009 at 0555 UTC and displays interesting atmospheric features south of 36N where the wind is predominantly from land (southeast). Atmospheric gravity waves with an approximately 2.5km wavelength and roll vortices originated by land features are seen in more detail in Figure 55. As described in Monaldo and Beal (2004) and Holt (2004), the SAR imaging mechanism present in these features is mainly wind stress.

A rectangular feature with dimensions 2.3 x 1.8km, located 32km offshore of Point Sur and with an apparently associated wake signature is shown in detail in Figure 56. This feature is also seen in MODIS True Color product illustrated in Figure 57.

The general circulation pattern of the hourly-average, HF-radar surface currents is seaward, where the near-concurrent SAR image illustrates lower backscatter (darker) regions close to shore, likely indicating upwelling of colder water and nutrients. Previous wind conditions demonstrate strong winds from northern quadrants, and a MODIS SST product imaged eight hours before the SAR passage agrees with the upwelling theory (Not shown here. Available at NRL webpage http://www7240.nrlssc.navy.mil/browse/lvl3/hmodis/Monterey250).

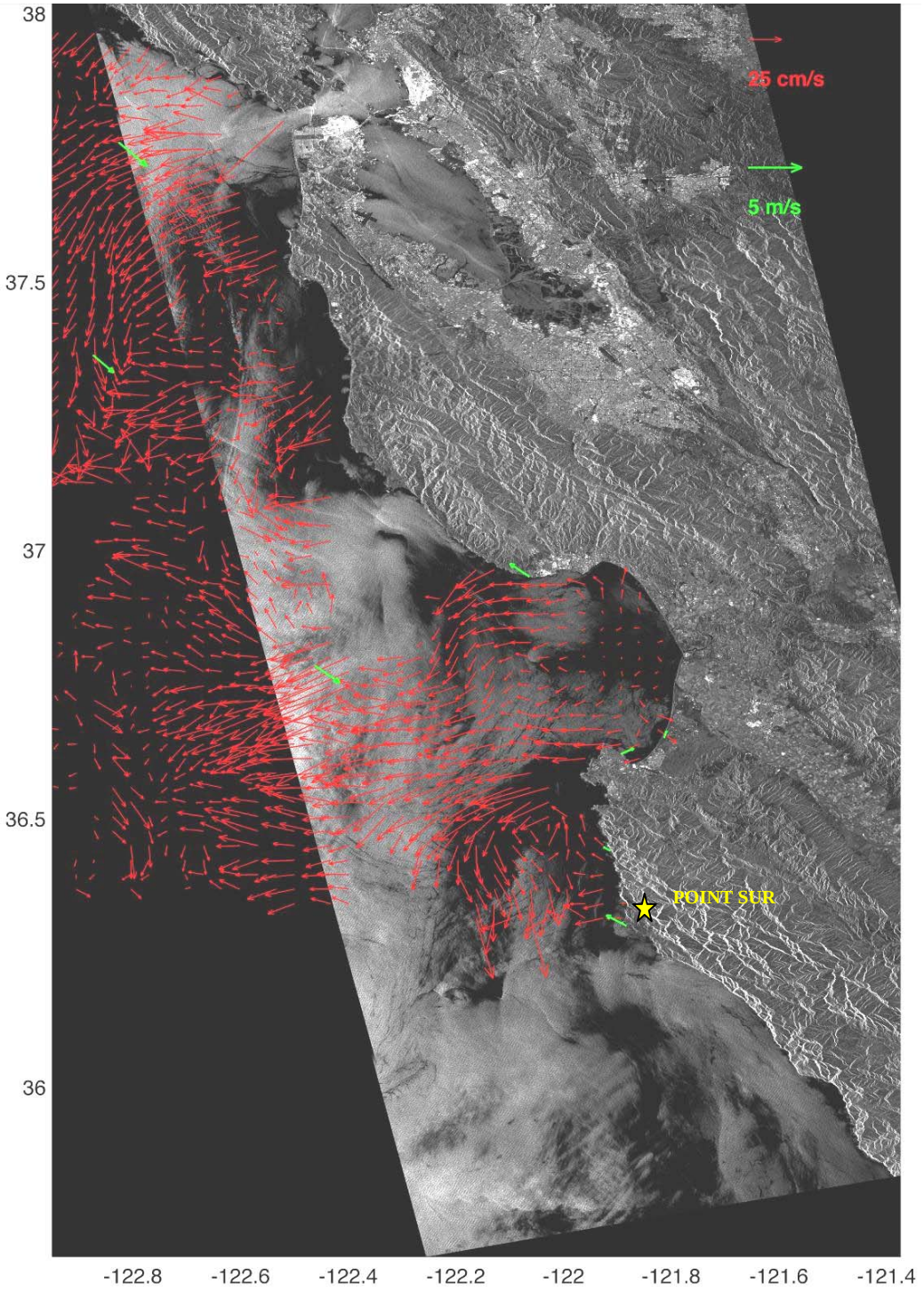

Figure 54. SAR image sensed on 27 September 2009 at 0555 UTC exemplifying atmospheric gravity waves and roll vortices originated by land features (see detail in Figure 55). The wind is weak and from the southeast. Offshore of Point Sur, there's a large rectangular feature (see detail in Figure 56). (SAR data provided by ESA).

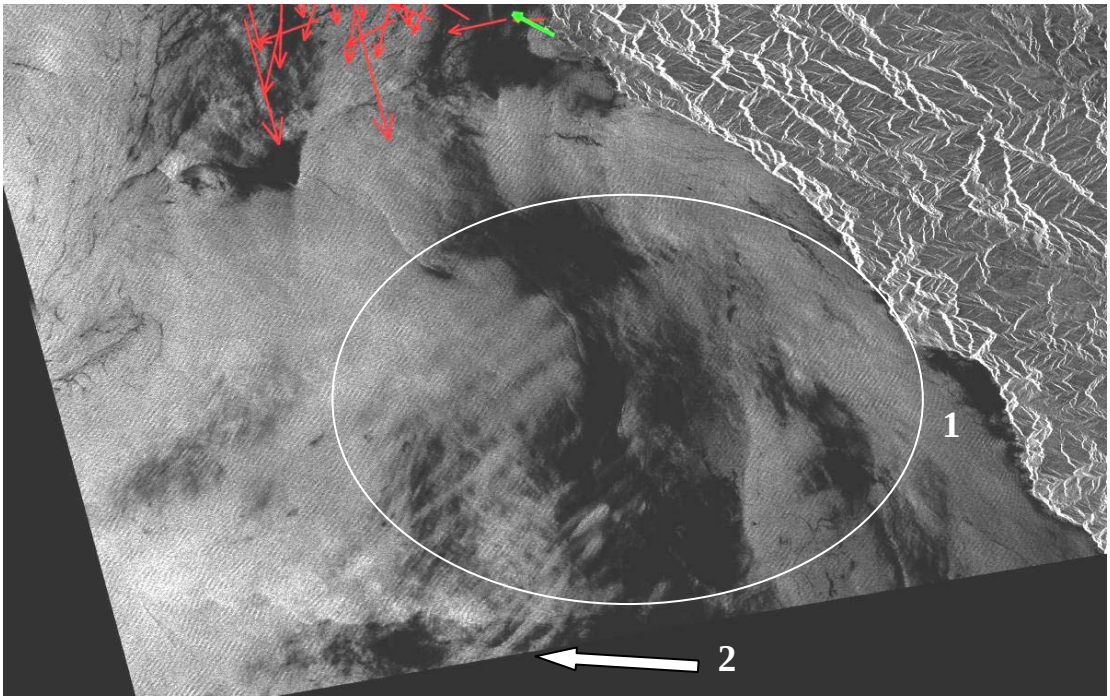

Figure 55. Detail of atmospheric gravity waves (1) and roll vortices (2) at the bottom of image captured on 27 September 2009 at 0555 UTC. The wind is weak and from the southeast. Offshore of Point Sur, there's a large rectangular feature (see detail in Figure 56). (SAR data provided by ESA).

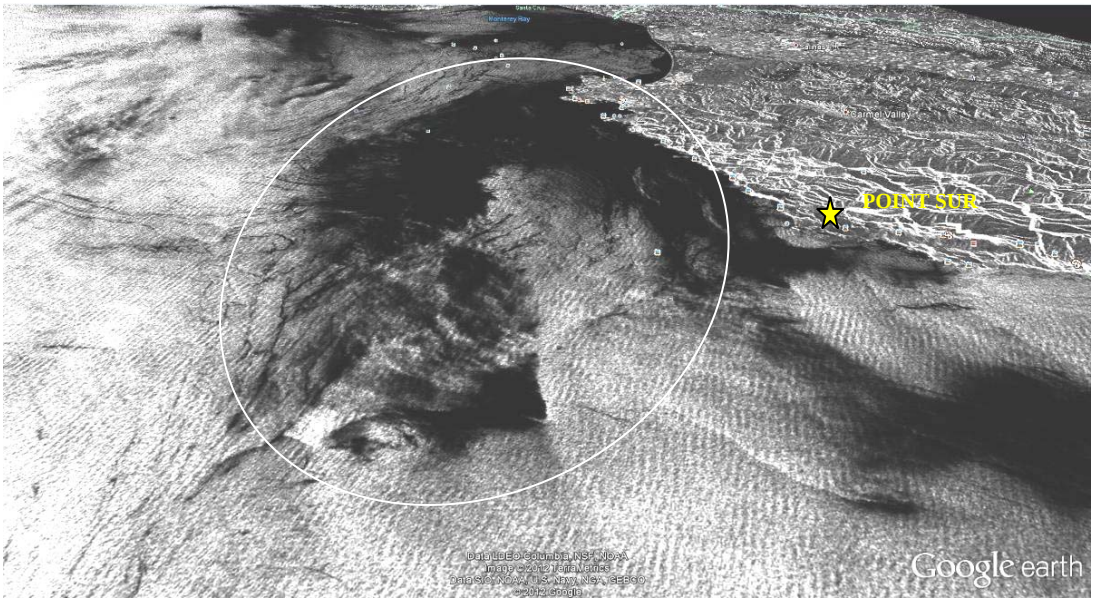

Figure 56. SAR image sensed on 27 September 2009 at 0555 UTC, showing a rectangular feature (2.3km x 1.8km) 32km offshore of Point Sur and a wake signature (SAR data provided by ESA).

Figure 57. MODIS Terra True Color product from 27 September 2009 at 1910 UTC showing atmospheric patterns in the Monterey Bay area. Note the rectangular feature SW of Point (After LANCE-MODIS, http://lance-modis.eosdis.nasa.gov/imagery/subsets/?project=aeronet&subset=Monterey).

V. CONCLUSIONS

A. DISCUSSION

The actual data set, where HF-radar surface currents and wind measurements overlap the SAR imagery, does not provide a clear assessment of comparable larger-scale ocean features retrieved by both remote sensors.

The imaging mechanisms found in the SAR imagery, identified in Table 5, are advection of surfactants, convergence/divergence, and atmospheric instability effects. The main constituent driving the surface roughness and allowing the visualization of backscatter gradients' is wind stress at the surface level. This study focused on the examination of ocean current contributions to surface variations.

A principal hypothesis of the present investigation is to assess the existence of ocean features in the SAR imagery that are correlated to the surface currents as perceived by HF radar. Some results show ocean features retrieved by HF radar and imaged by SAR provided the local wind has low intensity, the current field is strong, and the features are large enough. However, a consistent pattern has not been established. The divergence validation test performed in the selected cases (Chapter IV Examples 6 and 7) is positive and encouraging, yet a general conclusion could not be made.

There are several possible reasons contributing to a scarcely direct correlation between HF radar-derived surface currents and SAR ocean features, including:

- Surface currents changes to the surface roughness maybe overwhelmed by wind stress contributions. Surface wind is 10 to 20 times more intense than current flow.
- Indirect contribution of the surface current sensed by HF radar via short gravity waves ($\lambda \sim 12m$) compared with the direct effect of wind on the capillary waves sensed by SAR ($\lambda = 5.6cm$ for C-band).
- Poor alignment of the time scales. Although SAR captures the surface image in a 15-second snapshot, it mirrors the resulting distortions preceding atmospheric and oceanic processes of hours-to-days. HF radar maps, on the other hand, represent an hourly-average product of the surface currents, which becomes more instantaneous than the SAR image.

One possibility to bridge the temporal differences between instantaneous HF-radar currents and SAR images is the approach followed in Examples 3 and 5 of Chapter IV that suggests the use of an HF-radar, daily-average, surface-current map in which tidal and sea breeze effects are naturally removed, instead of the hourly-average product.

For the ROI (Figure 1) and the actual data set, the research revealed some recurring events such as: an outward plume detected in San Francisco and its dispersion in a bathymetry-wise shape; the manifestation of internal waves in the Half Moon Bay and Point Pigeon areas; upwelling events along the coast; the occurrence of eddies in and offshore of Monterey Bay; wind shadowing effects in the north part of Monterey Bay; current field structures and the presence of biogenic material at the surface, both in the Point Sur area; and the appearance of atmospheric gap flows and gravity waves.

The present research demonstrates that the SAR imagery is sensitive to wind speed and each SAR image has different levels of wind intensity in different parts of the image. Thus, it becomes problematic to quantitatively establish optimal wind intervals for specific ocean features and imaging mechanisms in certain regions. The wind thresholds found in this study agree with Table 5 and the discussion in Holt (2004, Table 2.1). Wind speeds below 2-3 m/s cause SAR ocean features to fade and merge with noise levels, though the appropriate enhancement of surface roughness by other imaging processes can lead to the improved sensing of oceanic features. This study revealed that surface winds of 2-4 m/s constitute the suitable level of wind speed required to make assessments of oceanic surface currents influence on SAR images. Hence, future studies in this area should consider assessing SAR data in seasons and time of day when wind speeds are moderate. Strong wind speeds of 10-12 m/s may cause wind clutter to mask most of the ocean surface features and, in cases of large fetch, it may lead to a well-organized atmospheric imprints on the surface layer as demonstrated in Chapter IV, Example 1.

Some examples in Chapter IV made evident the importance of the HF-radar surface current field in interpreting and identifying flow configurations in SAR images (Examples 5 and 7). Other examples demonstrated the complementary role of SST, ocean color, and chlorophyll concentration products when combined with corresponding SAR images (Examples 3 and 8). For instance, under conditions of partial cloud cover, SAR

can be used to fill in the gaps and connect SST fronts masked by clouds. Hence, a combination of the available remote sensors yields synergetic gains to the understanding of the ocean and its processes.

B. FUTURE RESEARCH

Future studies in the field should consider the wind conditions that distort the surface prior to SAR sensing and select SAR data where wind speed is weak. Knowledge of the surface current field, tides, and upwelling and downwelling events also assumes a relevant role, in which the 24-hour, HF-radar, surface-current trajectories and the daily-averaged, HF-radar, surface currents are preferred.

Another approach to the assessment of surface currents by HF and SAR is to derive the line-of-sight Doppler shift induced by the motion of the ocean surface (Danilo et al., 2005; Chapron et al., 2005). ENVISAT's ASAR provided a decade of data in which estimations of the Doppler centroid have served to retrieve ocean surface velocities, generally over very energetic regions of the ocean such as the Agulhas and Gulf Stream (Hansen et al., 2011; Johannessen et al., 2008; Rouault et al., 2010). The Sentinel-1 satellite, the ENVISAT follow-on estimated to be launched in 2013, will have improved capabilities in providing a more accurate Doppler centroid and, thus, stepping forward to superior research (Hansen et al., 2011).

THIS PAGE INTENTIONALLY LEFT BLANK

APPENDIX A

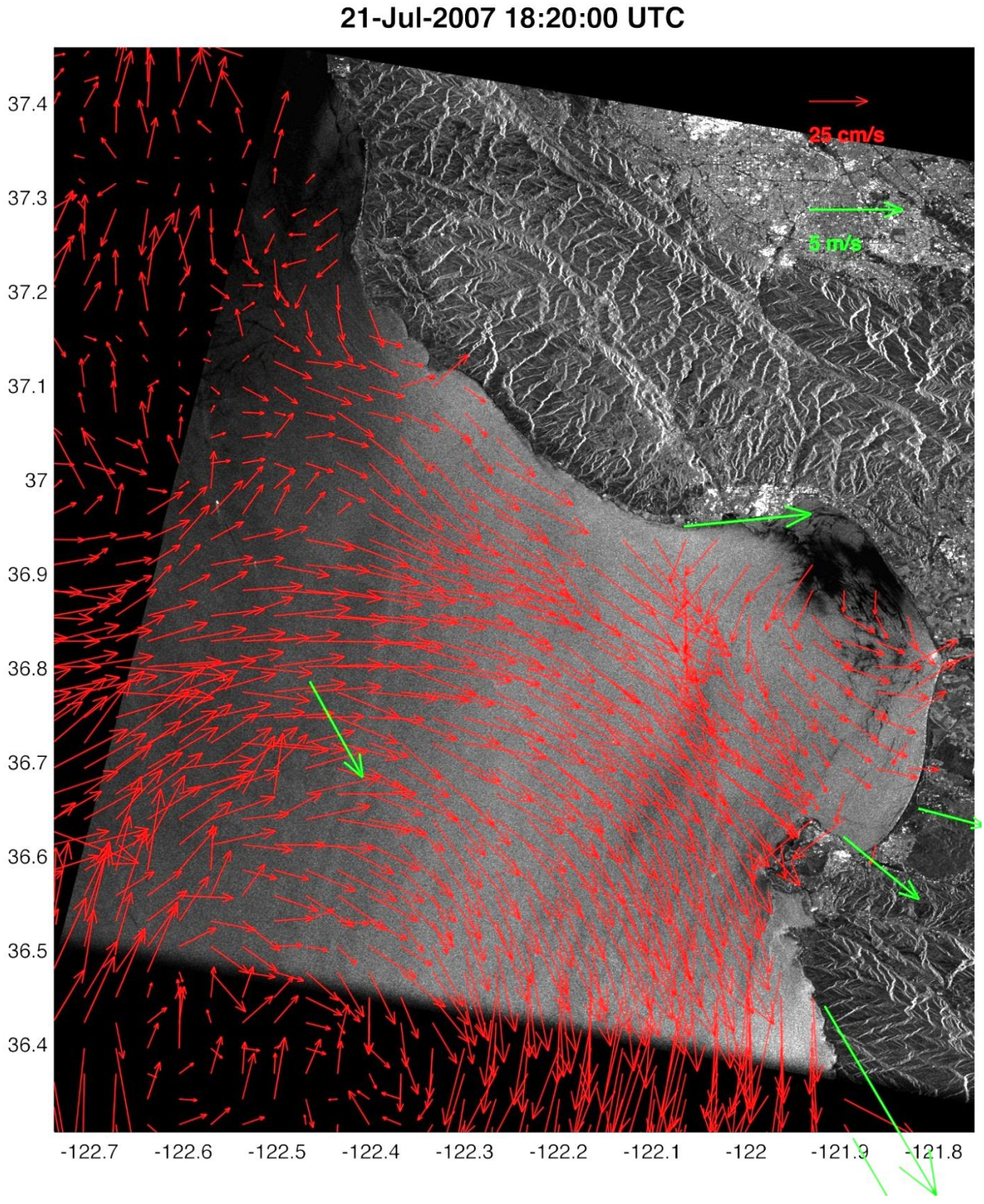

Figure 58. SAR image from 21 July 2007 at 1820 UTC and HF radar currents (red) and surface winds (green) from the closest hour (SAR data provided by ESA).

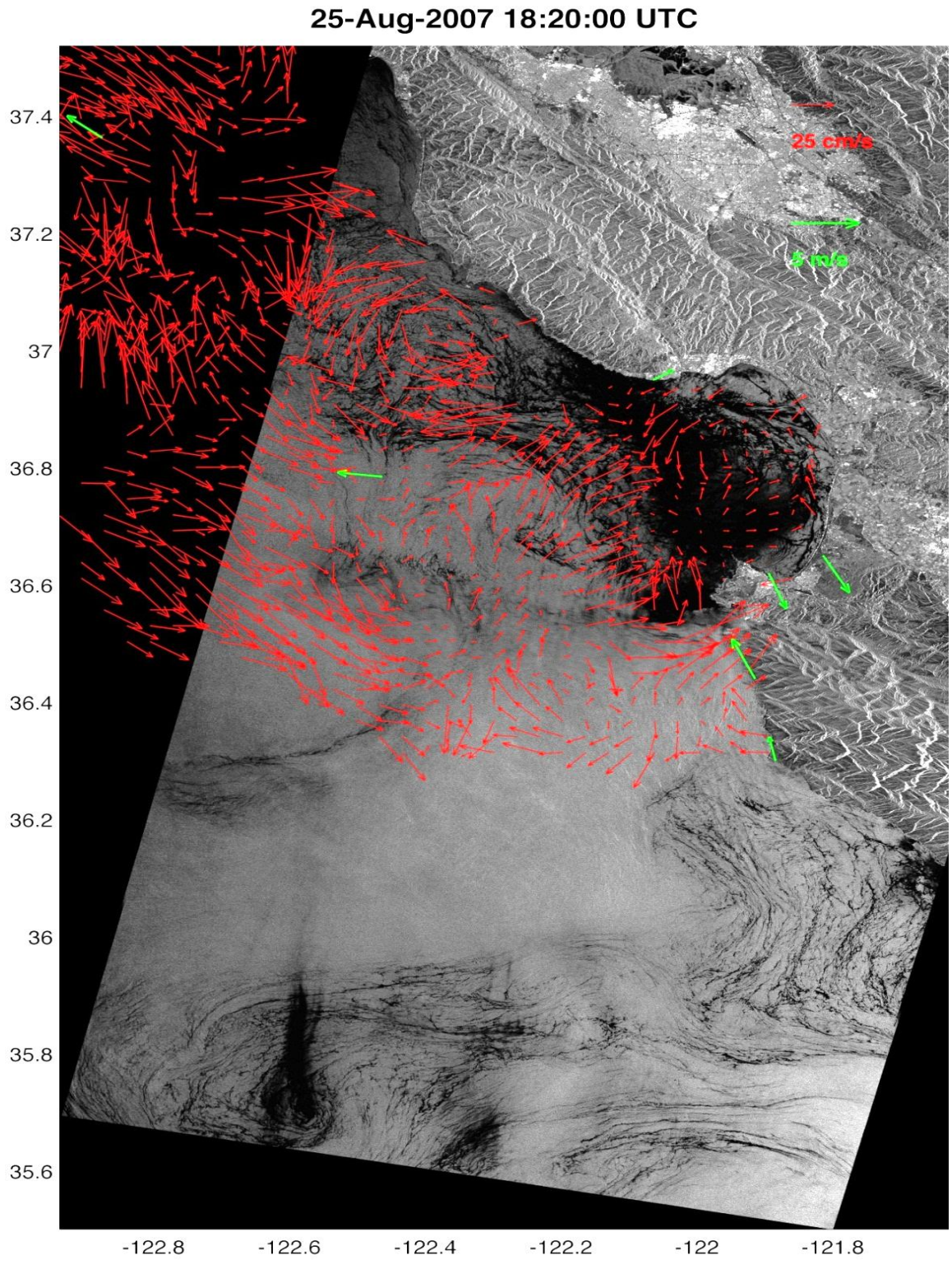

Figure 59. SAR image from 25 August 2007 at 1820 UTC and HF radar currents (red) and surface winds (green) from the closest hour (SAR data provided by ESA).

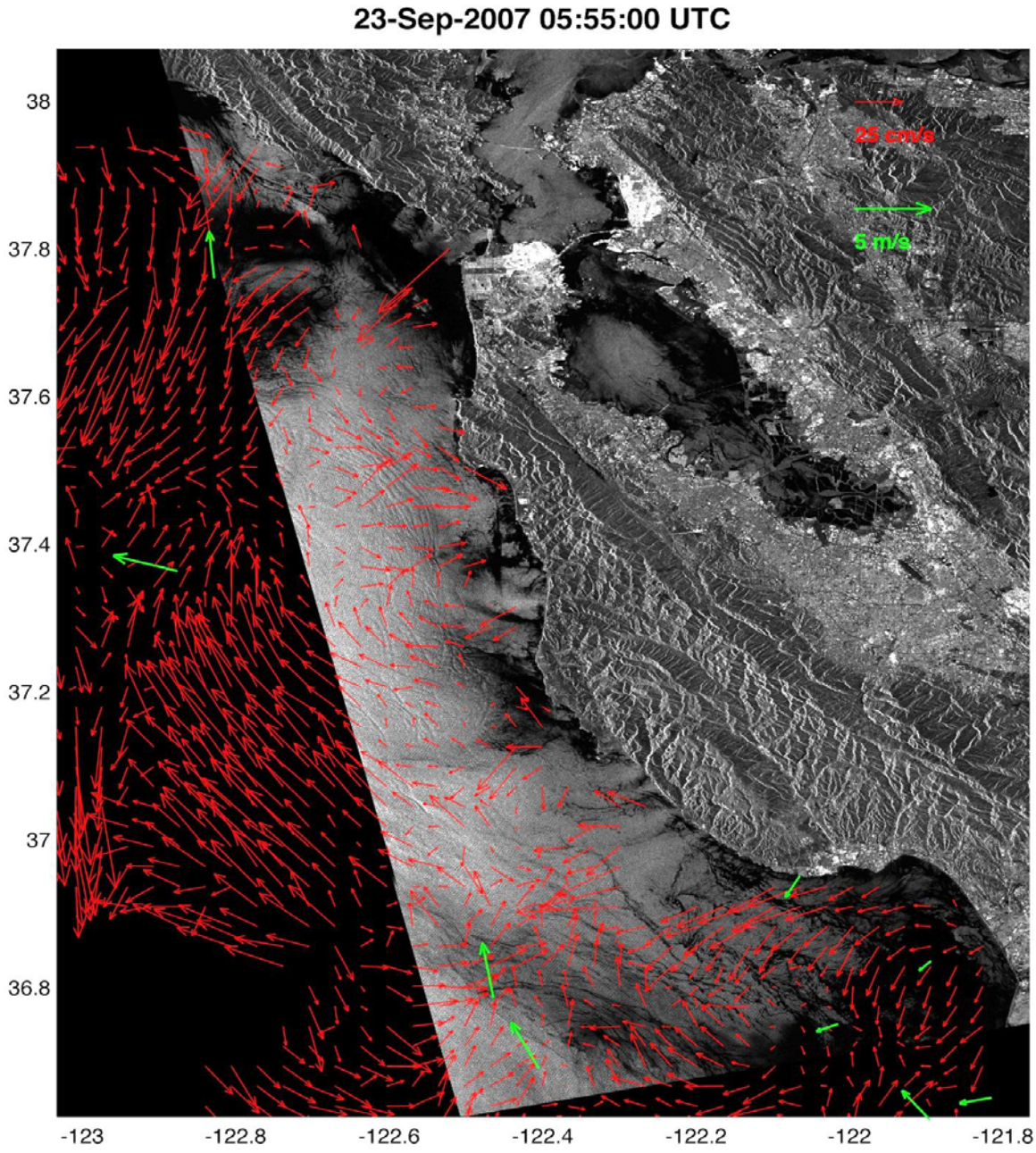

Figure 60. SAR image from 23 September 2007 at 0555UTC and HF radar currents (red) and surface winds (green) from the closest hour (SAR data provided by ESA).

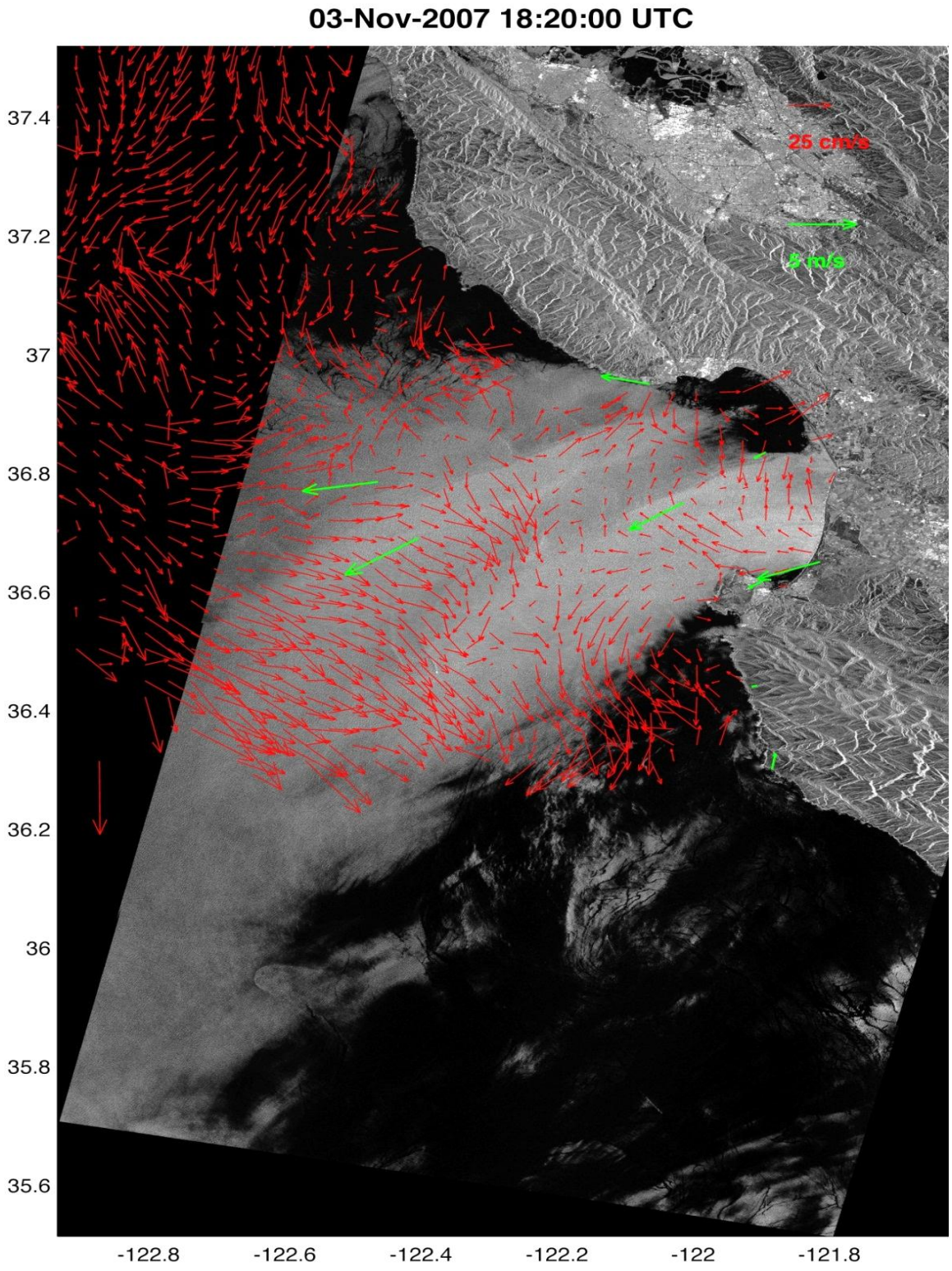

Figure 61. SAR image from 3 November 2007 at 1820 UTC and HF radar currents (red) and surface winds (green) from the closest hour (SAR data provided by ESA).

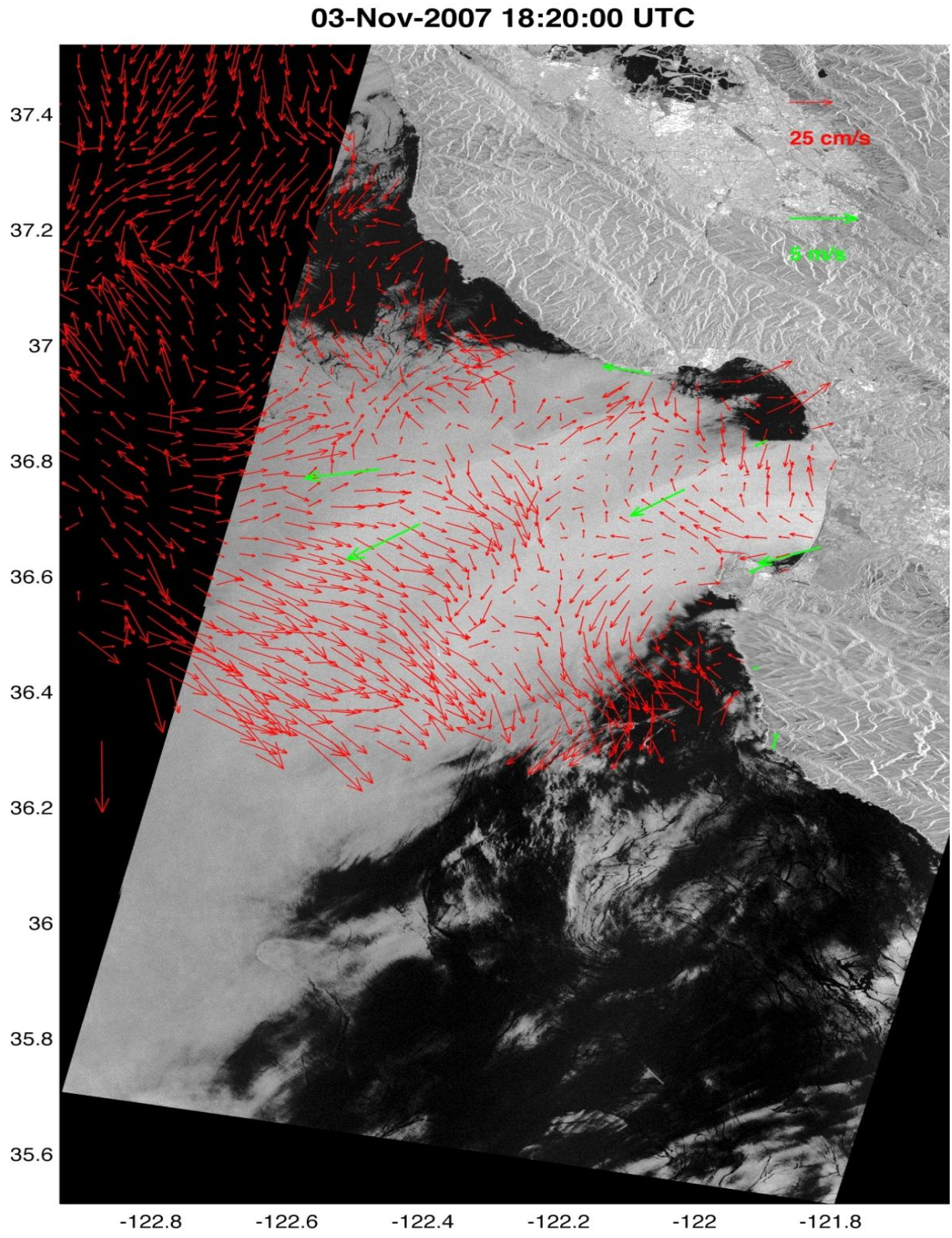

Figure 62. SAR image from 3 November 2007 at 1820 UTC and HF radar currents (red) and surface winds (green) from the closest hour (SAR data provided by ESA).

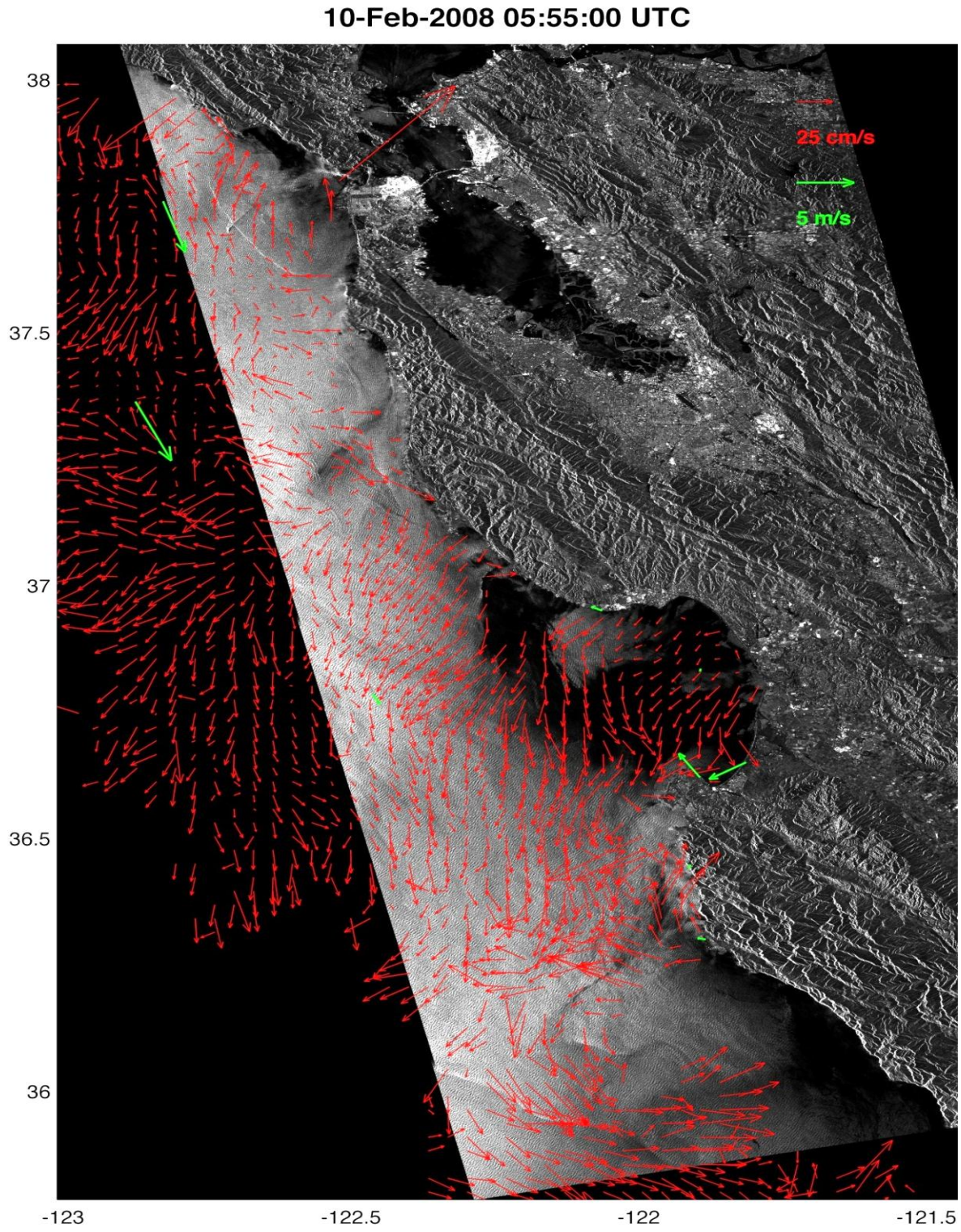

Figure 63. SAR image from 10 February 2008 at 0555 UTC and HF radar currents (red) and surface winds (green) from the closest hour (SAR data provided by ESA).

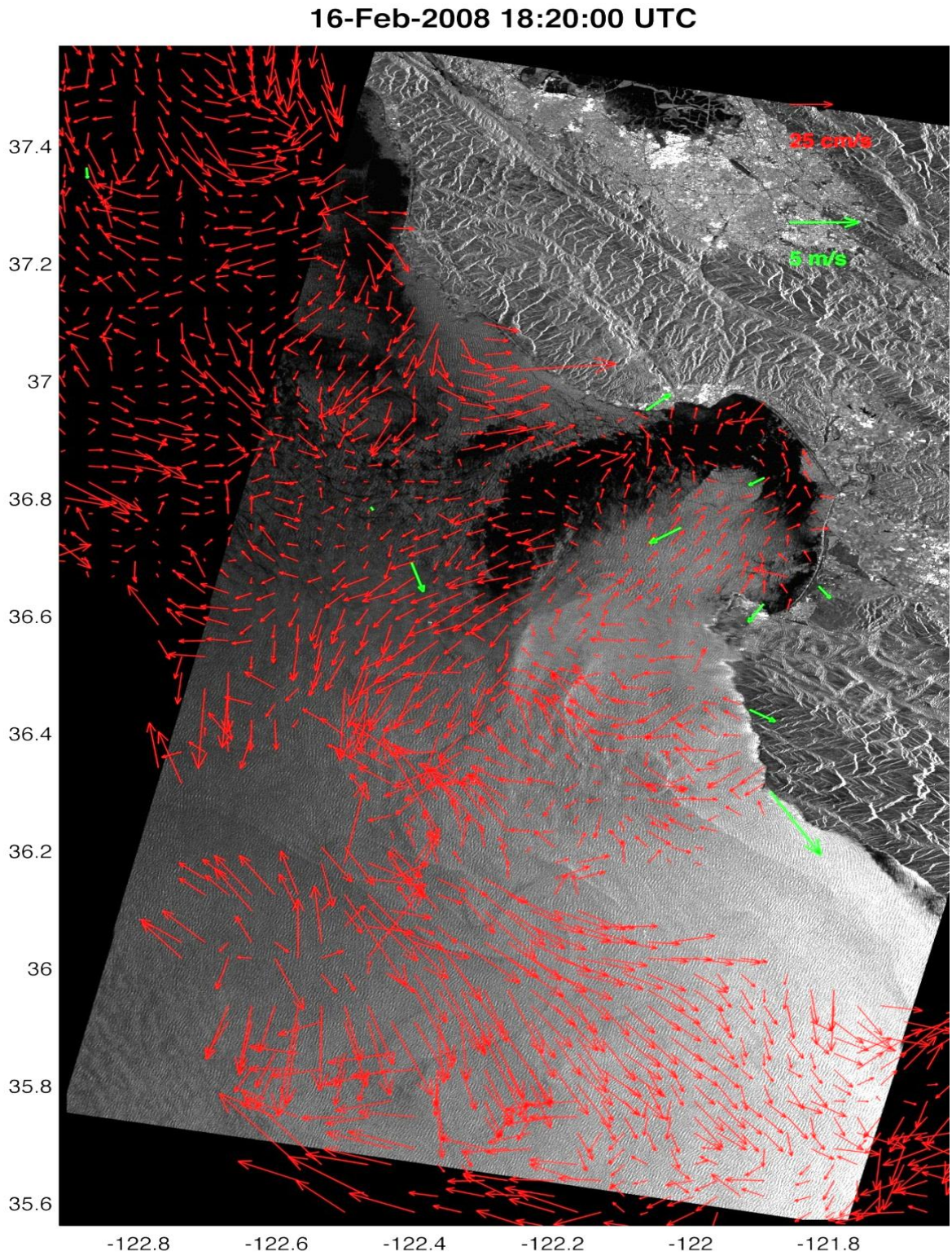

Figure 64. SAR image from 16 February 2008 at 1820 UTC and HF radar currents (red) and surface winds (green) from the closest hour (SAR data provided by ESA).

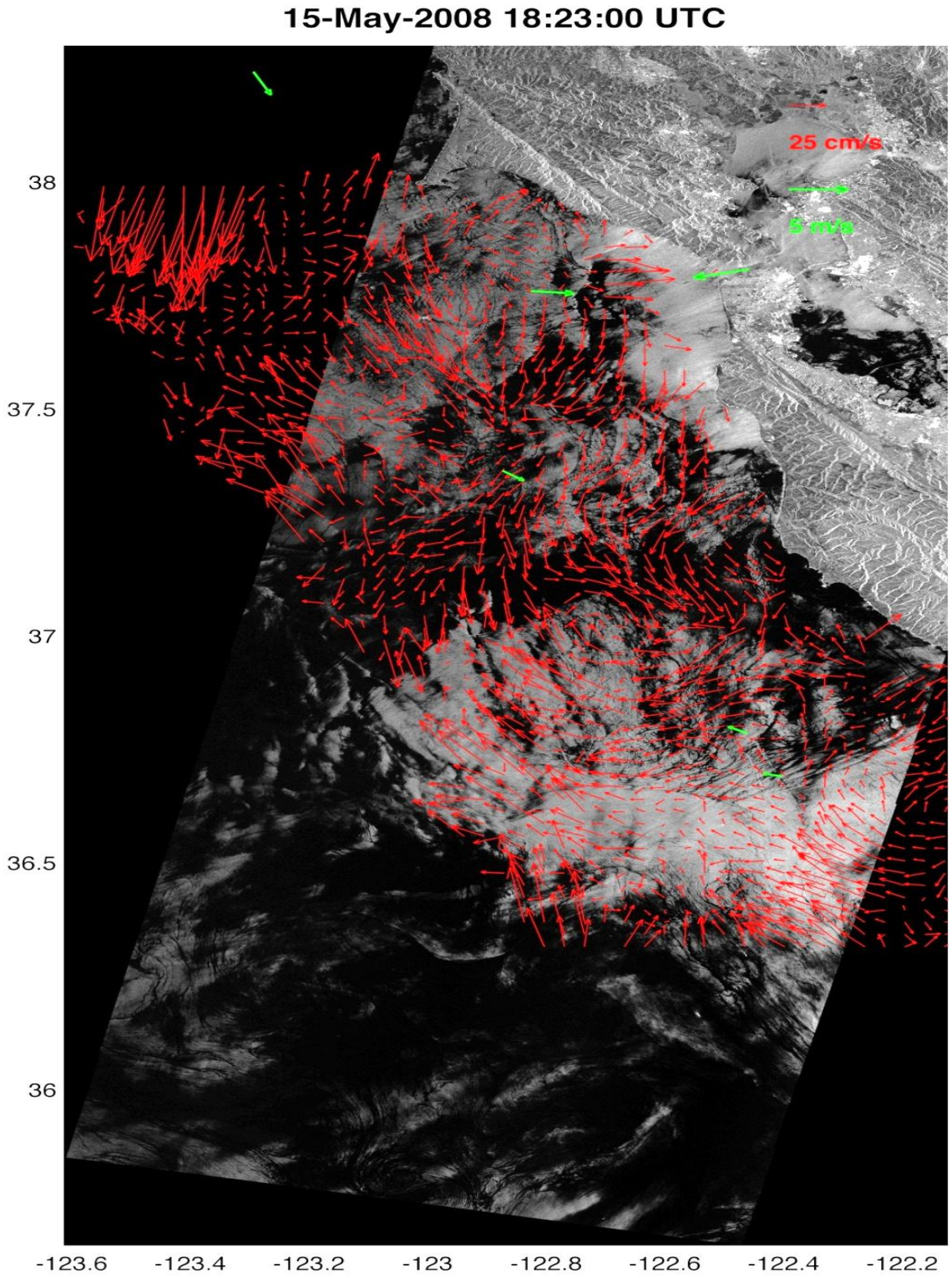

Figure 65. SAR image from 15 May 2008 at 1823 UTC and HF radar currents (red) and surface winds (green) from the closest hour (SAR data provided by ESA).

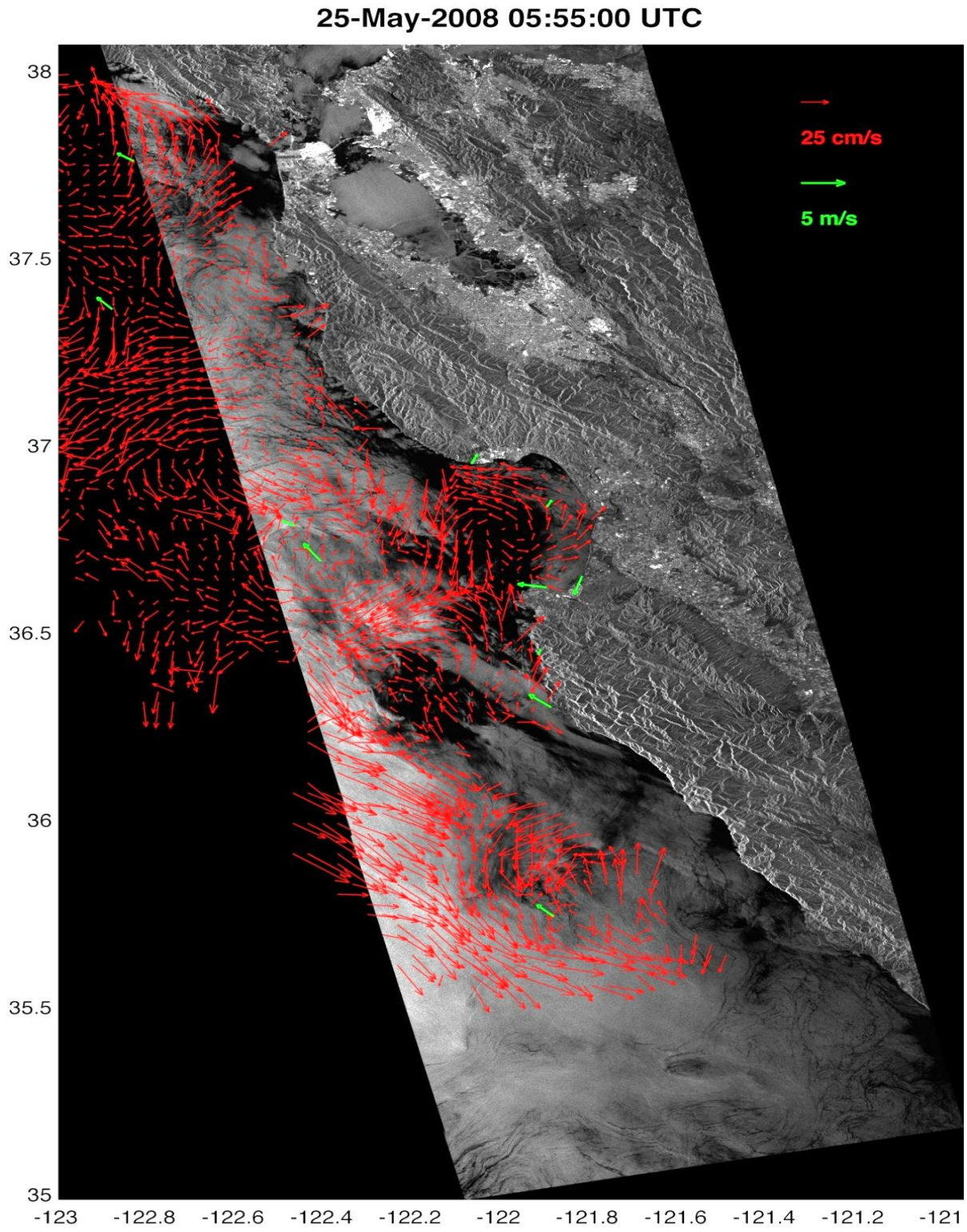

Figure 66. SAR image from 25 May 2008 at 0555 UTC and HF radar currents (red) and surface winds (green) from the closest hour (SAR data provided by ESA).

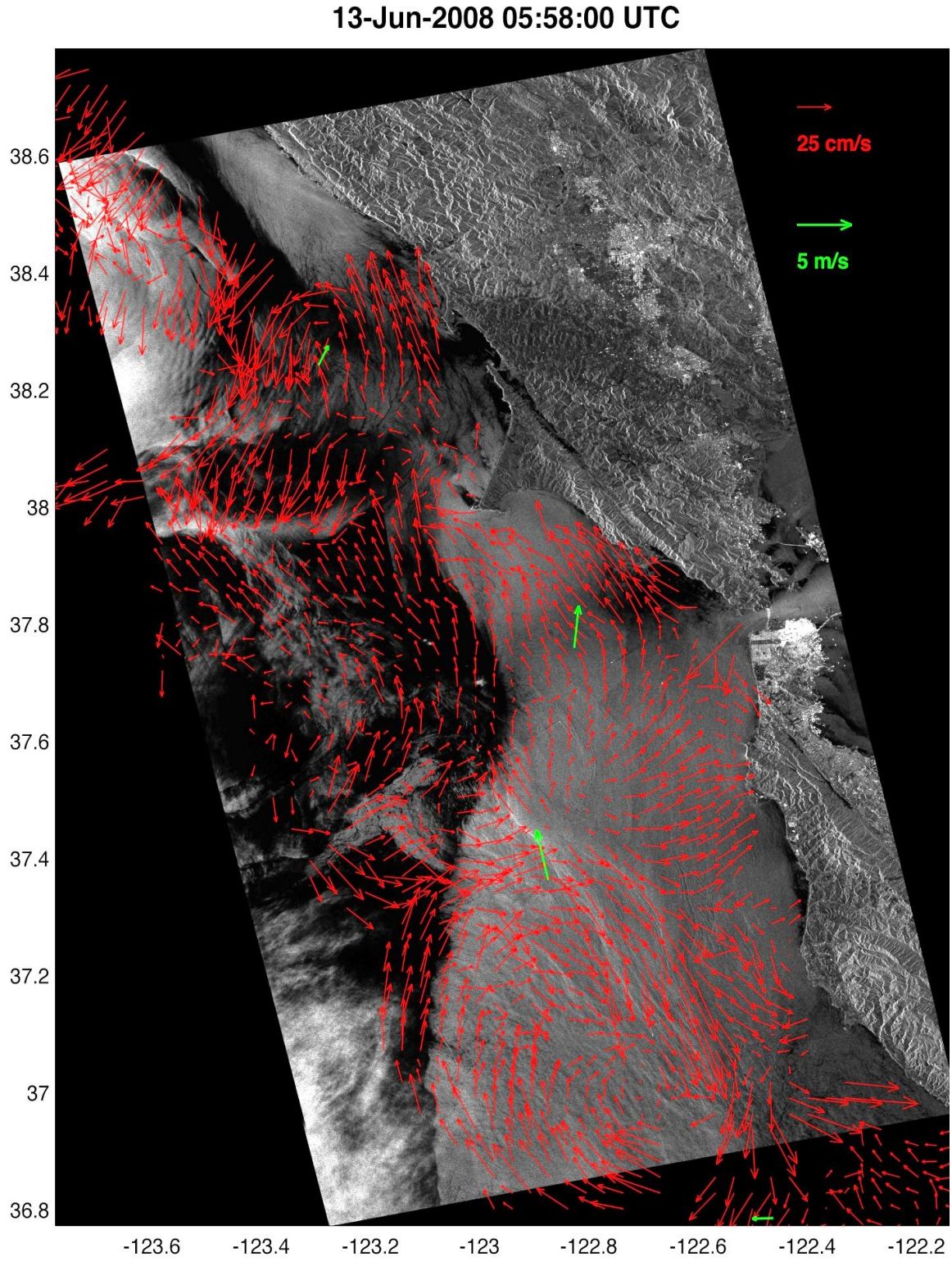

Figure 67. SAR image from 13 June 2008 at 0558 UTC and HF radar currents (red) and surface winds (green) from the closest hour (SAR data provided by ESA).

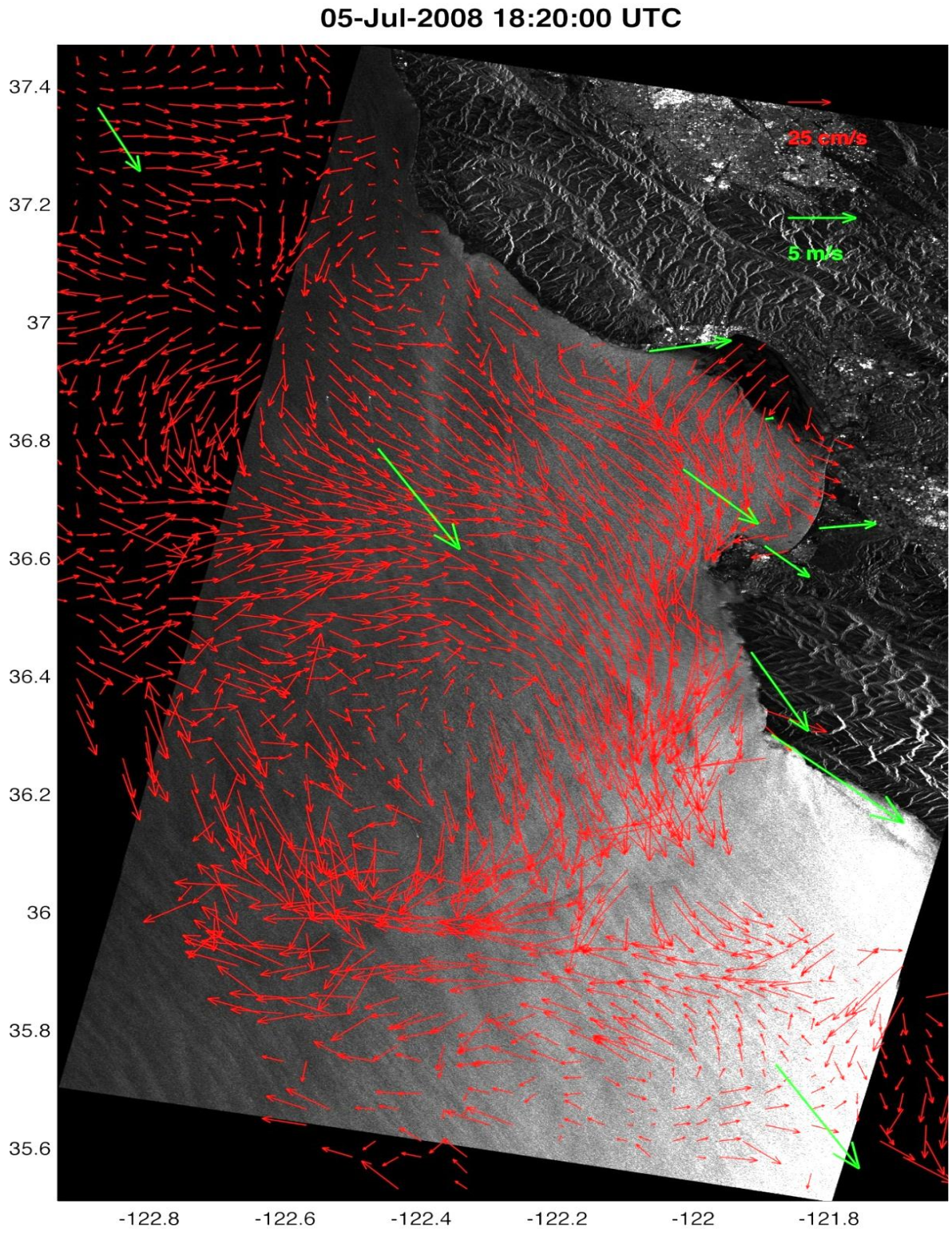

Figure 68. SAR image from 05 July 2008 at 1820 UTC and HF radar currents (red) and surface winds (green) from the closest hour (SAR data provided by ESA).

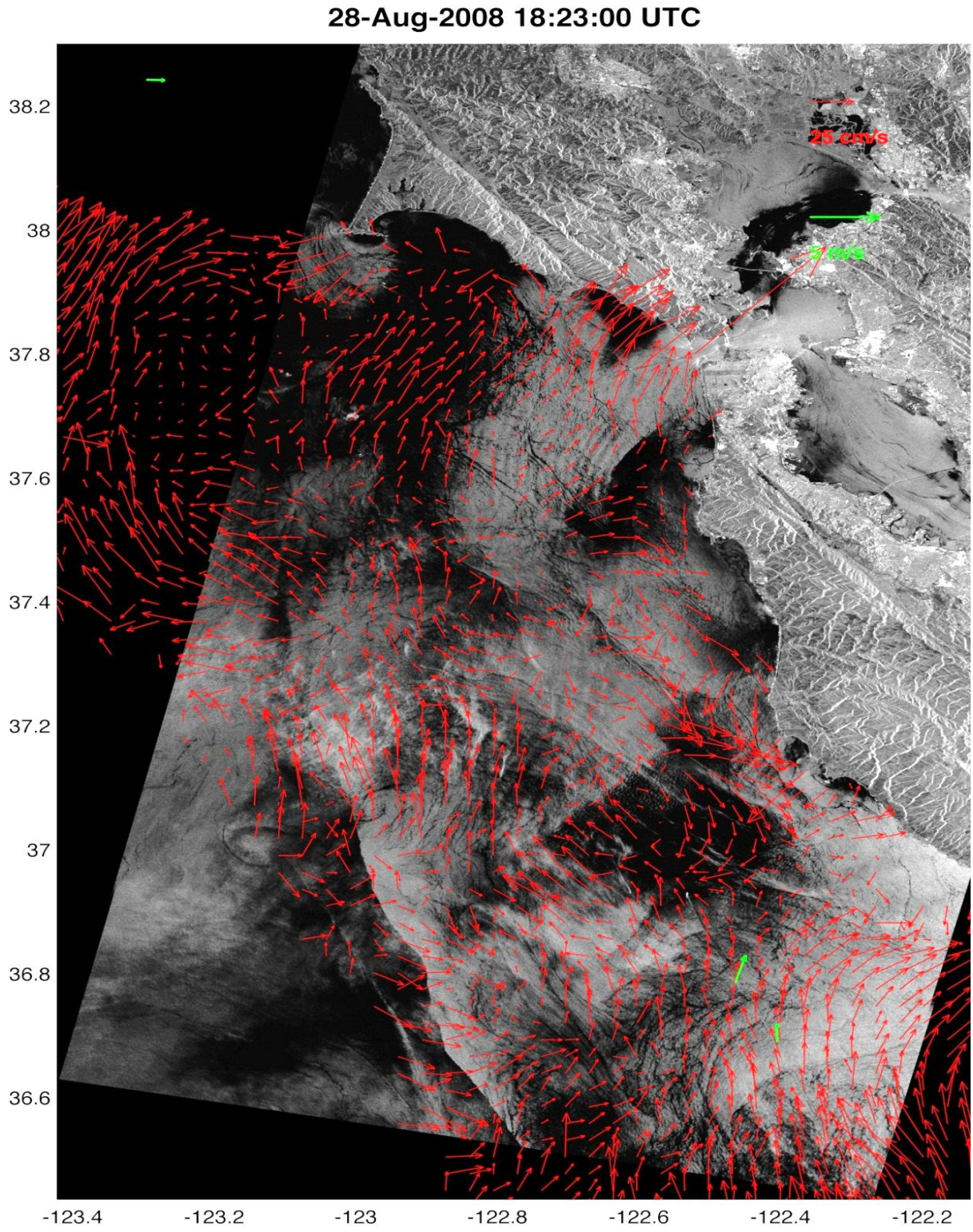

Figure 69. SAR image from 28 August 2008 at 1823 UTC and HF radar currents (red) and surface winds (green) from the closest hour (SAR data provided by ESA).

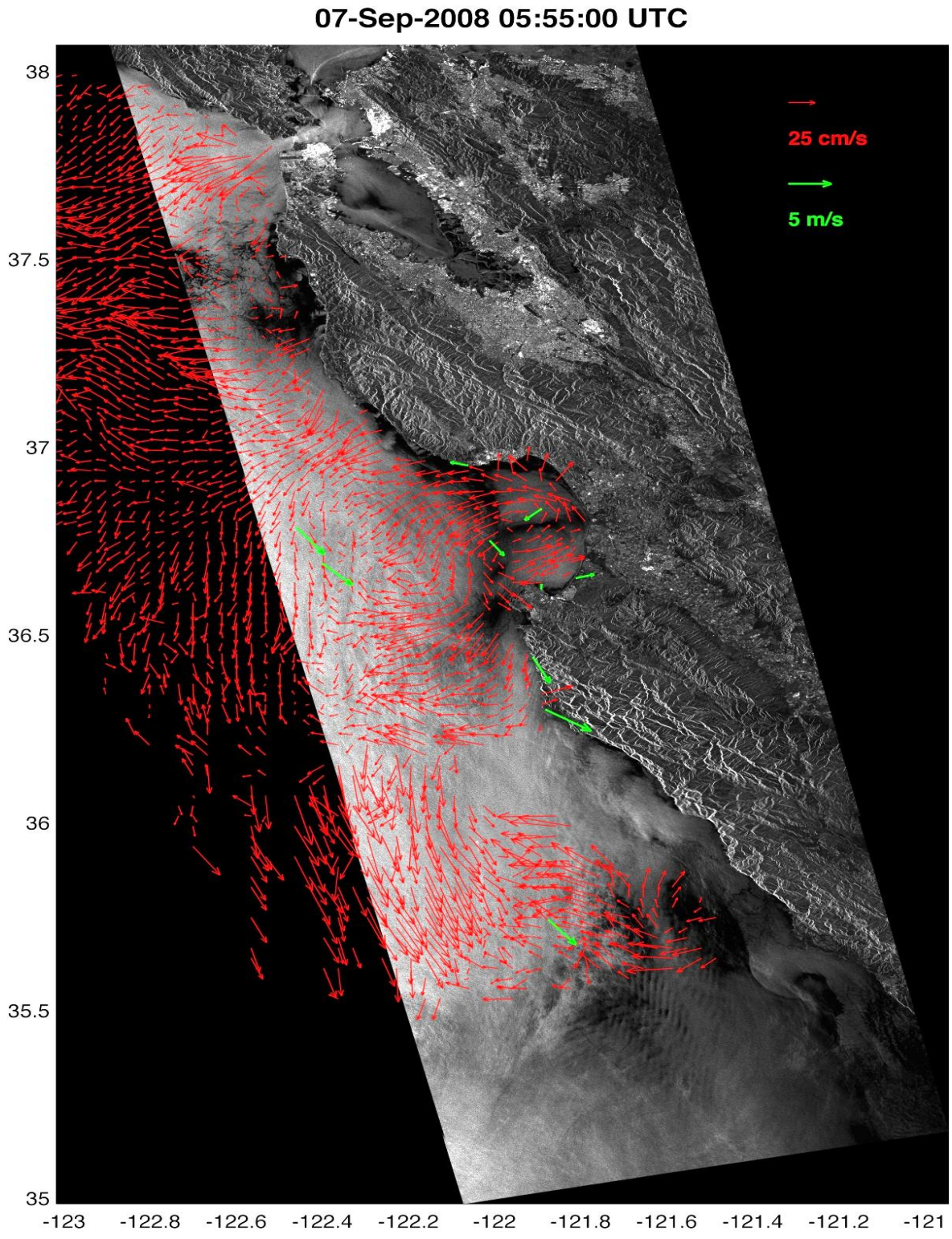

Figure 70. SAR image from 7 September 2008 at 0555 UTC and HF radar currents (red) and surface winds (green) from the closest hour (SAR data provided by ESA).

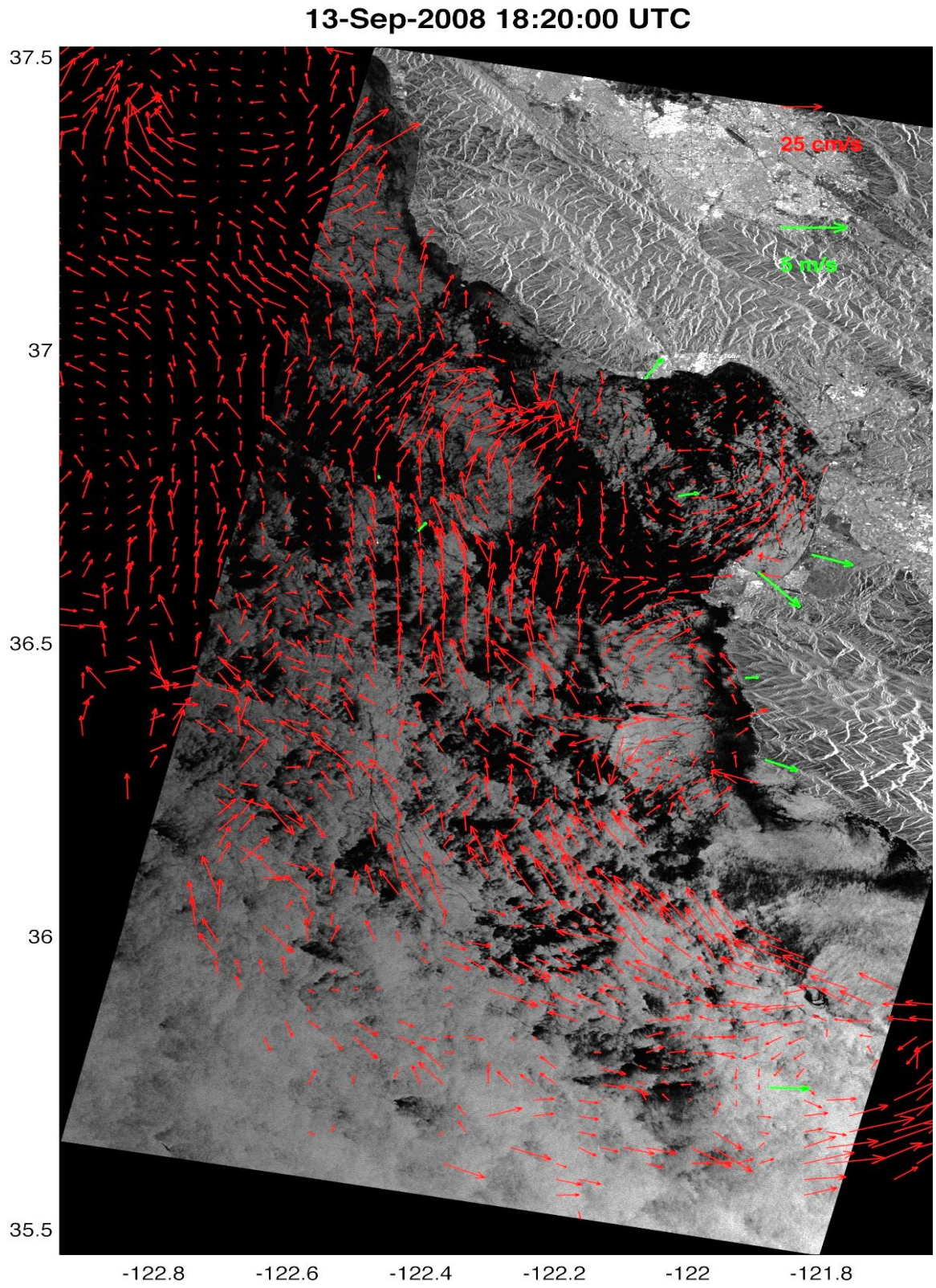

Figure 71. SAR image from 13 September 2008 at 1820UTC and HF radar currents (red) and surface winds (green) from the closest hour (SAR data provided by ESA).

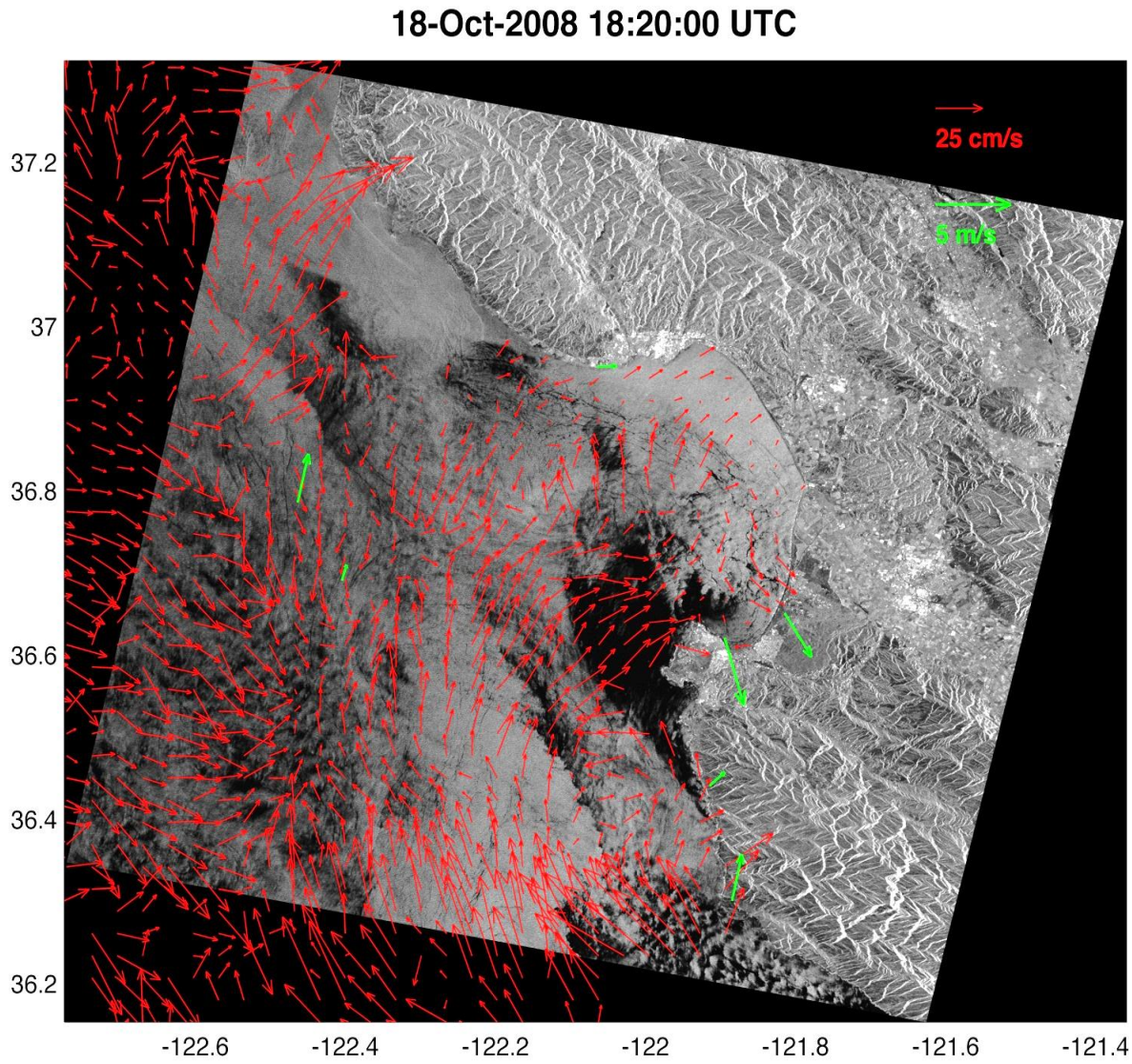

Figure 72. SAR image from 18 October 2008 at 1820 UTC and HF radar currents (red) and surface winds (green) from the closest hour (SAR data provided by ESA).

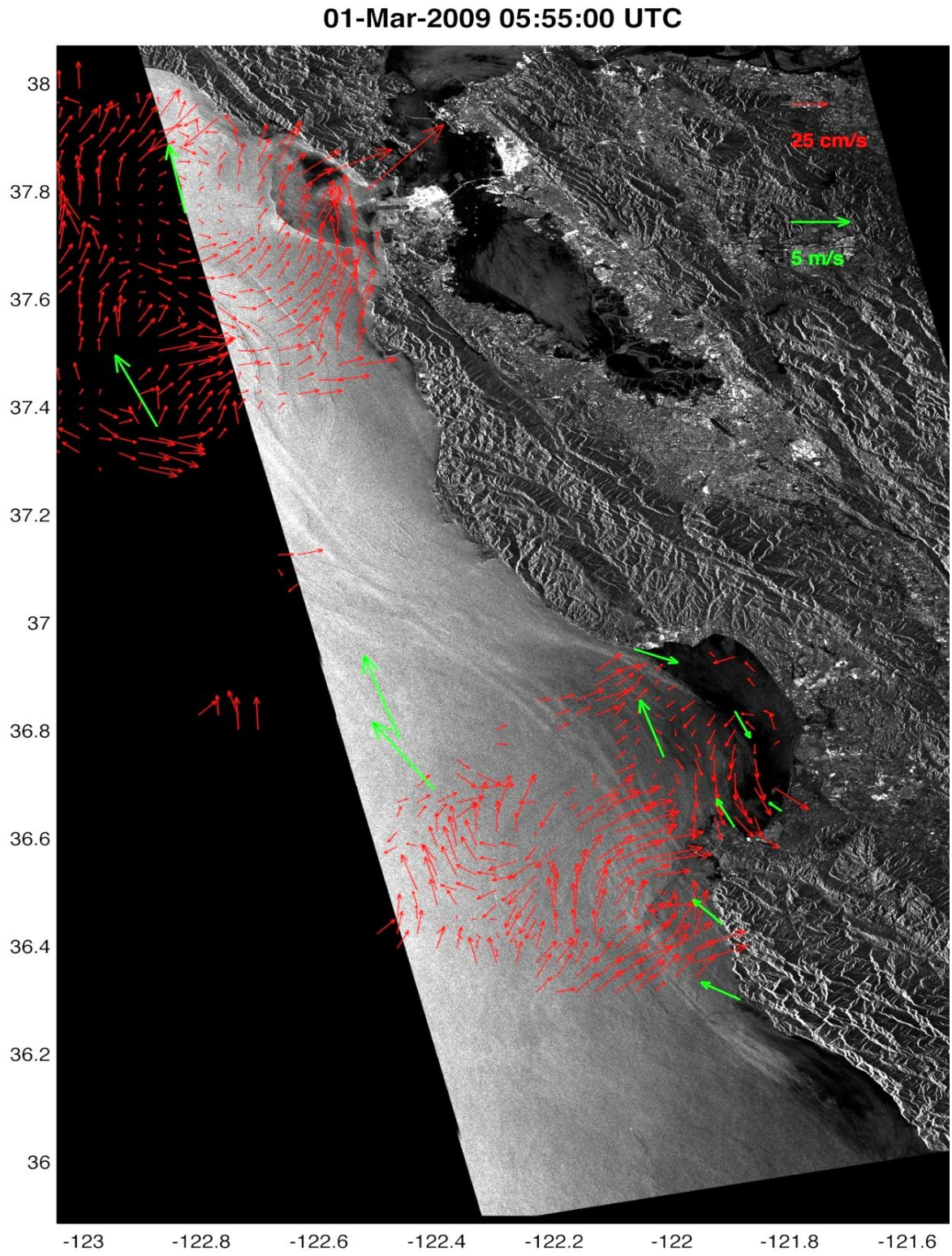

Figure 73. SAR image from 1 March 2009 at 0555 UTC and HF radar currents (red) and surface winds (green) from the closest hour (SAR data provided by ESA).

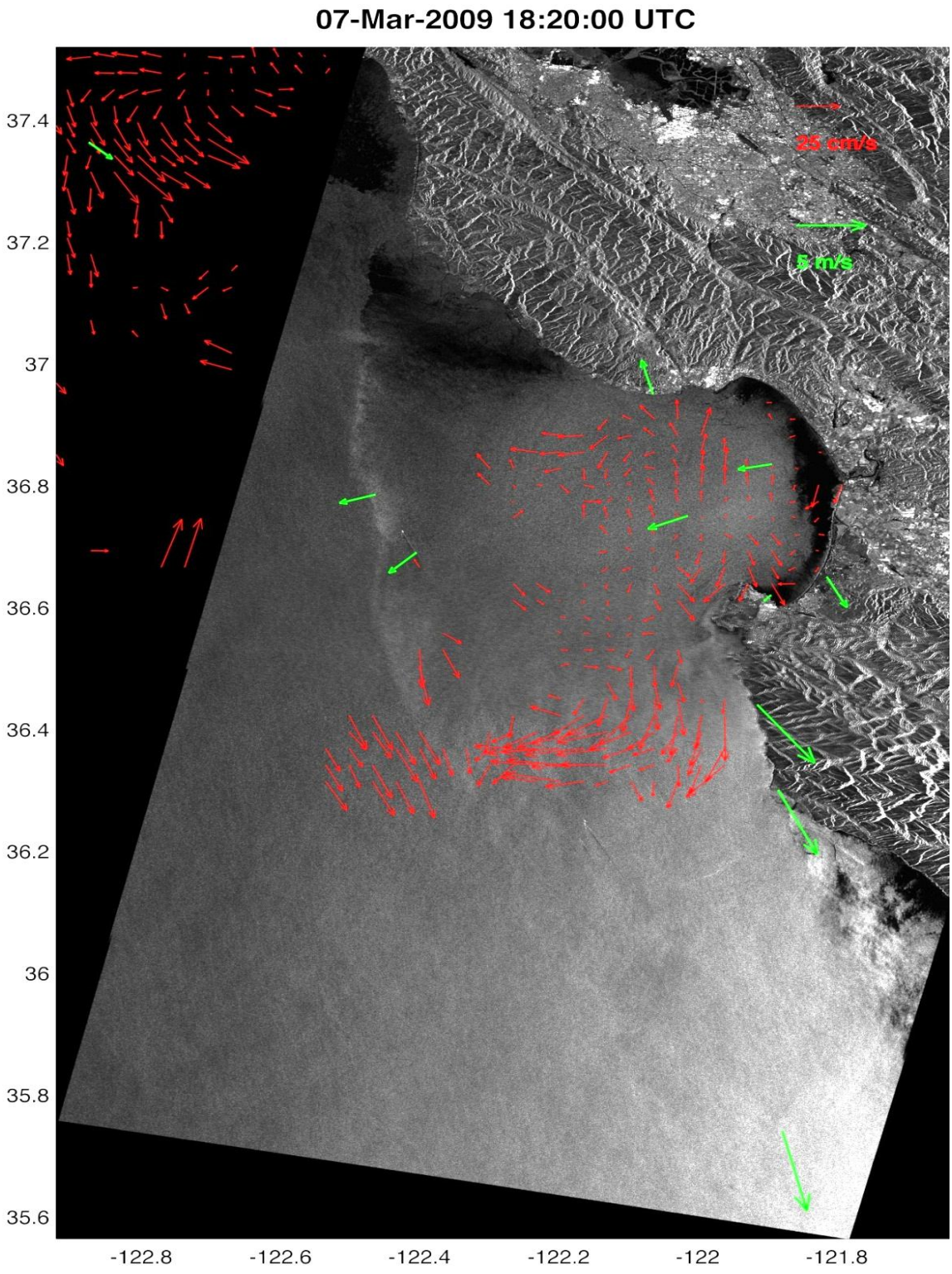

Figure 74. SAR image from 7 March 2009 at 1820 UTC and HF radar currents (red) and surface winds (green) from the closest hour (SAR data provided by ESA).

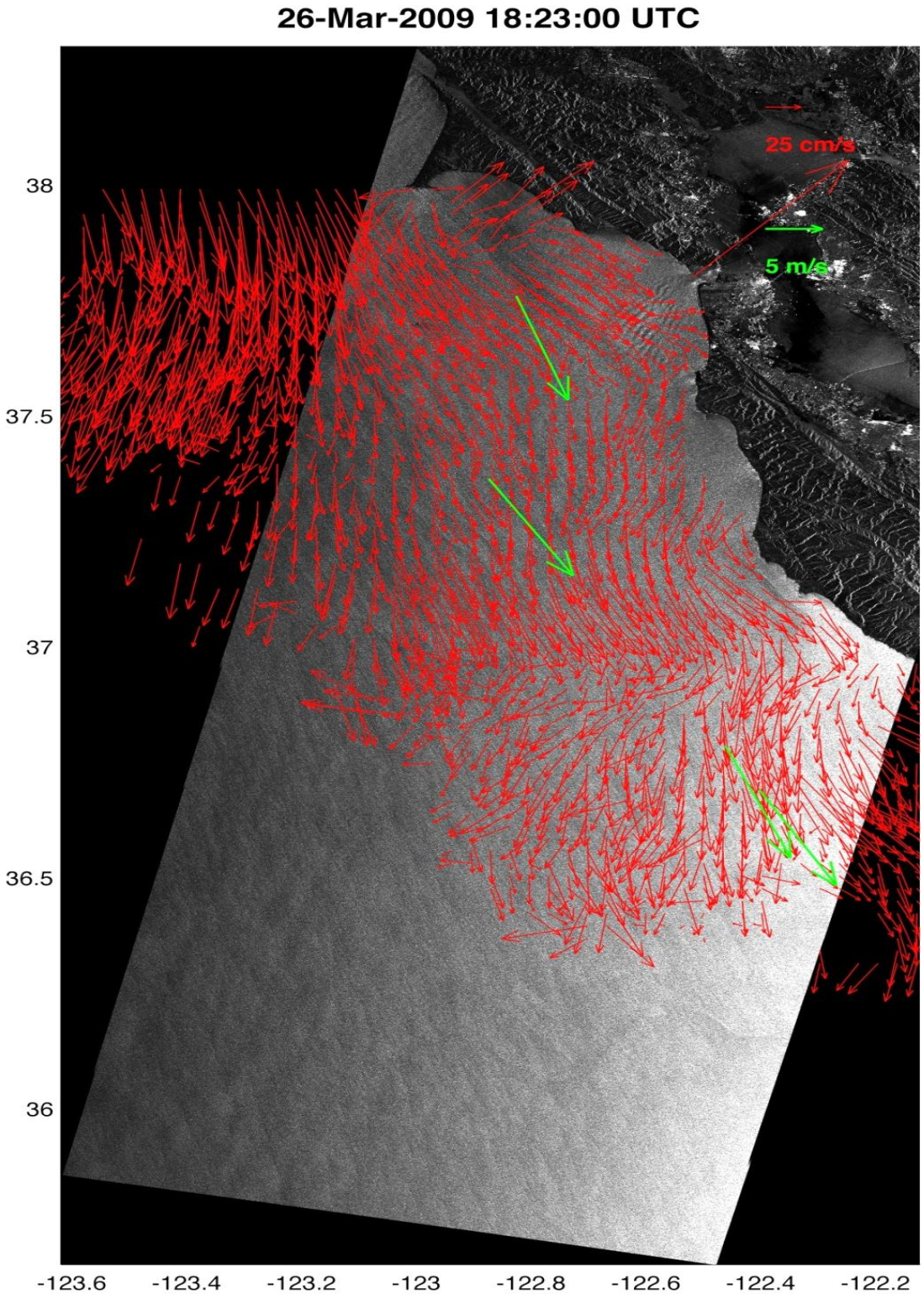

Figure 75. SAR image from 26 March 2009 at 1823 UTC and HF radar currents (red) and surface winds (green) from the closest hour (SAR data provided by ESA).

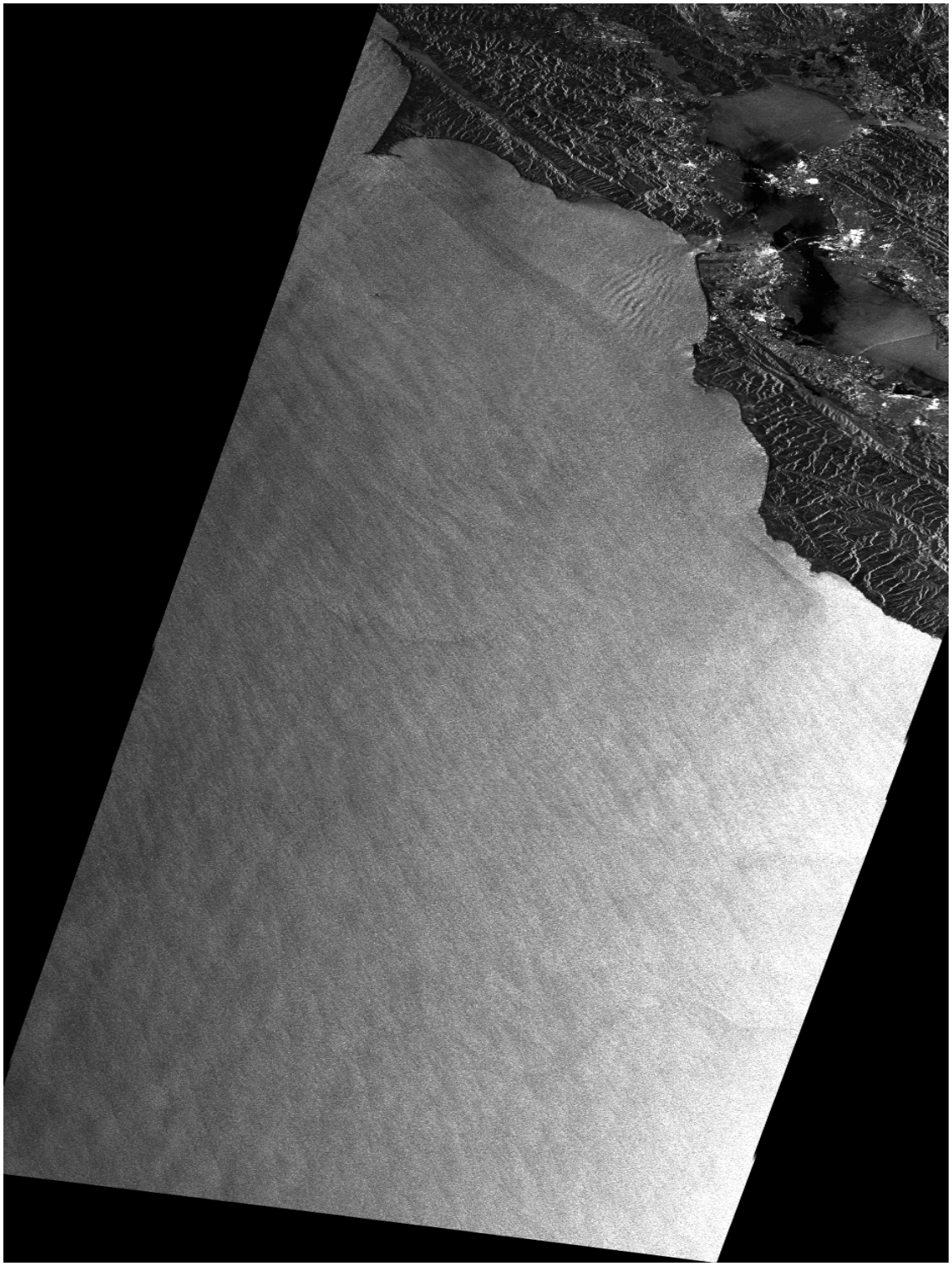

Figure 76. SAR image from 26 March 2009 at 1823 UTC (SAR data provided by ESA).

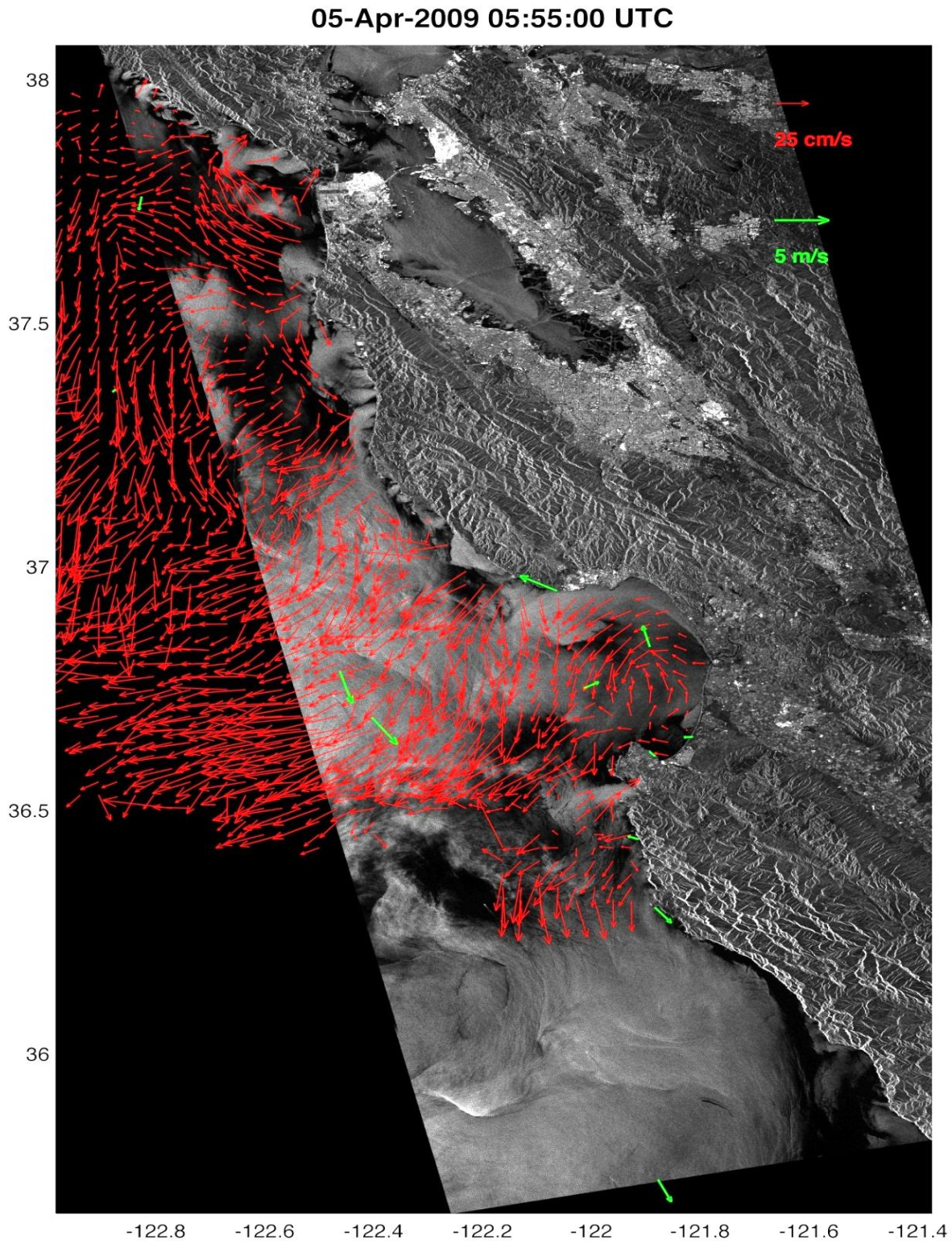

Figure 77. SAR image from 5 April 2009 at 0555 UTC and HF radar currents (red) and surface winds (green) from the closest hour (SAR data provided by ESA).

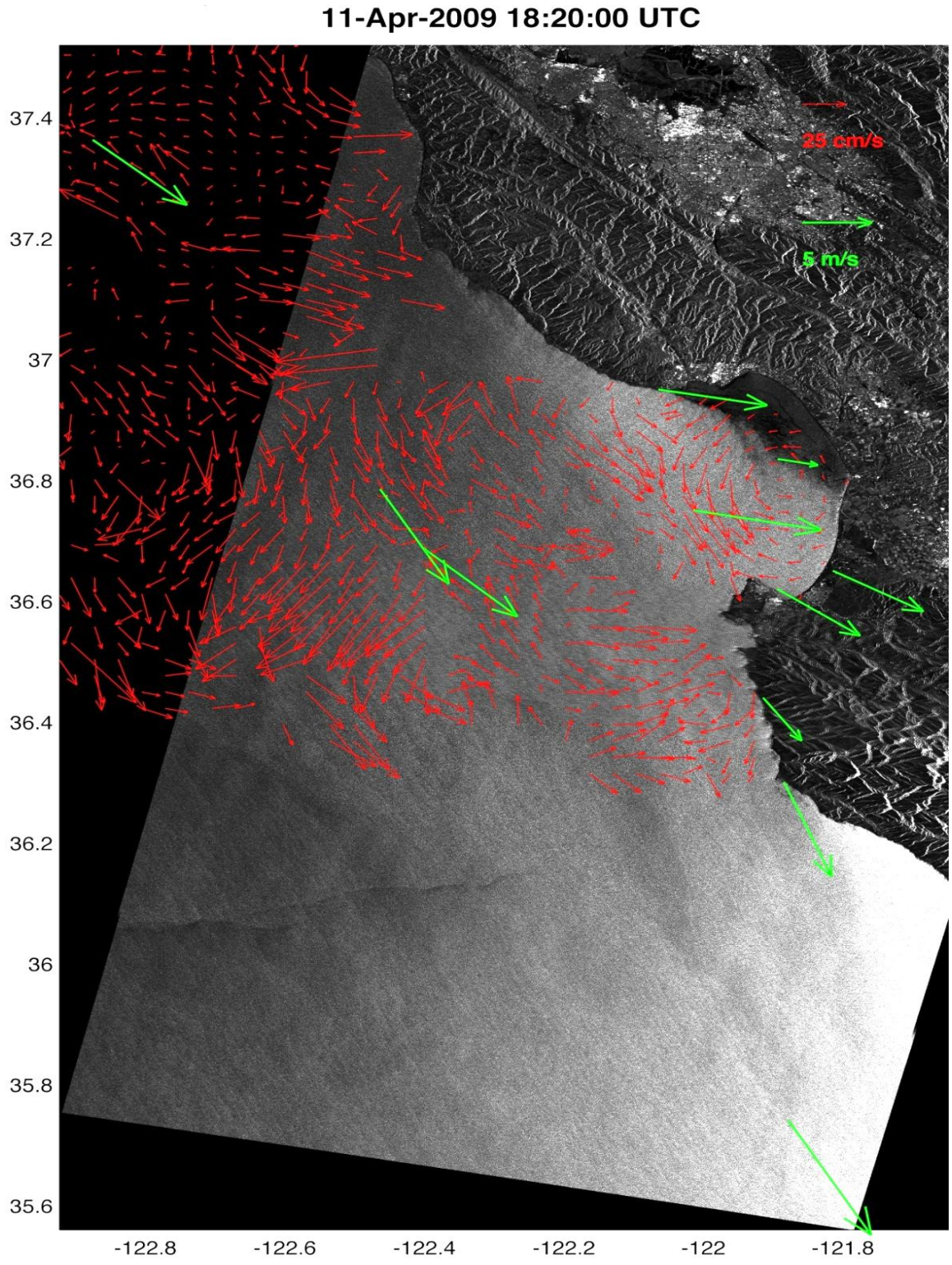

Figure 78. SAR image from 11 April 2009 at 1820 UTC and HF radar currents (red) and surface winds (green) from the closest hour (SAR data provided by ESA).

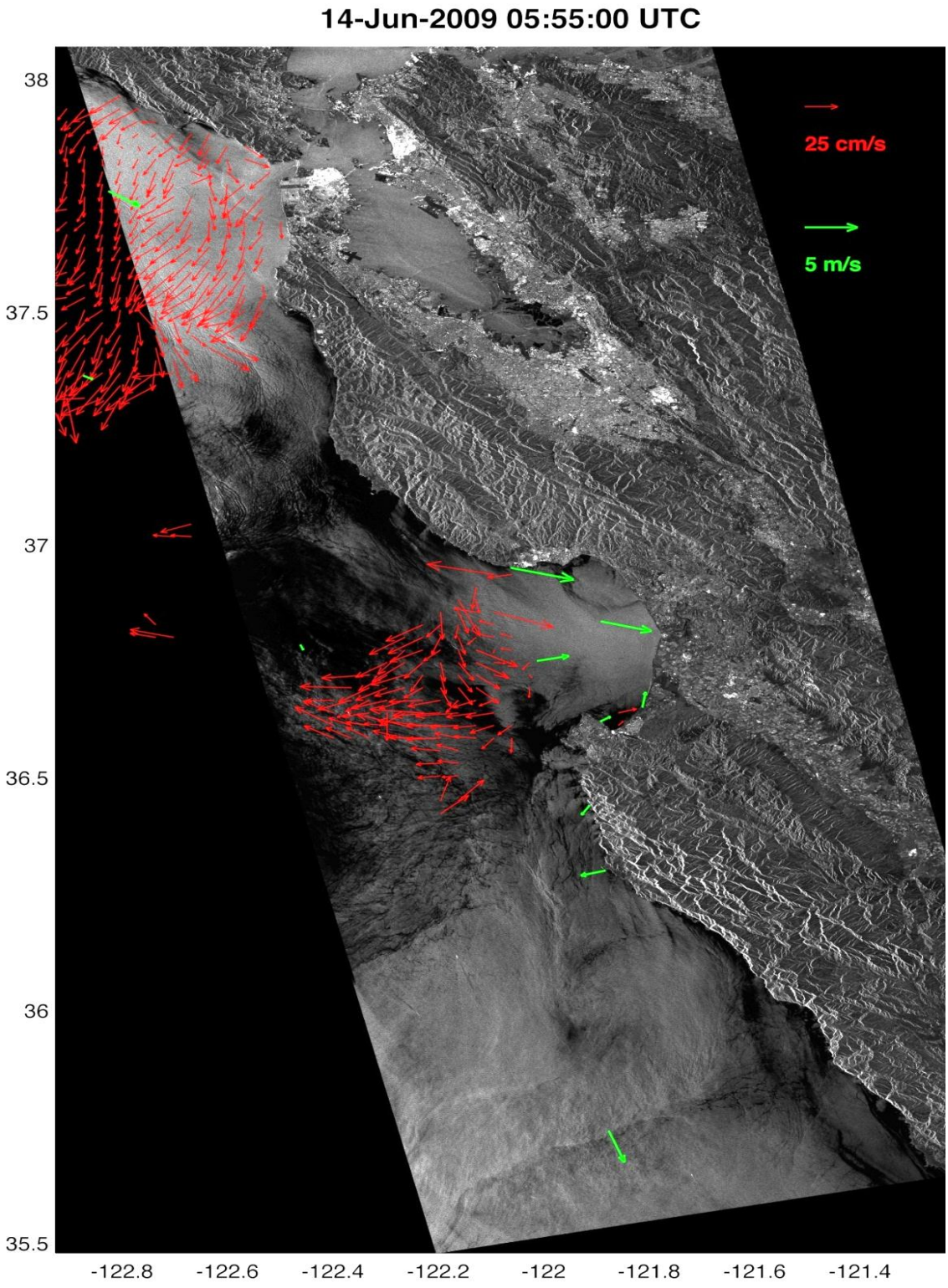

Figure 79. SAR image from 14 June 2009 at 0555 UTC and HF radar currents (red) and surface winds (green) from the closest hour (SAR data provided by ESA).

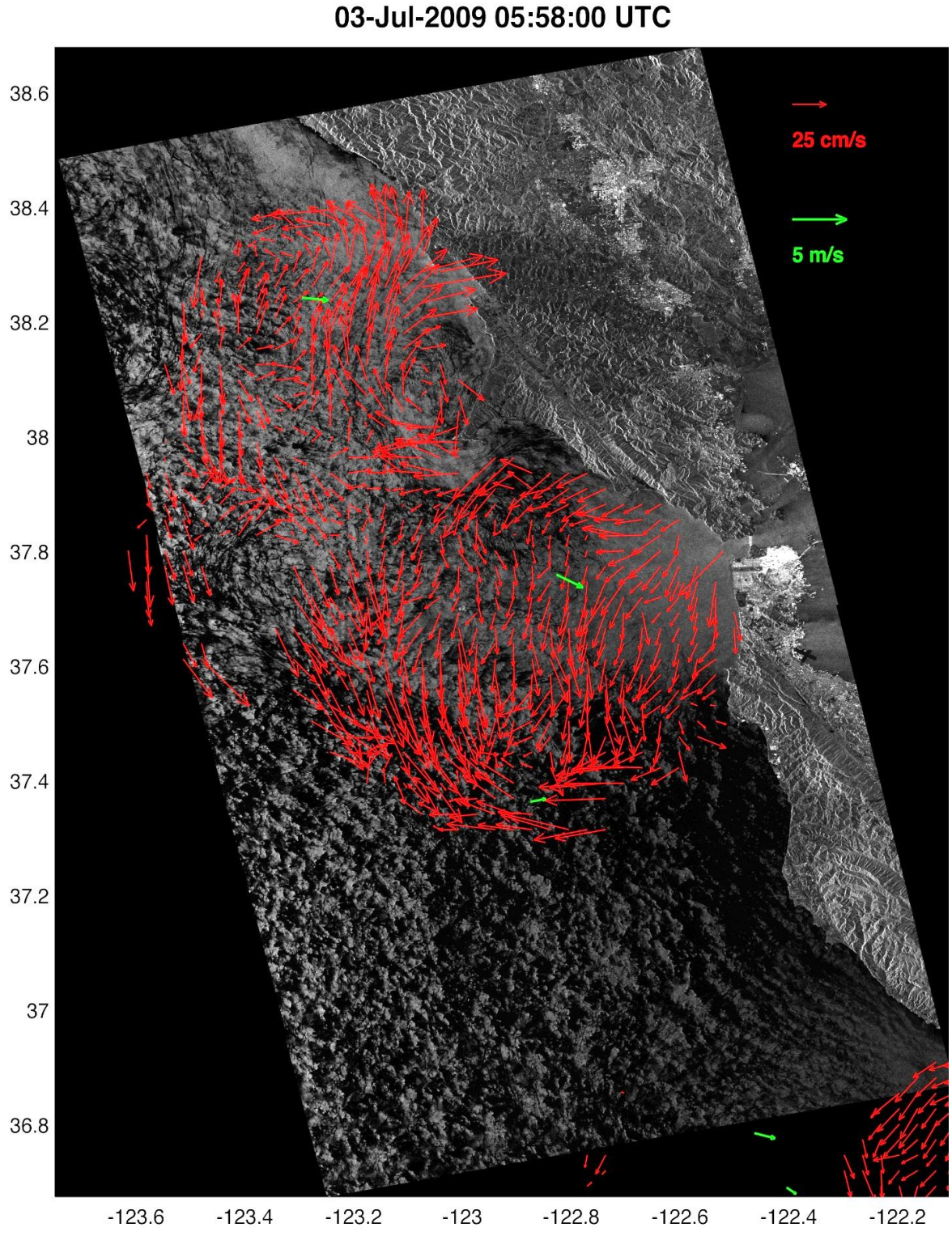

Figure 80. SAR image from 3 July 2009 at 0558 UTC and HF radar currents (red) and surface winds (green) from the closest hour (SAR data provided by ESA).

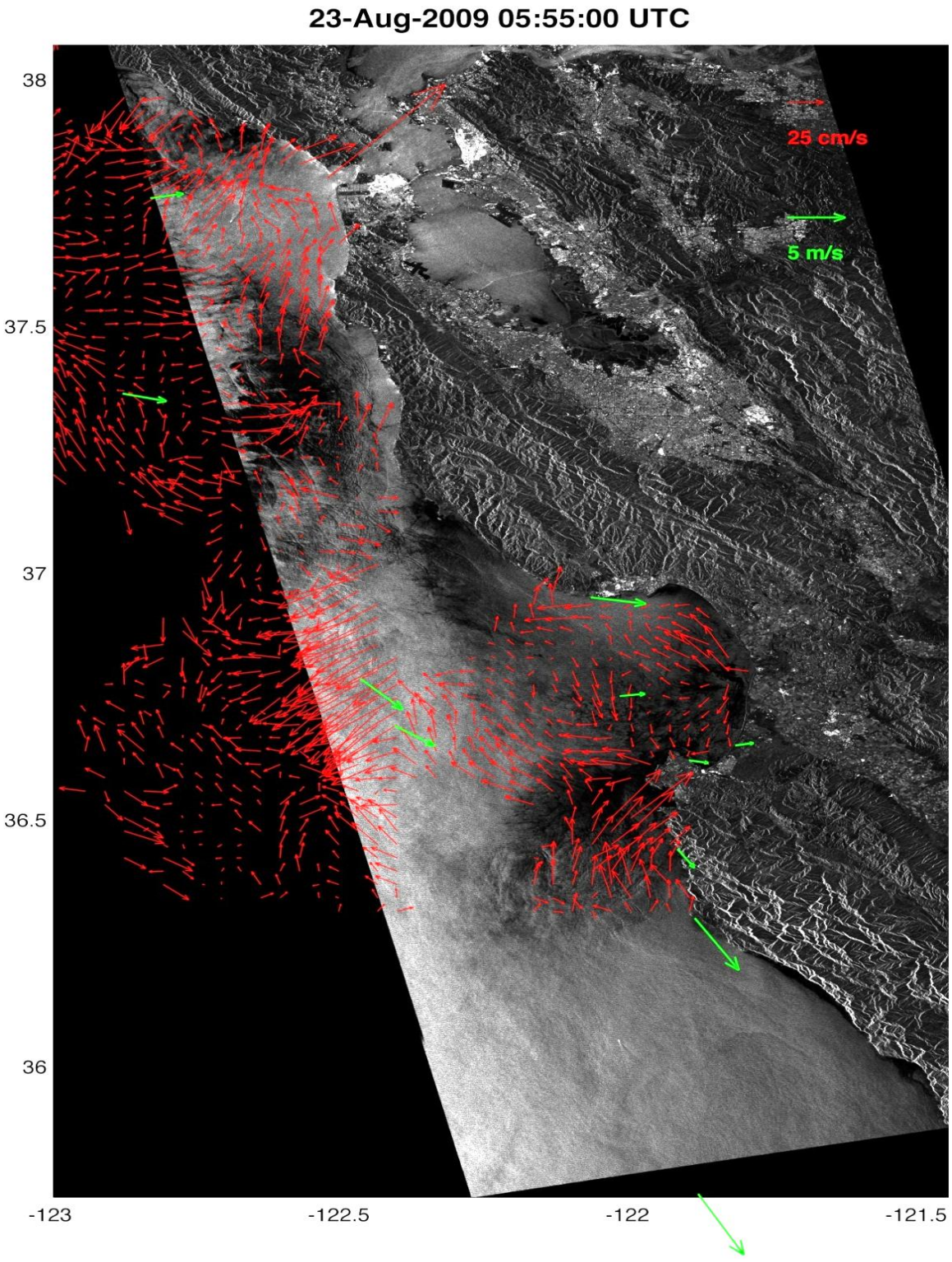

Figure 81. SAR image from 23 August 2009 at 0555 UTC and HF radar currents (red) and surface winds (green) from the closest hour (SAR data provided by ESA).

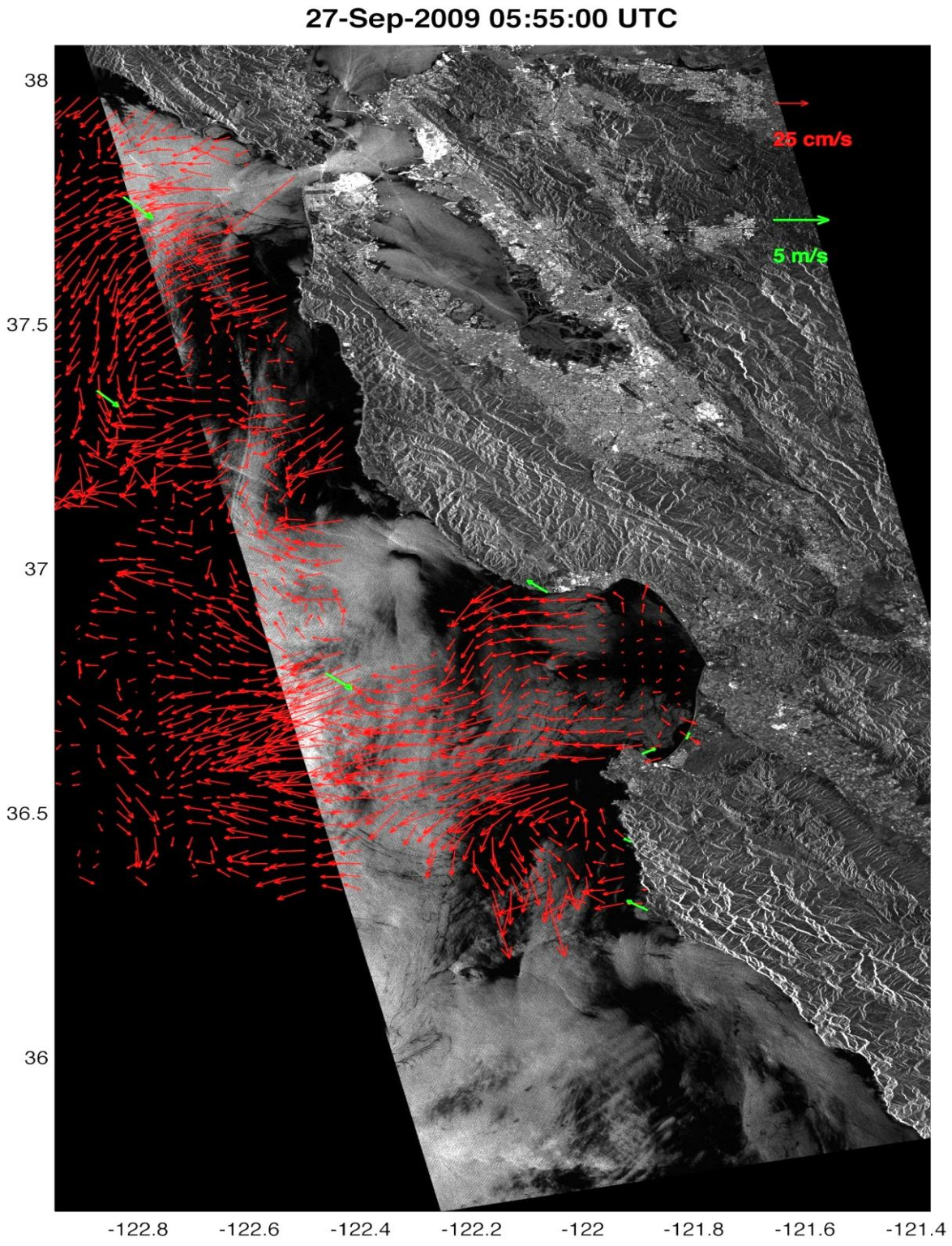

Figure 82. SAR image from 27 September 2009 at 0555UTC and HF radar currents (red) and surface winds (green) from the closest hour (SAR data provided by ESA).

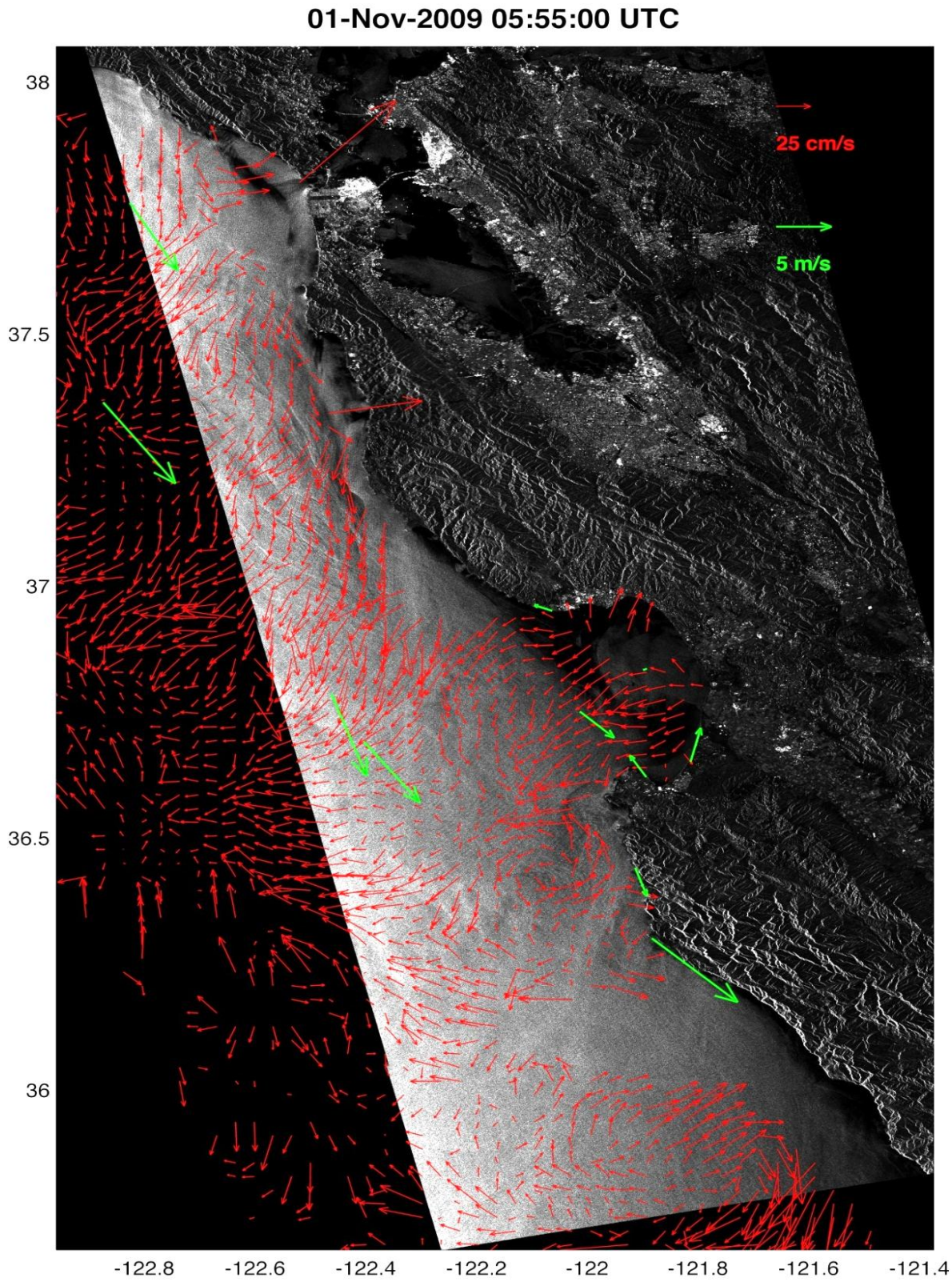

Figure 83. SAR image from 1 November 2009 at 0555 UTC and HF radar currents (red) and surface winds (green) from the closest hour (SAR data provided by ESA).

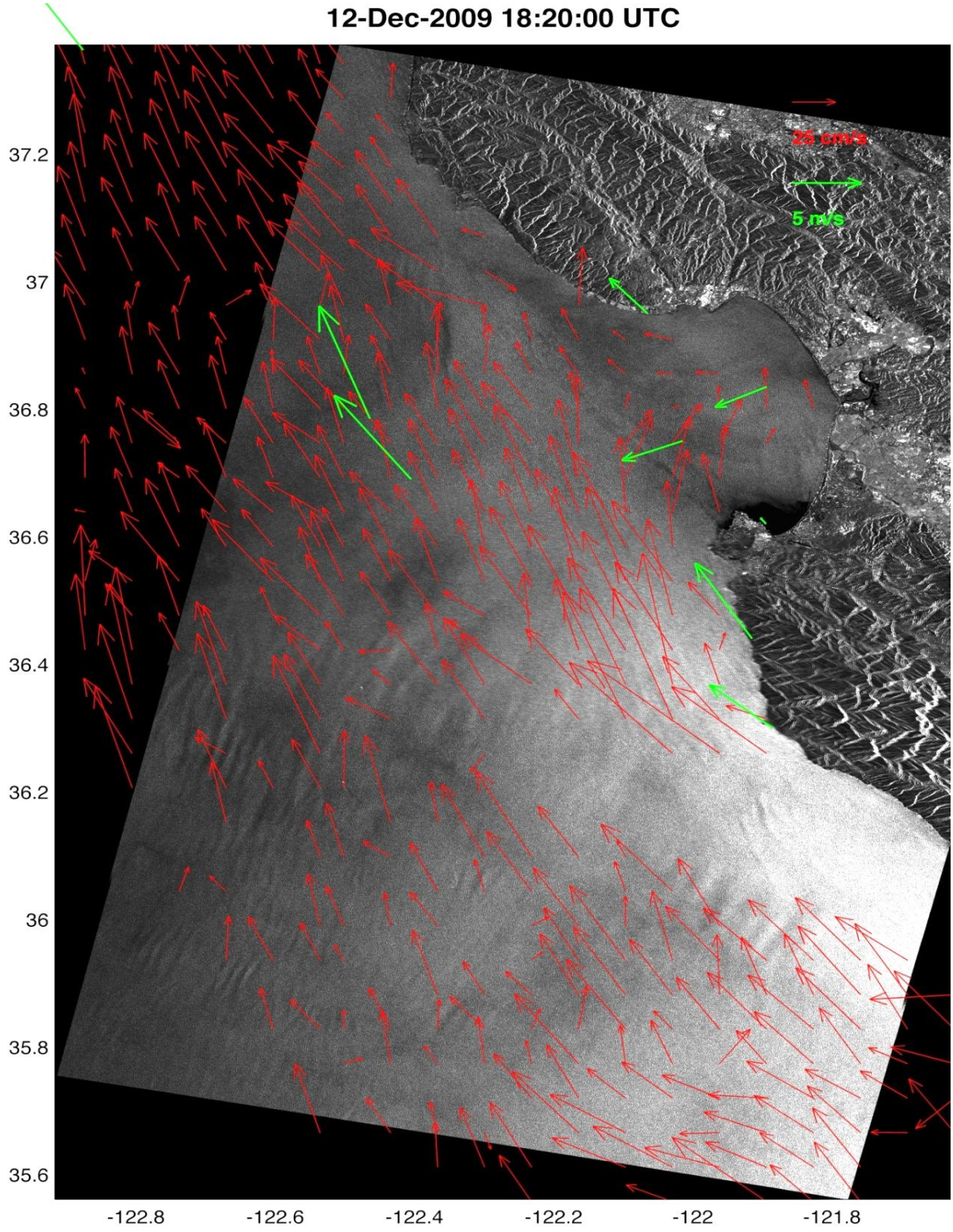

Figure 84. SAR image from 12 December 2009 at 1820 UTC and HF radar currents (red) and surface winds (green) from the closest hour (SAR data provided by ESA).

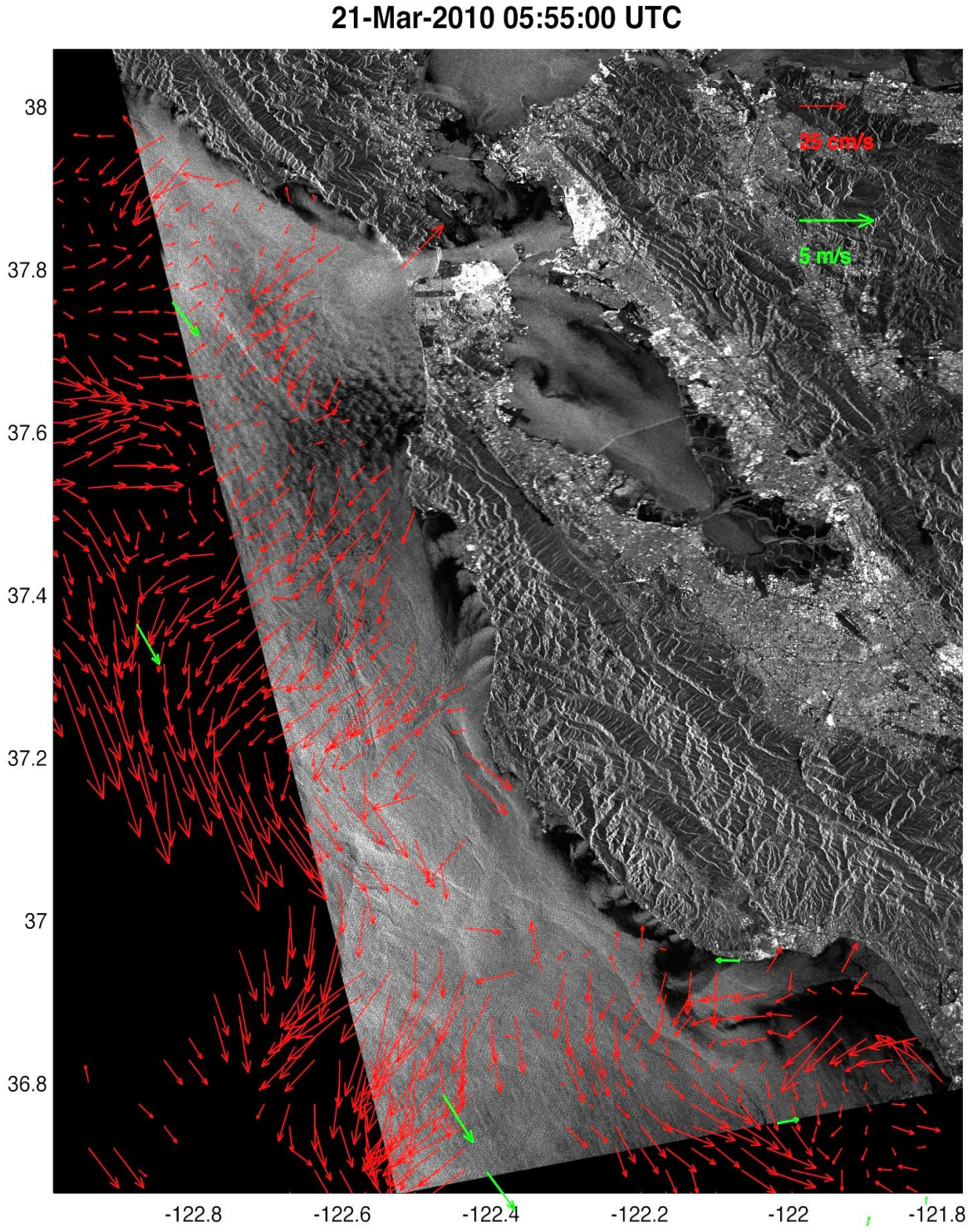

Figure 85. SAR image from 21 March 2010 at 0555 UTC and HF radar currents (red) and surface winds (green) from the closest hour (SAR data provided by ESA).

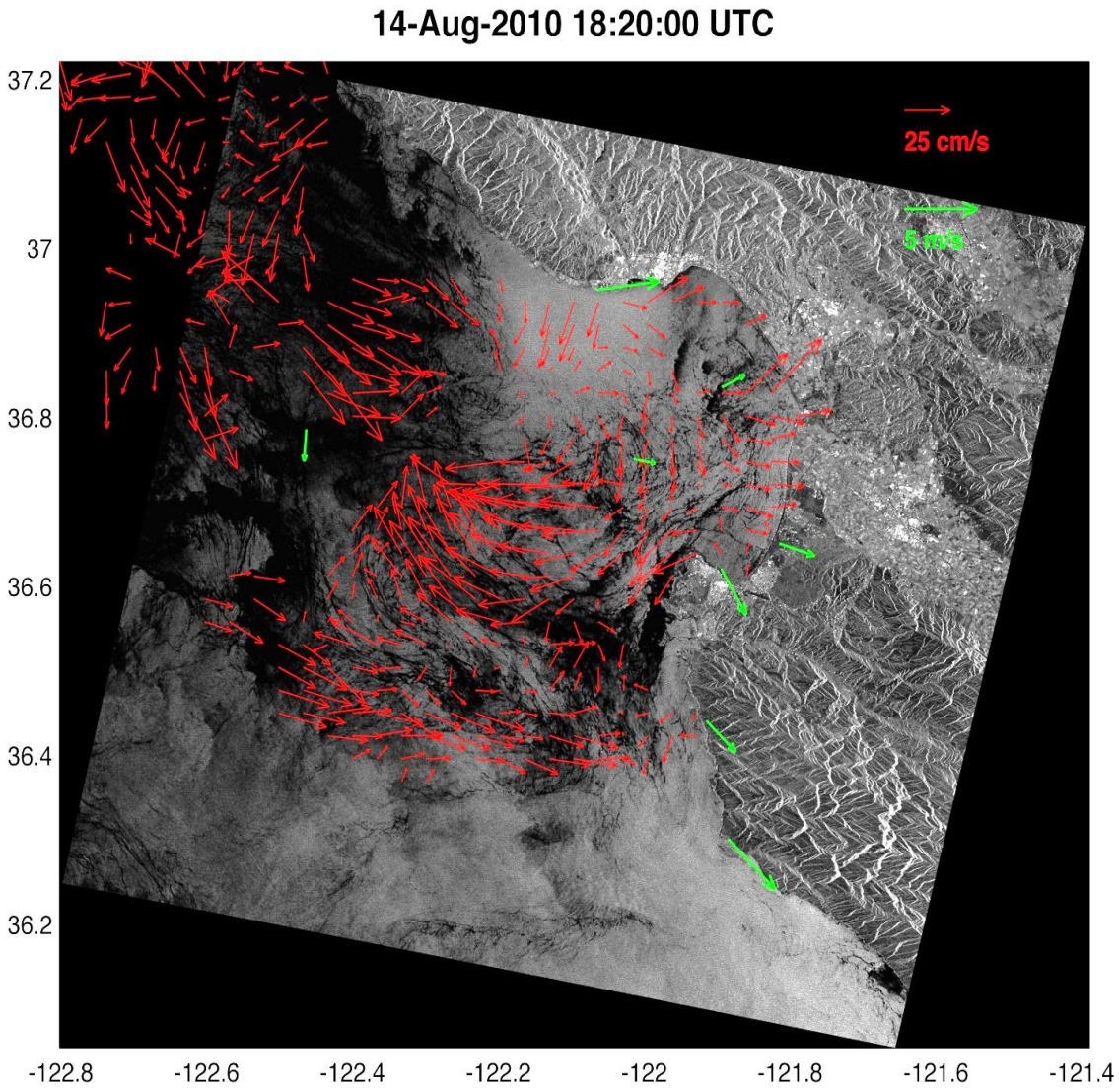

Figure 86. SAR image from 14 August 2010 at 1820 UTC and HF radar currents (red) and surface winds (green) from the closest hour (SAR data provided by ESA).

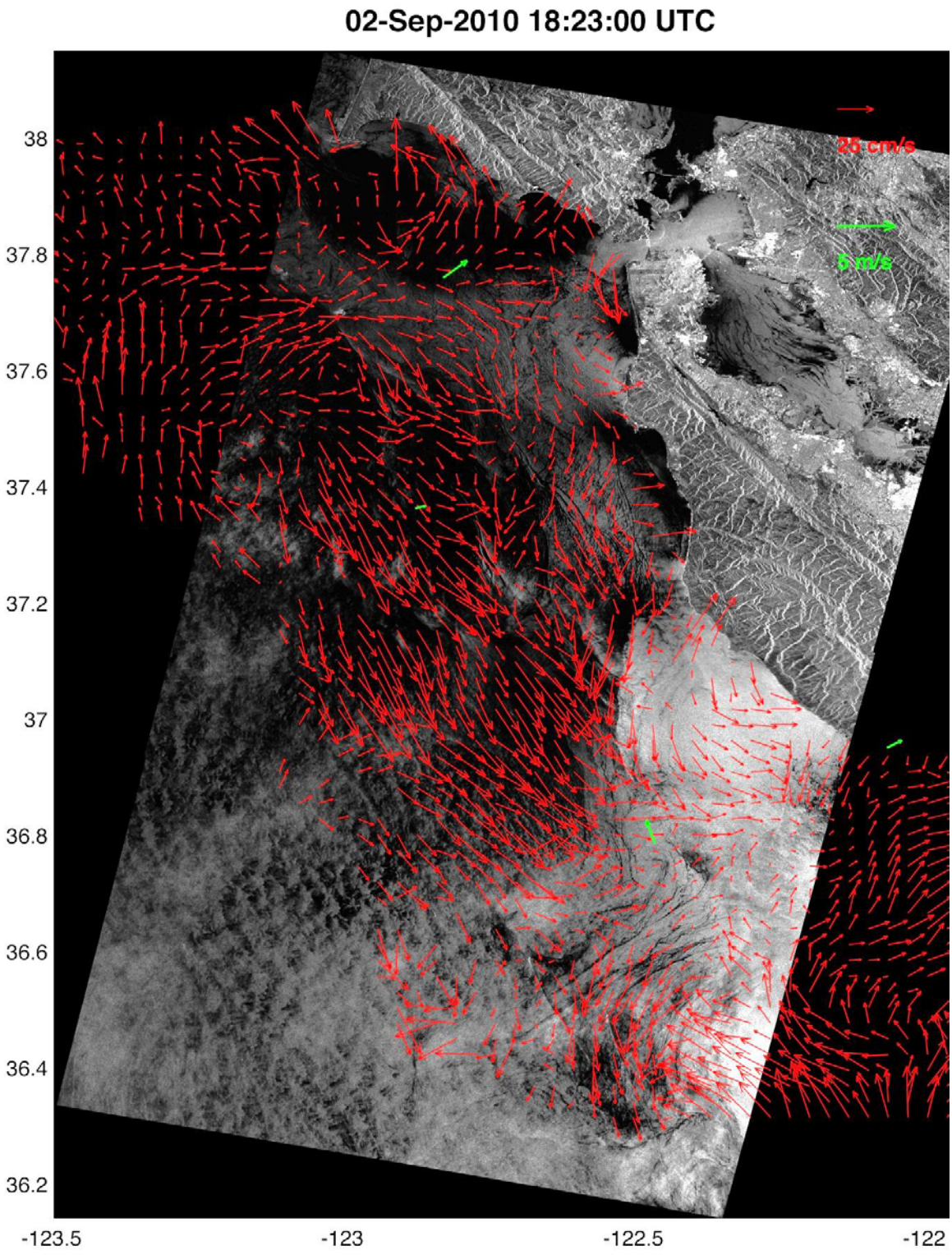

Figure 87. SAR image from 2 September 2010 at 1823 UTC and HF radar currents (red) and surface winds (green) from the closest hour (SAR data provided by ESA).

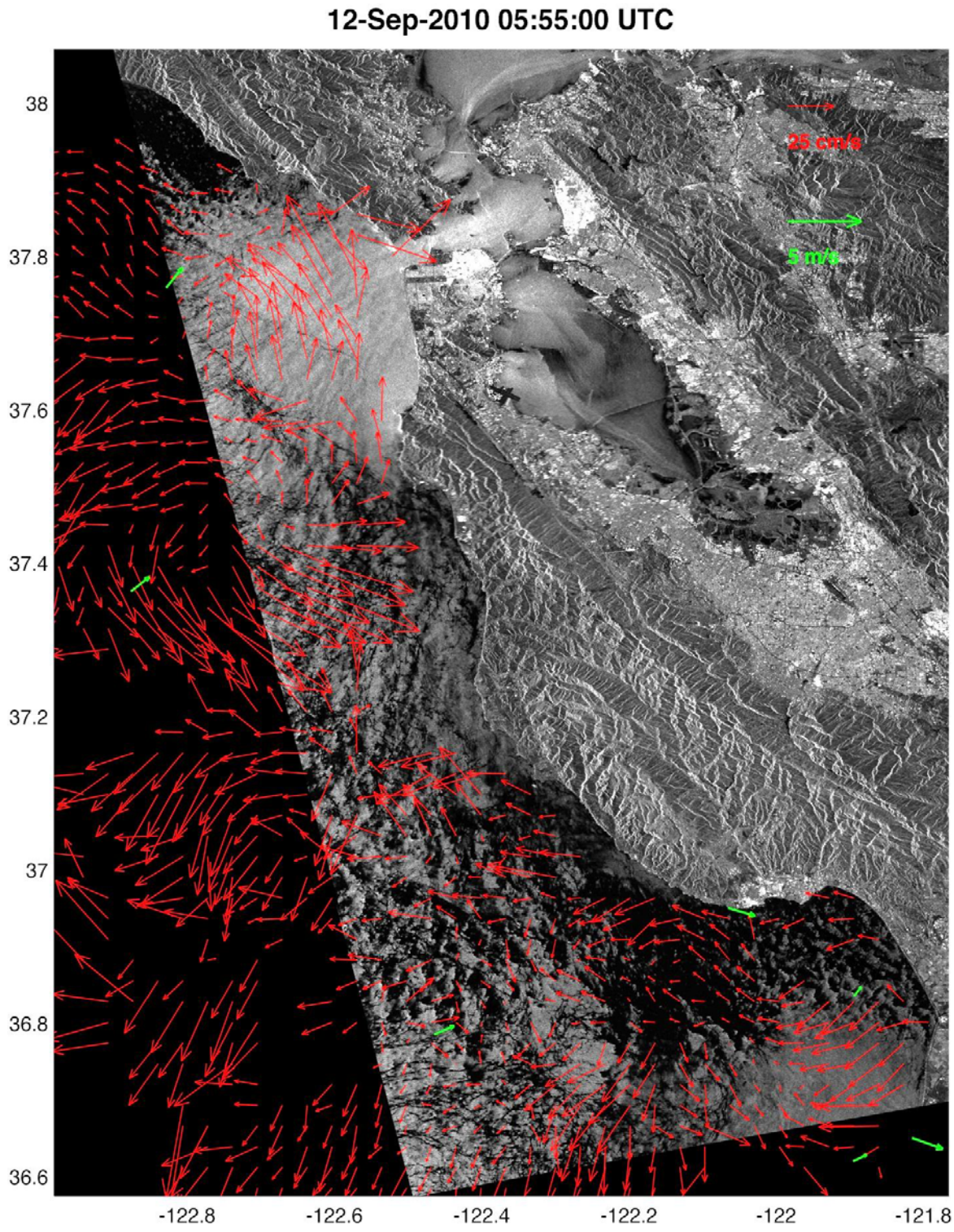

Figure 88. SAR image from 12 September 2010 at 0555 UTC and HF radar currents (red) and surface winds (green) from the closest hour (SAR data provided by ESA).

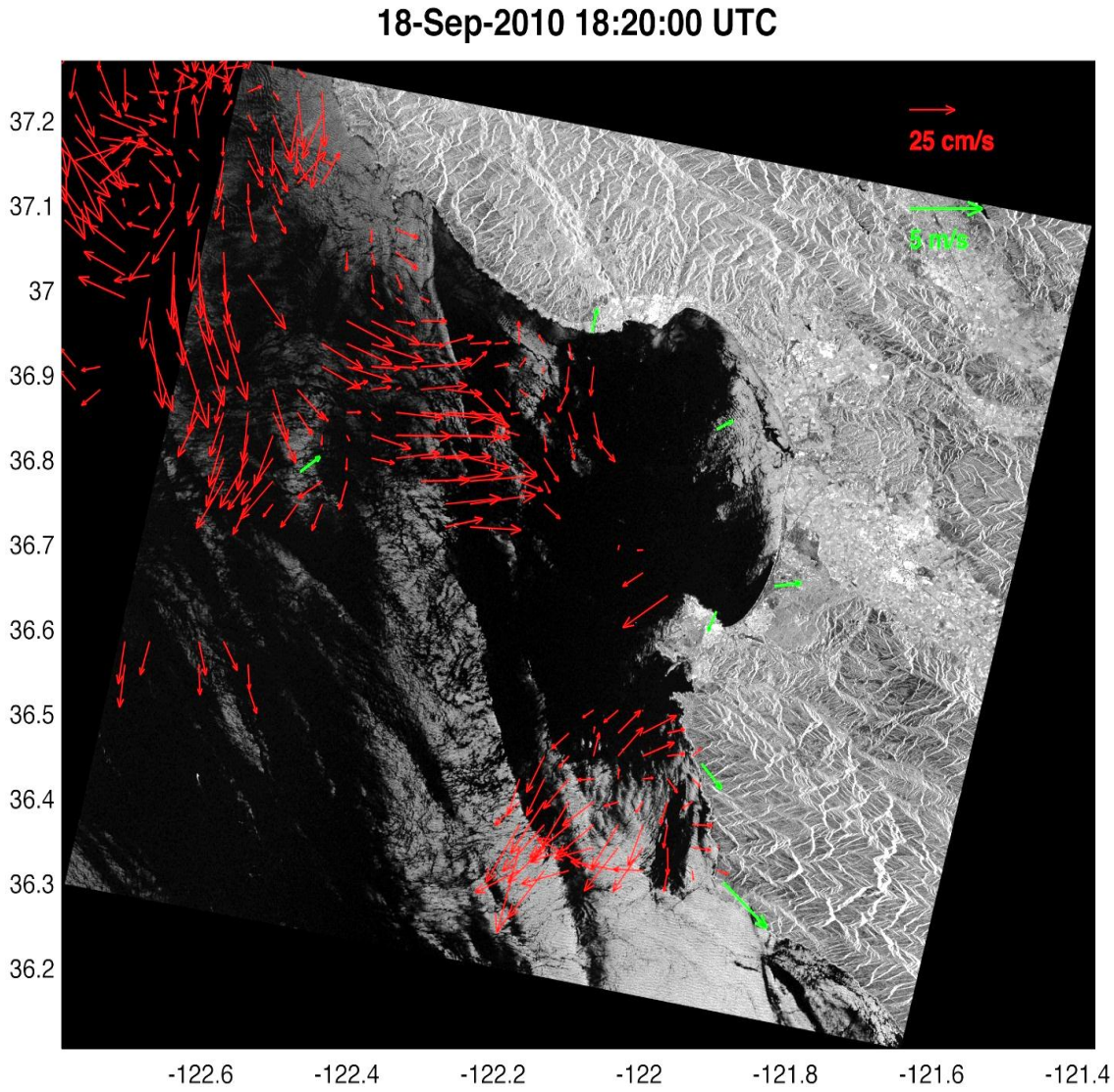

Figure 89. SAR image from 18 September 2010 at 1820 UTC and HF radar currents (red) and surface winds (green) from the closest hour (SAR data provided by ESA).

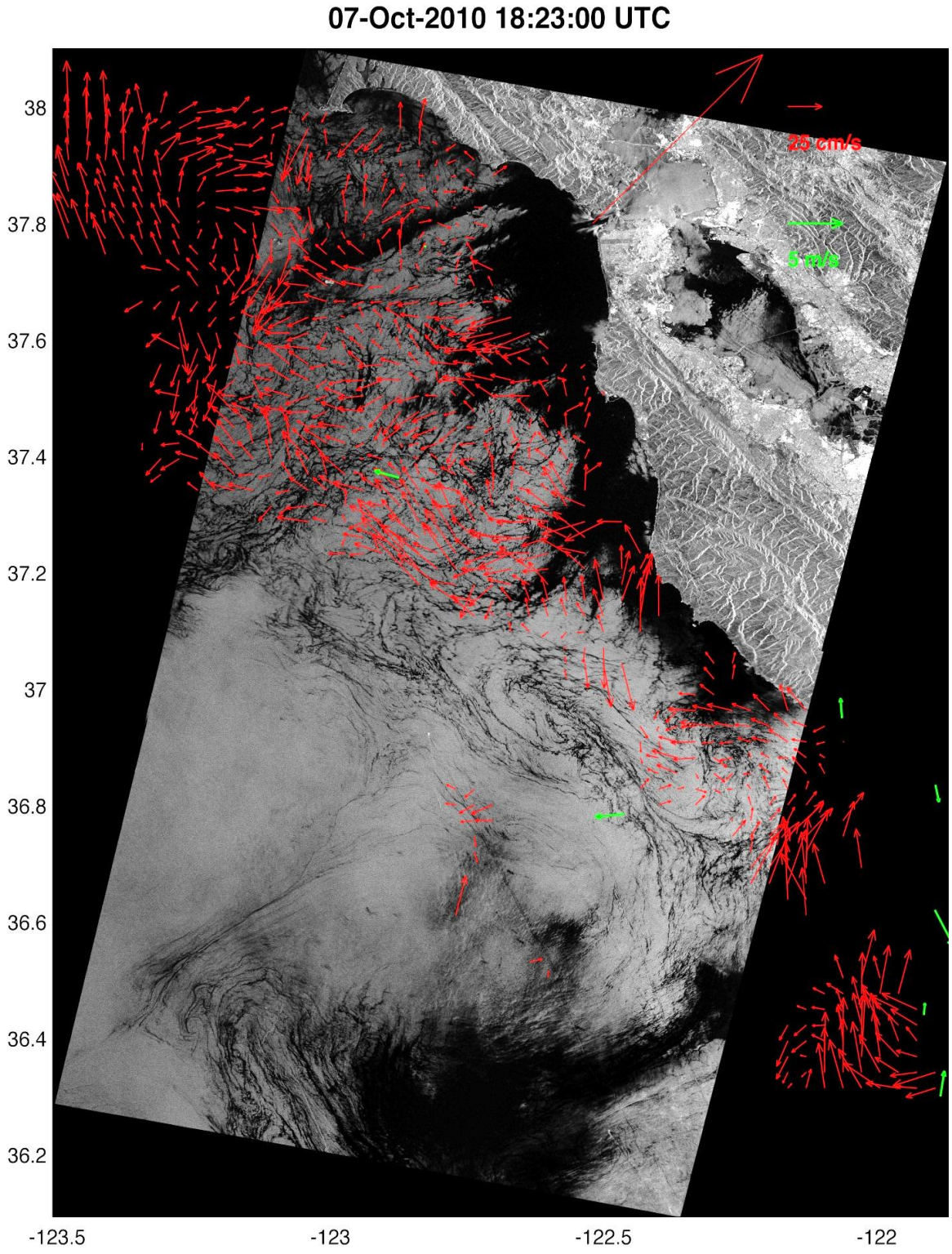

Figure 90. SAR image from 7 October 2010 at 1823 UTC and HF radar currents (red) and surface winds (green) from the closest hour (SAR data provided by ESA).

THIS PAGE INTENTIONALLY LEFT BLANK

APPENDIX B

Appendix B contains notes on possible features in the individual SAR images presented in Appendix A.

Supplementary images are maintained online by NPS. The link to access these documents is: http://calhoun.nps.edu/

Figure 58 21-Jul-07 18:20:00

1-Strong winds mask the oceanic features. A NNE-SSW-aligned dark band in Monterey Bay is located near a current convergence zone perceived by HF radar.
2-Atmospheric gravity waves are seen offshore with an N-S orientation, aligned 50° with wind.

Figure 59 25-Aug-07 18:20:00

1- A small cyclonic feature south of Pigeon Point can be seen in HF radar currents and imaged by SAR through surfactants.
2-In Monterey Bay, a convergence zone appears in HF radar currents, but there's not enough wind to generate capillary waves to image a feature on SAR.
3- Offshore of Carmel, a dark filament stretches from coast to offshore, captured in the SAR image as a lower backscatter region due to accumulation of surfactants.
4-In the lower part of the SAR image is an interesting frontal pattern that might be associated with surface flow. Note the slicks orientation and their curvature.

Figure 60 23-Sep-07 5:55:00

1- The HF radar currents indicate the presence of a vortical feature in Monterey bay, which is not depicted by SAR. In the north part of the Bay, closer to Santa Cruz, the HF vectors converge seaward and perpendicular to the most significant slicks pattern.
2-In the Half Moon Bay region, a packet of internal waves progresses shoreward, bending in agreement with the bathymetry (see Example 4 in Chapter IV). The HF radar, higher-intensive current vectors are located near the center of the concave internal wave structure.

Figure 61 3-Nov-07 18:20:00

1-A gap flow wind reversal pattern leaves Monterey Bay, from ENE, where the brighter strikes seen in the Bay indicate higher wind stress.
2- Close to Point Sur is evidence of a cyclonic eddy imaged by surfactants with a very low wind condition. This feature, shown in Figure 62, appears more obvious in regions where the surface roughness is higher, consequent of stronger winds.

Figure 63 10-Feb-08 5:55:00

See Example 8 in Chapter IV.

Figure 64 16-Feb-08 18:20:00

1- The corresponding MODIS True Color image taken at 2118 UTC (see NRL website (http://www7240.nrlssc.navy.mil/browse/lvl3/hmodis/Monterey250/2008/feb/aqua.2008047.0216.211500.D.L3.hmodis.MNT.v08.250m.true_color.png) shows oceanic optical features.
2- A wind gap flow pattern in Monterey Bay is detected by MBARI M0 and M1 buoys and seen in the SAR image as brighter surface.

Figure 65 15-May-08 18:23:00

1 – Southwest of Pigeon Point is an anti-cyclonic meander. In the bottom part of this feature, the orientation of the slicks tends to agree with the HF radar current field. A closer look at nearby ship wakes adds to the understanding of the surface flow.
2- The Farallon Islands produce a wake in the wind direction (WNW), which is visible on the SAR image.
3- In the San Francisco area is a gap flow, in which the shore station FTPC1 (http://www.ndbc.noaa.gov/station_page.php?station=FTPC1) measures the wind from ENE, whereas the buoy station 46026 (http://www.ndbc.noaa.gov/station_page.php?station=46026) measures the wind from the western quadrant. The opposing winds might indicate the presence of a shoreward front associated with roughness on the sea surface level. We propose that the edge of the frontal system is captured in the SAR image as a brighter strip with north-south alignment just east of the buoy station (green vector).

Figure 66 25-May-08 5:55:00

See Example 7 in Chapter IV.

Figure 67 13-Jun-08 5:58:00

1- A large wind front occupies almost the entire image. On the left side of the boundary is some backscatter at -15 to -20 db, whereas on the right side of the front is more backscatter around -5db to -10db.
2- HF radar surface currents detect an anti-cyclonic eddy offshore of Pigeon Point but this feature is masked in the SAR image.
3- Offshore of Half Moon Bay is a brighter signature with no apparent connection to the HF currents.
4- West of Point Reyes is brighter band where HF surface currents indicate an outward converging flow.
5- Atmospheric gravity waves with ~1.5km wavelength are depicted north of Point Reyes.

Figure 68 5-Jul-08 18:20:00

See Example 1 in Chapter IV, which contains lower-density, HF-radar surface currents overlapped.

Figure 69 28-Aug-08 18:23:00

See Example 2 in Chapter IV.

Figure 70 7-Sep-08 5:55:00

See Example 3 in Chapter IV.

Figure 71 13-Sep-08 18:20:00

1- A low wind condition, less than 1.5m/s in most of the image, does not create sufficient roughness to be sensed by SAR.
2- In Monterey Bay, HF-radar surface currents detect a cyclonic eddy which is slightly depicted by surfactants in the SAR image.

Figure 72 18-Oct-08 18:20:00

The SAR image describes a complicated surface pattern with little correlation to the hourly-averaged HF currents. The flow exhibits meandering circulation. The white circle indicates a possible cyclonic eddy around a brighter core.

Figure 73 1-Mar-09 5:55:00

1- See Example 4 in Chapter IV.
2- Besides the features previously discussed in Chapter IV, the SAR image detects a wind front in Monterey Bay. *In situ* measurements reveal a wind gradient in total agreement with the SAR image.

Figure 74 7-Mar-09 18:20:00

1- The SAR image shows a front parallel to the coast from Pigeon Point to south of Point Sur. HF-vectors don't provide enough information to assess the surface currents' influence on this feature.
2- On the Monterey Bay shoreline, the SAR image depicts a wind-shadow effect due to land sheltering by onshore winds. The differences in backscatter in this region are 15db.

Figure 75 26-Mar-09 18:23:00

1- The previous 10 days evidence very strong winds blowing from the NW quadrant, creating conditions for the occurrence of upwelling. An SST map from 27 March 2009 at 2140UTC

(http://www7240.nrlssc.navy.mil/browse/lvl3/modis/NorthEastPacific/2009/mar/aqua.2009086.0327.D.L3_Mosaic.modis.NEP.v07.1000m.sst.png) demonstrates this assumption.
2- The flow pattern is intense and in the same direction as the local wind. In Monterey Bay, buoys and shore stations measure moderate winds, and HF currents are less intense.
3- South of Pigeon Point is a strong seaward jet. In the same region, the SAR image detects a slightly darker band (See Figure 76).
4- Other indications of wind strength close to the San Francisco area features such as wakes from both Point Reyes Cape and the Farallones and surface gravity waves with ~1.5km wavelength (See Figure 76).

Figure 77 5-Apr-09 5:55:00

1- In Monterey Bay, A cyclonic feature is visible in SAR and HF surface currents. Two seaward filaments can be seen in both the north and south part of the Bay by way of convergence in HF currents and brighter bands in the SAR image.
2- Offshore of Año Nuevo Bay is an anti-cyclonic, vortical feature depicted by SAR and HF currents.
3 – West of Point Su is an interesting ship wake in a dark region in the SAR image. The ship's movement breaks the smooth surface where the wind is weak.

Figure 78 11-Apr-09 18:20:00

1- A cyclonic eddy is seen in HF currents in Monterey Bay. The SAR image exhibits a more intense backscatter in this area.
2- In the north part of Monterey Bay, the SAR image reveals a wind-shadowing effect.
3- West of Santa Cruz, SAR depicts atmospheric gravity waves of ~ 4 km wavelength.

Figure 79 14-Jun-09 5:55:00

1- A bathymetric dispersion of a seaward plume is displayed in San Francisco. The image was captured a few minutes after ebb tide. A similar feature is also seen in Figure A15.
2- Offshore of the Half Moon Bay and Pigeon Point areas, SAR detects bottom-induced features, including packets of internal waves, mostly dispersing parallel to the bathymetry.
3- Regions with relatively low winds speed allows the visualization of long ship wakes of around 50km.

Figure 80 3-Jul-09 5:58:00

1- In the Point Reyes area, visible vortical features visible are imaged by surfactants in SAR and captured by HF radar. The slicks are parallel to the surface currents
2- The rest of the SAR image exhibits very weak winds, thus creating little surface roughness.

Figure 81 23-Aug-09 5:55:00

1- In San Francisco is a bathymetric dispersion of a seaward plume. The tide is 3 hours after the ebb cycle. A similar feature is also seen in Figure A15.
2- Offshore of the Half Moon Bay and Pigeon Point areas, SAR detects bottom-induced features, including packets of internal waves, mostly dispersing parallel to the bathymetry.
3- Offshore of Monterey Bay, a convergence zone is seen in HF surface currents corresponding to a brighter band in the SAR image.

Figure 82 27-Sep-09 5:55:00

See Example 9 in Chapter IV.

Figure 83 1-Nov-09 5:55:00

1- In the San Francisco area, a brighter band presumably corresponds to a temperature gradient. The flood cycle is almost complete. According to the 8hr-prior SST http://www7240.nrlssc.navy.mil/browse/lvl3/modis/NorthEastPacific/2009/oct/aqua.2009304.1031.D.L3_Mosaic.modis.NEP.v08.1000m.sst.png and 15hr-subsequent SST http://www7240.nrlssc.navy.mil/browse/lvl3/modis/NorthEastPacific/2009/nov/aqua.20093051101.212000.D.L3.modis.NEP.v08.1000m.sst.png maps, offshore colder water and inshore warmer water masses are approximately in the same location.
2- Offshore of the Half Moon Bay and Pigeon Point areas, SAR detects bottom-induced features, including packets of internal waves, mostly dispersing parallel to the bathymetry.

Figure 84 12-Dec-09 18:20:00

1- The SAR image demonstrates strong winds and currents from the SE quadrant. Wind clutter masks ocean features and creates a homogeneous surface. The SST map, http://www7240.nrlssc.navy.mil/browse/lvl3/hmodis/Monterey250/2009/dec/aqua.2009346.1212.D.L3_Mosaic.hmodis.MNT.v08.250m.sst.png taken at 2115 UTC, shows a well-mixed surface temperature in the cloud-free ocean part offshore of Monterey.
2- The ship wakes are small, yet Point Pinos' wake extends for more than 40km along the bay in the direction of the wind.
3- Note the wind shadow in the south part of Monterey Bay as oppose to the usual shadowing at the north part of the Bay.
4- At the lower part of the image, one views atmospheric gravity waves with ~2km wavelength.

Figure 85 21-Mar-10 5:55:00

1- In San Francisco is a bathymetric dispersion of a seaward plume. The image was captured 2 hours after ebb tide. A similar feature is also seen in Figure A15.
2- Offshore of Half Moon Bay, SAR detects bottom-induced features, including packets of internal waves, mostly dispersing parallel to the bathymetry.

3- In Monterey Bay, HF currents evidence a cyclonic vortical structure. The SAR provides limited coverage of this feature.

Figure 86 14-Aug-10 18:20:00

See Example 5 in Chapter IV.

Figure 87 2-Sep-10 18:23:00

See Example 6 in Chapter IV.

Figure 88 12-Sep-10 5:55:00

1- Offshore of Half Moon Bay, a cyclonic eddy is retrieved by HF-radar currents. Limited SAR coverage of the area and low wind speed make difficult the visualization of the eddy.
2- In the San Francisco area, one can see atmospheric surface gravity waves of ~2km wavelength.
3- The rest of the SAR image exhibits very weak winds, thus creating little surface roughness.

Figure 89 18-Sep-10 18:20:00

MODIS SST and True Color images taken on 18 September 2010 at 2200 UTC http://www7240.nrlssc.navy.mil/browse/lvl3/hmodis/Monterey250/2010/sep/aqua.2010261.0918.220000.D.L3.hmodis.MNT.v08.250m.sst.png and http://www7240.nrlssc.navy.mil/browse/lvl3/hmodis/Monterey250/2010/sep/aqua.2010261.0918.220000.D.L3.hmodis.MNT.v08.250m.true_color.png show that temperature fronts and cloud pattern may be associated with SAR features.

Figure 90 7-Oct-10 18:23:00

See Example 3 in Chapter IV.

LIST OF REFERENCES

Apel, J.R., 2004. Oceanic Internal Waves and Solitons in *Synthetic Aperture Radar Marine User's Manual*. Jackson, C. R & Apel, J. R., eds, NOAA, NESDIS, Office of Research and Applications, Washington, DC. Available online at: http://www.sarusersmanual.com/ (accessed March, 2012).

Alpers, W. & Melsheimer, C., 2004. Rainfall in *Synthetic Aperture Radar Marine User's Manual*. Jackson, C. R & Apel, J. R., eds, NOAA, NESDIS, Office of Research and Applications, Washington, DC. Available online at: http://www.sarusersmanual.com/ (accessed March, 2012).

ASAR Users Guide. (n.d.). Retrieved from: http://envisat.esa.int/handbooks/ (accessed March, 2012)

Barrick, D., Evans, M., & Weber, B. (1977). Ocean surface currents mapped by radar. *Science*, 198, 138–144.

Canada Centre for Remote Sensing. (n.d.). *Educational resources for radar remote sensing* [Training slides toolkit]. Retrieved from http://www.nrcan.gc.ca/earth-sciences/geography-boundary/remote-sensing/radar-remote/1108 (accessed April, 2012)

Clemente-Colon, P., & Xiao-Hai Yan. (1999). Observations of east coast upwelling conditions in synthetic aperture radar imagery. *Geoscience and Remote Sensing, IEEE Transactions on*, 37(5), 2239-2248.

Chapman, R.D. & Graber, H.C. (1997). Validation of HF radar measurements. *Oceanography*, 10(2), 76–79.

Chapron, B., Collard, F. & Ardhuin, F. (2005). Direct measurements of ocean surface velocity from space: Interpretation and validation, *J. Geophys. Res.*, 110.

Collard, F., Ardhuin, F., & Chapron, B. (2005). Extraction of coastal ocean wave fields from SAR images. *Oceanic Engineering, IEEE Journal of*, 30(3), 526-533.

Chu, P. (n.d.), *Ocean Dynamics II (Waves & Instabilities)*, Naval Postgraduate School, Monterey,California.

Danilo, C., Chapron, B., Mouche, A., Garello, R. & Collard, F. (2007). Comparisons between HF radar and SAR current measurements in the Iroise sea. *OCEANS 2007 - Europe*, pp. 1–5.

DiGiacomo, P. M. & Holt, B. (2001). Satellite observations of small coastal ocean eddies in the Southern California Bight, *J. Geophys. Res.*, 106, 22,521–22,543

Freeman, A., Zlotnicki, V., Liu, T., Holt, B., Kwok, R., Yueh, S., Vazquez, J., Siegel, D. & Lagerloef, G., (2010). Ocean measurements from Space in 2025. *Oceanography*, 23(4), 144–161.

Fu, L.-L. & Holt, B. (1983). Some Examples of Detection of Oceanic Mesoscale Eddies by the SEASAT Synthetic-Aperture Radar, *J. Geophys. Res.*, 88(C3), 1844–1852.

Graber, H. C. & Heron, M. L. (1997). Wave height measurements from HF radar. *Oceanography*, VoI. 10, No. 2.

Graber, H. C., Thompson, D. R. & Carande R. E. (1996). Ocean surface features and currents measured with synthetic aperture radar interferometry and HF radar, *J. Geophys. Res.*, 101(C11), 25,813–25,832.

Hansen, M. W., Collard, F., Dagestad, K., Johannessen, J. A., Fabry, P., & Chapron, B. (2011). Retrieval of sea surface range velocities from envisat ASAR doppler centroid measurements. *Geoscience and Remote Sensing, IEEE Transactions on*, 49(10), 3582–3592.

Hasselmann, K. (1982). An ocean model for climate variability studies. Progress in Oceanography, 11(2), 6992.

Henderson, F. & Lewis A. (1998), *Principles and Applications of Imaging Radar, Manual of Remote Sensing, 3rd Edition, Volume 2.* New York: John Wiley and Sons.

Holt, B. (2004). SAR Imaging of ocean surface in *Synthetic Aperture Radar Marine User's Manual*. Jackson, C. R & Apel, J. R., eds, NOAA, NESDIS, Office of Research and Applications, Washington, DC. Available online at: http://www.sarusersmanual.com/ (accessed March, 2012).

Johannessen, J. A., Chapron, B., Collard, F., Kudryavtsev, V., Mouche A., Akimov, D. & Dagestad, K.-F. (2008). Direct ocean surface velocity measurements from space: Improved quantitative interpretation of Envisat ASAR observations, *Geophys. Res. Lett.*, 35.

Johannessen, J. A., Shuchman, R. A., Digranes, G., Lyzenga, D. R., Wackerman, C., Johannessen, O. M., & Vachon, P. W. (1996). Coastal ocean fronts and eddies imaged with ERS 1 synthetic aperture radar, *J. Geophys. Res.*, 101(C3).

Johannessen, J. A., Shuchman, R. A., Johannessen, O. M., Davidson, K. L., & Lyzenga, D. R. (1991). Synthetic Aperture Radar Imaging of Upper Ocean Circulation Features and Wind Fronts, *J. Geophys. Res.*, 96(C6), 10,411–10,422.

Kerbaol, V., & Collard, F. (2005). SAR-derived coastal and marine applications: From research to operational products. *Oceanic Engineering, IEEE Journal of*, 30(3), 472–486.

Lyzenga, D. R., Marmorino & G. O., Johannessen, J. A., 2004. Ocean currents and current gradients in *Synthetic Aperture Radar Marine User's Manual*. Jackson, C. R & Apel, J. R., eds, NOAA, NESDIS, Office of Research and Applications, Washington, DC. Available online at: http://www.sarusersmanual.com/ (accessed March, 2012).

Mahapatra, P. & Hanssen, R. (2011). *NEST Cookbook*. Retrieved from: http://nest.array.ca/web/nest/documentation (accessed March, 2012)

Marinkovic, P. (2009). *Fringe 2009 NEST DORIS training*. Retrieved from: http://nest.array.ca/web/nest/documentation (accessed March, 2012).

Mansourpour, M. Rajabi, M.A. & Blais, J.A.R (n.d.). "*Effects and performance of speckle noise reduction filters on active radar and SAR images*, Retrieved from: http://www.isprs.org/proceedings/XXXVI/1-W41/makaleler/Rajabi_Specle_Noise.pdf (accessed June, 2012)

Marmorino, G. O., Thompson, D. R., Graber, H. C., & Trump, C. L. (1997), Correlation of oceanographic signatures appearing in synthetic aperture radar and interferometric synthetic aperture radar imagery with in situ measurements, *J. Geophys. Res.*, 102(C8), 18,723–18,736.

Martin, S. (2004), *An Introduction to Ocean Remote Sensing*, Cambridge University press, United Kingdom.

Minchella, A. (2011). *Next ESA SAR Toolbox (NEST)*. Retrieved from http://nest.array.ca/web/nest/documentation (accessed March, 2012).

Minchella, A., & Costantini, F (2011). *Italian Coast Guard training*. Retrieved from: http://nest.array.ca/web/nest/documentation (accessed March, 2012).

McCandless, A.W. & Jackson C. R. (2004). Principles of synthetic aperture radar in *Synthetic Aperture Radar Marine User's Manual*. Jackson, C. R & Apel, J. R., eds, NOAA, NESDIS, Office of Research and Applications, Washington, DC. Available online at: http://www.sarusersmanual.com/ (accessed March, 2012).

Monaldo F.M. & Beal, R. (2004). Wind speed and direction in *Synthetic Aperture Radar Marine User's Manual*. Jackson, C. R & Apel, J. R., eds, NOAA, NESDIS, Office of Research and Applications, Washington, DC. Available online at: http://www.sarusersmanual.com/ (accessed March, 2012).

NEST User Manual. (n.d.). Retrieved from: http://nest.array.ca/web/nest/documentation (accessed March, 2012).

Paduan, J. D. & Cook, M. S, (1997). Mapping surface currents in Monterey Bay with CODAR – type HF radar. *Oceanography*, 10(2), 49-52.

Paduan, J. D. & Graber, H.C., (1997). Introduction to High-Frequency radar: reality and myth. *Oceanography*, 10(2), 36-39.

Paduan, J. D., & Rosenfeld, L. K. (1996). Remotely sensed surface currents in Monterey Bay from shore-based HF radar (Coastal Ocean Dynamics Application Radar), *J. Geophys. Res.*, 101(C9), 20,669–20,686

Paduan, J. D., Washburn, L. (2012). *High Frequency radar observations of ocean surface currents annual reviews*. Manuscript submitted for publication.

Rouault, M. J., Mouche, A., Collard, F., Johannessen, J. A., & Chapron, B. (2010), Mapping the Agulhas Current from space: An assessment of ASAR surface current velocities, *J. Geophys. Res.*, 115.

Rufenach, C. L., Shuchman, R. A., & Lyzenga, D. R. (1983), Interpretation of Synthetic Aperture Radar Measurements of Ocean Currents, *J. Geophys. Res.*, 88(C3), 1867–1876.

Ryan, J. P., Fischer, A. M., Kudela, R. M., McManus, M. A., Myers, J. S., Paduan, J. D., Ruhsam, C. M., Woodson, C. B., & Zhang, Y. (2010). Recurrent frontal slicks of a coastal ocean upwelling shadow, *J. Geophys. Res.*, 115.

Sanderson, B. G. (1995), Structure of an eddy measured with drifters, *J. Geophys. Res.*, 100(C4), 6761–6776.

Stewart, R. (1985), *Methods of Satellite Oceanography*, University of California, p.238.

Stewart, R., & Joy, J. (1974), HF radio measurements of surface currents. Deep-Sea Research on pp. 1039-1049 vol.21.

Talley L.D., Pickard G.L., Emery W.J., Swift J.H. (2011). *Descriptive Physical Oceanography: An Introduction* (Sixth Edition), Elsevier, Boston.

Teague, C.C., Vesecky, J.F., and Fernandez, D.M. (1997). HF radar instruments, past to present. *Oceanography*, 10(2), 40-44.

Thompson, D. R., Graber, H. C., & Carande, R. E. (1994). Measurements of ocean currents with SAR interferometry and HF radar. *Geoscience and Remote Sensing Symposium, 1994. IGARSS '94*. Surface and Atmospheric Remote Sensing: Technologies, Data Analysis and Interpretation, International, 4. pp. 2020-2022 vol.4.

Veci, L., Minchela, A. & Engdahl, M. (2009). *NEST user training course*. Retrieved from: http://nest.array.ca/web/nest/documentation (accessed March, 2012).

INITIAL DISTRIBUTION LIST

1. Defense Technical Information Center
   Ft. Belvoir, Virginia

2. Dudley Knox Library
   Naval Postgraduate School
   Monterey, California

3. Dr. Jeffrey Paduan
   Department of Oceanography, OC/PD
   Naval Postgraduate School
   Monterey, California

4. Benjamin Holt
   Jet Propulsion Laboratory
   California Institute of Technology
   Pasadena, California

5. CFR Santos Martinho
   Portuguese Navy, Instituto Hidrografico
   Lisbon, Portugal

6. CTE Martins Cosme
   Portuguese Navy, Direccao do Servico de Formacao
   Lisbon, Portugal

7. Instituto Hidrografico - Biblioteca
   Portuguese Navy, Instituto Hidrografico
   Lisbon, Portugal

8. Escola Naval - CINAV
   Base Naval de Lisboa, 2810-001 Alfeite
   Almada, Portugal

9. Escola Naval - Biblioteca
   Base Naval de Lisboa, 2810-001 Alfeite
   Almada, Portugal

10. LT Ricardo Vicente
    Portuguese Navy, Instituto Hidrografico
    Lisbon, Portugal